Two Approaches to White Matter Nuclear Magnetic Resonance: Water Diffusion and Inhaled Laser-Polarized Xenon

by

Sharon Peled

Submitted to the Harvard-M.I.T. Division of Health Sciences and Technology

in partial fulfillment of the requirements for the degree of

Doctor of Philosophy

at the

MASSACHUSETTS INSTITUTE OF TECHNOLOGY

June 1997

Author .....
Harvard-M.I.T. Division of Health Sciences and Technology
May 16, 1997

Certified by .....
Ferenc A. Jolesz
Professor of Radiology, Harvard Medical School
Thesis Supervisor

Certified by .....
David G. Cory
Associate Professor of Nuclear Engineering, M.I.T.
On Campus Thesis Supervisor

Certified by ..
Ronald L. Walsworth
Staff Physicist, Harvard-Smithsonian Center for Astrophysics
Thesis Reader

Certified by ..
Daniel A. Kirschner
Associate Professor of Biology, Boston College
Thesis Reader

Certified by ..
Stephen A. Raymond
Assistant Professor of Anesthesiology, Harvard Medical School
Thesis Reader

Accepted by .....
Martha L. Gray
Chairperson, Departmental Committee on Graduate Students

Two Approaches to White Matter Nuclear Magnetic Resonance: Water Diffusion and Inhaled Laser-Polarized Xenon

by
Sharon Peled

Submitted to the Harvard-M.I.T. Division of Health Sciences and Technology
on May 16, 1997, in partial fulfillment of the requirements for the degree of
Doctor of Philosophy

Abstract

The goal of the work described in this thesis is the development of both ^{129}Xe and ^{1}H NMR methods to increase the utility of magnetic resonance imaging of white matter in the brain.

The lipophilicity of xenon raises the possibility of a new source of NMR signal from within the myelin membranes after inhalation of laser-polarized ^{129}Xe. The factors influencing the accumulation of polarized ^{129}Xe in human tissue are described. The resulting model predicts the ^{129}Xe magnetization in different tissues. Substitution of estimated values for the relaxation times of ^{129}Xe in biological tissues results in an expected signal-to-noise ratio (SNR) from laser-polarized ^{129}Xe MR in the white matter of the human brain of approximately 0.6% of the equivalent SNR from proton MR.

The longitudinal relaxation time (T_1) of laser-polarized ^{129}Xe dissolved in a foam preparation of fresh human blood was measured *in vitro*. Extrapolating the results to *in vivo* oxygenation conditions, T_1 is estimated to be 5-10 sec in arterial blood. A preliminary measurement of ^{129}Xe in a purified myelin solution suggests that T_2 of ^{129}Xe in myelin may be relatively short.

Structural compartmentation in frog peripheral nerve was correlated with components of the ^{1}H transverse relaxation decay curve and with the diffusion characteristics of the water in the nerve. No restriction of water mobility was evident in the component of the signal with the intermediate T_2 relaxation time out of the three measured tissue T_2 values. Restricted diffusion was observed in the component with the longest T_2 time, supporting the assignment of at least part of the spins contributing to this component to the intra-axonal compartment. The diffusion attenuation was modeled for physiologically relevant geometries which, when averaged over the wide range of axon sizes in the nerve, could explain the observed non-exponential behavior.

Apparent diffusion tensor maps of the human brain were acquired with a magnetic resonance imaging sequence. Display of the orientation and directional uniformity of the water diffusion in the brain demonstrated most of the known major anatomical constituents of human white matter, with statistically significant hemispheric laterality found in the anterior limb of the internal capsule.

Thesis Supervisor: Ferenc A. Jolesz
Title: Professor of Radiology, Harvard Medical School

On Campus Thesis Supervisor: David G. Cory
Title: Associate Professor of Nuclear Engineering, M.I.T.

Acknowledgments

I am deeply grateful to my supervisor, Ferenc Jolesz, for his support and trust over the years. He directed my work with extraordinary clear-sightedness, and his sense of humor helped me keep mine through it all. I was also extremely fortunate in the other members of my thesis committee who were all so generous with their knowledge and their time. I cannot thank David Cory enough for the help he gave me; his expertise brought substance to my thesis and his encouragement gave me the confidence to complete it. I wish to express my sincere gratitude to Stephen Raymond for always giving wise advice, frequently sharing his original ideas, and forgiving me my technical failures. I thank Ronald Walsworth and Daniel Kirschner for their kindness and friendship. Ron stepped me through writing my first paper and his comments made me improve much of my other work. Dan gently corrected my mistakes, discussed the next steps and was ever willing to help with them.

Many others helped me at different stages during these years. I am indebted to Robert Mulkern for his continuous interest in and unconditional contributions to nearly everything I worked on. Yuan Cheng provided invaluable assistance with hardware at M.I.T. and Luigino Nascimben made having blood drawn almost pleasant. I thank Ching-Hua Tseng, Hákon Gudbjartsson and Carl-Fredrik Westin from our group for being both collaborators and friends. And I am grateful to all the other members of our group who created such a positive environment, particularly Walid Kyriakos and Larry Panych. I owe my presence in the group at Brigham and Women's Hospital to Samuel Patz and I thank him for his help during my first year here, and thereafter. I would also like to acknowledge all the people in the HST Division who together create a pleasant, efficient and supportive framework within which students are free to follow their interests.

To Pisti, for his patience and love, I dedicate this thesis.

Contents

List of Figures

List of Tables

Chapter 1

Background

1.1 Introduction

A number of physical ^{1}H nuclear magnetic resonance (NMR) properties of tissue are useful for providing contrast in magnetic resonance imaging (MRI), among them longitudinal and transverse relaxation (T_1, T_2), magnetization transfer, and diffusion. If water in structural compartments within biological tissue exhibits individual values for these parameters due to the different chemical environment, these parameters can provide information about the underlying structure of the tissue. In parts of this thesis the nature of the correspondence between the structure of an amphibian peripheral nerve and two physically measurable entities, namely the apparent diffusion of tissue water and ^{1}H transverse relaxation, is studied.

Examples of the possible clinical uses of compartmental assignment through NMR are the differentiation between intracellular versus extracellular edema, and characterization of ischemia which is accompanied by shifts in water between the intracellular and extracellular spaces. Identification of a compartment associated with the water in the myelin sheath may aid in understanding the pathogenesis of demyelinating disease. If the water in between the myelin membranes has a different characteristic transverse relaxation time than other components of the tissue, this would allow it to be differentiated from the surrounding tissue by decomposing the multiexponential T_2 decay curve. Magnetic resonance imaging is one of the main tools used in diag-

nosing demyelinating diseases, in particular multiple sclerosis (MS). Currently MRI delineates MS lesions in the brain but does not offer any specific information about the pathology. Much would be gained if the NMR signal originating in myelin could be identified, separated from the rest of the white matter signal and correlated with structural and functional changes in the myelin.

An alternative nucleus which may be useful for white matter imaging is ^{129}Xe. Optical pumping techniques [45, 26, 33, 25, 21] allow the spin-polarization of these noble gas nuclei far above thermal levels. Magnetic resonance imaging using laser-polarized ^{129}Xe was proposed in 1994 in a study in which a ^{129}Xe image of an excised mouse lung was obtained [4]. White matter perfusion and demyelination studies based on the high affinity of xenon for lipids are thus possible goals for the future, motivating our interest in ^{129}Xe MR.

In Chapter 2, the uptake of laser-polarized ^{129}Xe in tissue is modeled [81]. The SNR from human white matter is assessed to be approximately 0.6% of the equivalent ^{1}H SNR. An important factor in the model is the longitudinal relaxation time of ^{129}Xe in blood. Chapter 3 describes fast, one-shot T_1 measurements of laser-polarized ^{129}Xe dissolved in fresh human blood *in vitro* [98]. From these measurements, the longitudinal relaxation time of ^{129}Xe in arterial blood was estimated to be 5-10 s under *in vivo* conditions. A preliminary measurement of ^{129}Xe in a purified myelin solution from rat brain, outlined in Chapter 4, indicates a relatively short T_2.

Also in Chapter 4, ^{1}H T_2 of intra-myelinic water *in vivo* is estimated from T_2 of water in the purified myelin solution to be less than 50 ms. Chapter 5 addresses the problem of correlating structural compartments in an amphibian peripheral nerve with measured NMR parameters. Based on the diffusivity of water associated with each T_2 component and the measured exchange between the components, compartmental assignments of the T_2 components of the signal are made. Contrary to previous assumptions, the longest T_2 time measured from the tissue appears to be associated with the intracellular space. In Chapter 6 models of diffusion in neural tissue incorporating the whole range of axon sizes represented in the nerve are compared to the data from Chapter 5. Chapter 7 describes some tools necessary for quantitatively

assessing and displaying the results of diffusion tensor imaging of white matter tracts. An example of hemispheric laterality found with this technique in humans is shown.

1.2 Structural Properties of Myelinated Nerves

Figure 1-1A shows a schematic representation of part of a bullfrog sciatic nerve bundle. Frog sciatic nerves are easily obtained and frequently studied with a view to applying any principles learned from them to improving the specificity of diagnostic white matter MRI in humans. Compared to frog sciatic nerve, human white matter contains smaller and more densely packed axons.

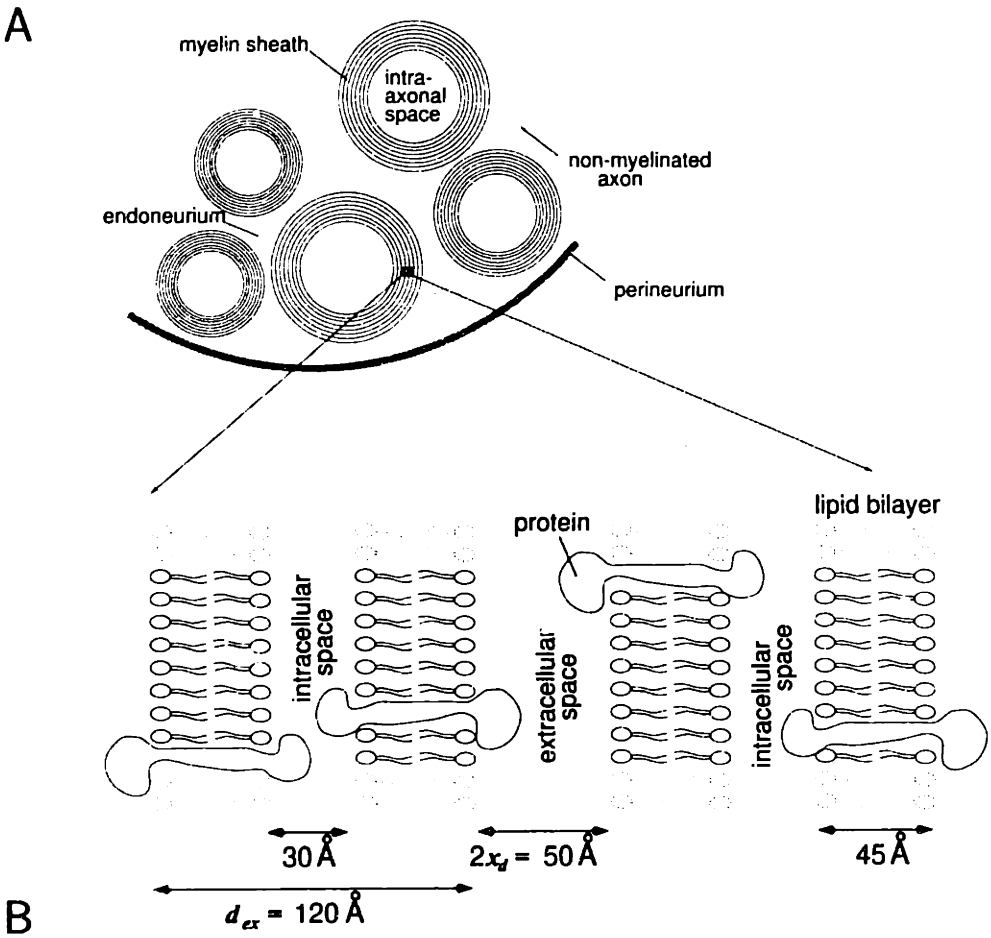

Figure 1-1: Schematic diagrams of a frog sciatic nerve. (A) Part of a fascicle cross section; (B) Myelin bilayer (dimensions from Ref. [50]).

A typical peripheral nerve trunk is about one mm in diameter and contains myelinated and non-myelinated fibers ranging in radius between 0.5 - 10 μm. The relatively large number of non-myelinated fibers contribute very little to the total volume due to their small size. The extracellular space (endoneurium) contains endoneural collagen I. The myelin sheath consists of the membranes and cytoplasm of Schwann cells which spiral around the axons up to 100 times. The total width of the myelin sheath is typically up to one half the radius of the axon which it encloses. The membranes are composed of lipid bilayers with associated proteins. Figure 1-1B shows the approximate dimensions of the bilayers and the inter- and intra-lamellar spaces, from Ref. [50]. The distance, d_{ex}, is referred to as the exclusion length because it generally remains constant when the myelin is perturbed chemically. The distance x_d may vary with the pH and with the ionic strength of the nerve's environment.

Biological membranes carry electric charge at their surfaces which are exposed to the adjacent bulk solution. These arise from charged lipid molecules, from sialic acid residues on carbohydrates, and from charged amino acid side chains of membrane proteins. Charged lipid molecules and sialic acid are mostly anionic, while amino acid side chains may bear positive or negative charges. In myelin the surface charge is usually negative and causes electrostatic repulsion between the bilayers. The surface charge density in frog sciatic nerve has been estimated at between 1,500Å^2 and 5,000Å^2 per elementary charge [86].

At physiological temperatures the lipid membranes are fluid systems although exhibiting a diffusion anisotropy of $\sim 10^7$. The phase transition from the liquid to gel phase brings with it a thickening of the bilayer and a decrease in surface area along with a decrease in molecular mobility. Certain substances can change lipid membrane properties. For example, cholesterol in lipid membranes can eliminate the gel-to-fluid phase transition. Cholesterol causes greater mechanical rigidity and thus lowers the transmembrane permeability.

In neural tissue the mobility of the water is restricted in the directions perpendicular to the axons which are oriented along the fiber tracts, leading to anisotropy of the water diffusion. Myelination is not essential for diffusion anisotropy in nervous

tissue as shown in studies of nonmyelinated garfish olfactory nerves [10] and in brains of neonates before the histological appearance of myelin [110, 48] but myelin is widely assumed to be the major barrier to diffusion in myelinated fiber tracts.

1.3 Nuclear Magnetic Resonance[2]

1.3.1 Quantum Mechanics to Vectors

A magnetic field, $\vec{H}$, breaks an energy level degeneracy in particles possessing non-zero angular momentum, $\vec{J}$, through the Zeeman interaction. The Hamiltonian describing the interaction is:

$$\mathcal{H} = -\vec{\mu} \cdot \vec{H} \tag{1.1}$$

where the magnetic moment, $\vec{\mu}$, is proportional to the angular momentum through the gyromagnetic constant, γ:

$$\vec{\mu} = \gamma \vec{J}. \tag{1.2}$$

The angular momentum of the nuclei of both ^{1}H and ^{129}Xe is $\hbar/2$ therefore in these examples the energies corresponding to the Zeeman Hamiltonian are:

$$E = \pm \frac{\gamma \hbar H}{2} \tag{1.3}$$

resulting in the transition, or resonance, frequency, ω, between the energy levels:

$$\omega = \gamma H. \tag{1.4}$$

The time dependence of the expectation value of an operator F, that is not explicitly time dependent, can be derived directly from Schrödinger's equation and is given by:

$$\frac{d\langle F \rangle}{dt} = \frac{i}{\hbar} \langle [\mathcal{H}, F] \rangle \tag{1.5}$$

[1] Reference [2] is a widely read text on this subject.

Substitution of $F = \vec{\mu}$ and the Hamiltonian from Eq. 1.1, and using the permutation properties of the commutation relations between the components of the angular momentum operator, we get:

$$\frac{d\langle\vec{\mu}\rangle}{dt} = \langle\vec{\mu}\rangle \times \gamma\vec{H}\,. \tag{1.6}$$

Equation 1.6 describes the time dependence of the expectation value of the magnetic moment of a single spin but applies equally well to the magnetic moment of an ensemble of non-interacting spins. Equation 1.6 is formally the same as the classical description of a magnetic moment interacting with a magnetic field:

$$\frac{d\vec{M}}{dt} = \vec{M} \times \gamma\vec{H}, \tag{1.7}$$

and provides justification for treatment of the spin ensemble as a magnetization vector.

The equilibrium magnetization of an ensemble of spins in a static magnetic field, H_0, is determined by the Boltzmann distribution. The slightly higher interaction energy of spins antiparallel (depending on the sign of γ) to the field creates a small reduction in the number of these spins compared to those that are oriented parallel to the field. The ratio of numbers of antiparallel spins, N_+, versus parallel spins, N_- is:

$$\frac{N_+}{N_-} = e^{-\Delta E/kT} = e^{-\gamma\hbar H_0/kT} \approx 1 - \frac{\gamma\hbar H_0}{kT} \tag{1.8}$$

the last approximation justified by $kT \simeq 4 \times 10^{-14}$ erg and $\gamma\hbar H_0 \simeq 3 \times 10^{-19}$ erg for MR imaging systems temperatures and field strengths. The bulk equilibrium magnetization density is defined by:

$$\begin{aligned} M_0 &= (N_- - N_+)|\vec{\mu}| \\ &= (N_- - N_+)\gamma\hbar/2 \\ &\approx \frac{N\gamma^2\hbar^2 H_0}{4kT} \end{aligned} \tag{1.9}$$

where N is the particle density.

The direction of the magnetization vector can be manipulated by applying a time-dependent magnetic field perpendicular to the main field, $\vec{H}_0$. If the applied field oscillates at or close to the resonance frequency, ω, in a frame of reference rotating at this frequency, the main field will vanish and the expectation value of the spin ensemble will react to the transverse field by manifesting the Zeeman splitting relative to the transverse plane resulting in the magnetization vector tipping into the transverse plane. Once there, it can be measured during its coherent precession in the laboratory frame.

1.3.2 Relaxation

As we saw in the previous section, when a magnetic field is applied to the spin ensemble, at thermal equilibrium the magnetic moments of the spins will have a Boltzmann distribution and a net magnetic moment, designated by M_0. If the field is removed, the equilibrium state will no longer be that of bulk magnetization but of a less ordered state with no prefered direction of magnetization. The exponential time constant characterizing the loss of bulk magnetic moment of an ensemble of spins is called the longitudinal relaxation time and designated by the symbol T_1. Longitudinal relaxation is also refered to as spin-lattice relaxation because the change in state is mediated by the energy transfer between the particles and their surroundings.

If the precession of the spins is made coherent by a radio-frequency (RF) field in the transverse direction, as outlined in the previous section, a detectable signal will result. Even if the external magnetic field were perfectly homogeneous, the spins will not all precess with exactly the same angular velocity, resulting in an eventual dephasing of the transverse components of the signal. The time constant that characterizes this loss of transverse magnetization is called the transverse relaxation time and designated by the symbol T_2. Transverse relaxation is also refered to as spin-spin relaxation due to its origin in interactions between neighboring particles. In liquids the transverse magnetization decays in an exponential manner.

The phenomenological Bloch equations incorporate these two relaxation times

with the classical description of the interaction between a magnetic moment and a magnetic field from Eq. 1.7 [16]:

$$\frac{dM_x}{dt} - \gamma(M_y H_z - M_z H_y) + \frac{M_x}{T_2} = 0, \tag{1.10}$$

$$\frac{dM_y}{dt} - \gamma(M_z H_x - M_x H_z) + \frac{M_y}{T_2} = 0, \tag{1.11}$$

$$\frac{dM_z}{dt} - \gamma(M_x H_y - M_y H_x) + \frac{M_z - M_0}{T_1} = 0. \tag{1.12}$$

The dominant relaxation interaction for spin $\frac{1}{2}$ nuclei in tissue is the dipole interaction which is due to the effect of the field created by the dipole moment of each particle on its neighbors. The potential energy of two interacting magnetic dipole moments is:

$$\phi = \frac{\vec{\mu}' \cdot \vec{\mu}}{r^3} - \frac{3(\vec{\mu} \cdot \vec{r})(\vec{\mu}' \cdot \vec{r})}{r^5}. \tag{1.13}$$

Expressions for T_1 and T_2 due to the dipolar interaction have been derived from the Hamiltonian corresponding to Eq. 1.13 (see for example, [2, 67]). For systems of like spin $\frac{1}{2}$ particles they are:

$$\frac{1}{T_1} = j(\omega_0) + 4j(2\omega_0), \tag{1.14}$$

$$\frac{1}{T_2} = \frac{3}{2}j(0) + \frac{5}{2}j(\omega_0) + j(2\omega_0),$$

where $j(\omega)$ is refered to as the spectral density of the magnetic field fluctuations and ω_0 is the resonance frequency of the spins. The spectral density corresponding to dipolar coupling can be calculated from the Hamiltonian if the relative thermal motion of the spins is known. The motion is assumed rotational if the spins belong to the same molecule, and both rotational and translational if the interaction is intermolecular.

If within an NMR sample there is some degree of spatial ordering of the molecules, the dipolar interaction can be minimized by orienting the sample at the "magic" angle of $\sim 55°$ relative to the magnetic field (solution of $3\cos^2\theta - 1 = 0$). Some biological tissues such as tendon and cartilage, do indeed exhibit changes in relaxation times dependent upon their orientation but no such effect was observed in nerve [46].

1.3.3 The Spin Echo

In 1950 Erwin Hahn found that the dephasing of the transverse magnetization due to an inhomogeneous magnetic field could be refocussed by the application of a second RF pulse [44]. Today the signal from a pulse sequence consisting of a 90° pulse (leaves no longitudinal magnetization) followed by a 180° pulse, is called a Hahn spin-echo. The time between the initial pulse and the formation of the echo is designated by the expression TE for echo-time.

The spin echo does not refocuss dipolar coupling between like spins so the amplitude of the Hahn spin-echo relative to the original signal allows estimation of T_2. A method suited to measuring multi-exponential T_2 times is the Carr-Purcell-Meiboom-Gill (CPMG) pulse sequence which provides more points on the T_2 relaxation decay curve by following the 180° pulse with many additional 180° inversion pulses, each one refocussing the previous echo. The phase of the inversion pulses in the CPMG sequence is 90° shifted from that of the first 90° pulse and acquisition is restricted to the even echoes in order to correct for pulse tip-angle imperfections.

Often, acquiring the signal from an echo is more convenient than measuring the initial signal decay after a pulse. When the echo amplitude is required to suffer minimal T_2 decay, a series of three 90° pulses is often used which creates a "stimulated echo" after the third pulse. The amplitude of the stimulated echo is almost independent of T_2 because for most of the duration of TE the magnetization vector is not in the transverse plane.

1.3.4 Diffusion

Fick's second law describes diffusion within a homogeneous region:

$$\frac{\partial c}{\partial t} = D\nabla^2 c\,. \tag{1.15}$$

If the initial condition is given by $c(\vec{r}', 0) = \delta(\vec{r}' - \vec{r})$, the solution of Eq. 1.15, which represents the probability that a spin which starts at position $\vec{r}$ will end up at position

$\vec{r}'$ after time t, is given by the following gaussian distribution:

$$P(\vec{r}|\vec{r}',t) = c(\vec{r}',t) = (4\pi Dt)^{-3/2} e^{-(\vec{r}'-\vec{r})^2/4Dt}. \tag{1.16}$$

The mean square displacement for free diffusion in 3 dimensions is, from Eq. 1.16:

$$\langle(\vec{r}' - \vec{r})^2\rangle = 6Dt. \tag{1.17}$$

The main method of detecting diffusion with NMR relies on dephasing the NMR signal from diffusing spins. Two identical magnetic field gradients are applied, the second at time Δ after the first [18, 93]. The phase of a diffusing spin at position $\vec{r}$ experiencing a constant gradient $\vec{g}$ for duration δ, will increase by:

$$\phi = \gamma\delta\vec{g}\cdot\vec{r}\,. \tag{1.18}$$

When this phase is inverted by a π RF pulse, after experiencing another gradient equal to the first, the phase shift will be:

$$\phi = \gamma\delta\vec{g}\cdot(\vec{r}' - \vec{r})\,, \tag{1.19}$$

where $\vec{r}'$ is the new position of the spin at the time of the second gradient pulse. The attenuation of the NMR signal stems from integration over all the spins with all their respective phase shifts. The NMR signal attenuation after diffusion time Δ is then:

$$E_\Delta(\vec{g}) = \int\int \rho(\vec{r})P(\vec{r}|\vec{r}',\Delta)e^{\imath\gamma\delta\vec{g}\cdot(\vec{r}'-\vec{r})}d\vec{r}d\vec{r}'\,. \tag{1.20}$$

The solution of Eq. 1.20 for free, unrestricted diffusion, turns out to be:

$$E_\Delta(\vec{q}) = e^{-bD}\,, \tag{1.21}$$

where $b = q^2\Delta$ and $\vec{q} = \gamma\delta\vec{g}$.

In the narrow pulse approximation assumed above, the motion of the spins dur-

ing the application of the gradient pulses is negligible, i.e. $\delta \ll \Delta$. The diffusion attenuation corrected for cases in which this assumption is not valid is given by [93]:

$$E_{\Delta}(\vec{q}) = e^{-q^2(\Delta - \delta/3)D} . \tag{1.22}$$

Measurement by NMR of diffusion relies on obtaining the signal attenuation, $E_{\Delta}(\vec{q})$, for different values of the b-factor, usually by stepping the gradient strength.

1.4 Laser-Polarized ^{129}Xe MRI

^{129}Xe is a stable, nuclear spin $\frac{1}{2}$ isotope of xenon with a natural abundance of 26%. Nuclear spin polarizations greater than 10% can be created in samples of ^{129}Xe gas at pressures near 1 atmosphere using a technique in which transient hyperfine interactions during collisions between the ^{129}Xe atoms and optically-pumped Rb vapor polarize the ^{129}Xe gas. After this "hyper-polarization", the bulk magnetization in the ^{129}Xe sample is approximately 10^5 times larger than that of the same number of protons in a field of 1 Tesla. This non-Boltzmann distribution relaxes back to thermal equilibrium with a characteristic time T_1.

Xenon is an inert gas which, although possessing anaesthetic properties, can be safely inhaled at relatively high concentrations [13]. After inhalation, xenon is transported throughout the body by the blood. The solubility of ^{129}Xe in blood allows for its transport to tissues distal from the lung [23].

The potential clinical applications of polarized ^{129}Xe MR are unknown at this stage and depend on the attainable signal-to-noise ratio (SNR). The lung and other readily accessible gas spaces, such as the sinuses, have been the first candidates for imaging [89, 104, 20]. Large ^{129}Xe chemical shifts (150 ppm in common organic solvents [71]) suggest chemical shift imaging and *in-vivo* spectroscopy in other organs. ^{129}Xe tissue resonances have been observed in live mice [104], live rats [89, 88], and most recently in the human brain [20]. A chemical shift image of inhaled, laser-polarized ^{129}Xe in a live rat brain has also been obtained [95].

Chapter 2

Determinants of Tissue Delivery for ^{129}Xe Magnetic Resonance in Humans[1]

2.1 ^{129}Xe Uptake Model

The uptake process begins with the inhalation of polarized ^{129}Xe gas, followed by transport of the ^{129}Xe in the blood stream to the tissue of interest and build-up of the magnetization in that tissue.

We make several assumptions:

1. There is a constant external supply of polarized ^{129}Xe.
2. The inhaled tidal gas mixes completely with the total alveolar gas within the lungs before exhaling.
3. Breathing can be approximated as continuous, i.e. there is a constant rate of gas exchange, R_F, with an alveolar volume, V_A.

[1] S. Peled, F. A. Jolesz, C-H. Tseng, L. Nascimben, M. S. Albert, and R. L. Walsworth. Determinants of tissue delivery for ^{129}Xe magnetic resonance in humans. *Magn. Reson. Med.*, 36:340-344, 1996.

4. Blood is known to spend less than 1 second in transit in any capillary, whether in lung or in target organs, and to emerge in equilibrium with local tissue concentrations of diffusible species [49]. We thus assume that the blood transit time in any organ other than artery or vein can be set to zero, and that diffusion equilibrium is instantaneous.

5. Dissolved ^{129}Xe in the blood is transported to and from body tissues at the rate of local perfusion.

The expression for the change with time of the total amount of polarized ^{129}Xe in the alveoli is given in Eq. 2.1, where C_A is the alveolar concentration of polarized ^{129}Xe:

$$V_A\dot{C}_A = C_I R_F - C_A(R_F + \frac{V_A}{\mathrm{T}_{1_{air}}} + \lambda\dot{Q}) \ . \tag{2.1}$$

Equation 2.1 contains contributions from the following sources:

1. The inhaled flow, $C_I R_F$, where $C_I = fP/V_0$ is the inhaled concentration of polarized ^{129}Xe which is determined by the fraction of ^{129}Xe in the inhaled air mixture, f, and the initial polarization fraction of the ^{129}Xe, P. V_0 is the molar volume of an ideal gas at lung temperature and water vapor pressure.

2. The exhaled flow, $-C_A R_F$.

3. The decay of polarization in the lung, $-C_A V_A/\mathrm{T}_{1_{air}}$.

4. The flow into the pulmonary blood, $-C_A\lambda\dot{Q}$, where $\dot{Q}$ is the pulmonary blood flow and λ is the partition coefficient for xenon between blood and gas. (Partition coefficients define the ratio of the concentrations of a substance between two different media at equilibrium.)

We neglect any contribution from ^{129}Xe returning from the circulation because our calculations indicate that this contribution is small. The theoretical maximal contribution of venous return is equal to the flow into the pulmonary blood, $C_A\lambda\dot{Q}$.

Canceling this term in Eq. 2.1 and using the lung physiology parameters from Table 2.1 results in only a 5% change in alveolar concentration. Figure 2.1 shows a schematic representation of the model.

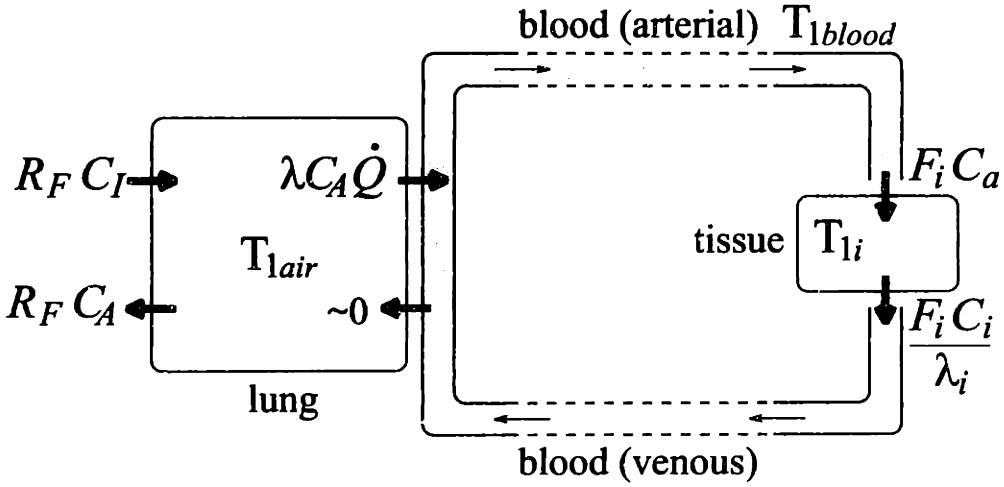

Figure 2-1: Flow diagram of polarized ^{129}Xe in the body.

The solution of Eq. 2.1 for C_A is given by:

$$C_A(t) = C_I R_F (1 - e^{-\frac{t}{V_A}(R_F + \frac{V_A}{T_{1_{air}}} + \lambda\dot{Q})})/(R_F + \frac{V_A}{T_{1_{air}}} + \lambda\dot{Q}). \tag{2.2}$$

The estimated concentration of ^{129}Xe polarization in the arterial blood which reaches the tissue, C_a, is obtained from the alveolar concentration by multiplying by the blood/gas partition coefficient and by the longitudinal relaxation term in blood, $e^{-t_i/T_{1_{blood}}}$:

$$C_a(t) = \lambda C_A(t - t_i) e^{-\frac{t_i}{T_{1_{blood}}}}, \tag{2.3}$$

where t_i is the time the xenon spends in solution before reaching the capillaries of tissue i.

From Fick's principle we can write (following Ref. [58]) an equation for the tissue saturation process:

$$\dot{C}_i = F_i(C_a - \frac{1}{\lambda_i} C_i), \tag{2.4}$$

where C_i is the polarized ^{129}Xe concentration in tissue i, F_i is the blood flow to the

tissue (measured in ml of blood per ml of tissue per second), and λ_i is the partition coefficient between tissue i and blood.

Equation 2.4 should be modified to include the decay of polarization in the tissue with time constant T_{1_i}:

$$\dot{C}_i = F_i C_a - (\frac{F_i}{\lambda_i} + \frac{1}{T_{1_i}})C_i \quad , \quad t > t_i \, . \tag{2.5}$$

The final expression for the concentration of polarized xenon in tissue is the solution of Eq. 2.5 which incorporates Eqs. 2.2 and 2.3 and the initial condition $C_i(t_i) = 0$. The full, time-dependent solution of Eq. 2.5 is:

$$C_i(t) = \frac{\delta}{\alpha - \beta}\left(1 - e^{-\beta(t-t_i)} - \frac{\beta}{\alpha}(1 - e^{-\alpha(t-t_i)})\right) \tag{2.6}$$

with

$$\begin{aligned} \alpha &= \frac{F_i}{\lambda_i} + \frac{1}{T_{1_i}} \quad , \\ \beta &= \frac{R_F}{V_A} + \frac{1}{T_{1_{air}}} + \frac{\lambda \dot{Q}}{V_A} \quad , \\ \delta &= \frac{F_i \lambda C_I R_F e^{-t_i/T_{1_{blood}}}}{\beta V_A} \quad . \end{aligned}$$

In steady-state ($t \to \infty$) one finds:

$$C_i(\infty) = \frac{\delta}{\alpha} = \frac{C_I e^{-\frac{t_i}{T_{1_{blood}}}} \lambda R_F F_i}{(R_F + \frac{V_A}{T_{1_{air}}} + \lambda \dot{Q})(\frac{F_i}{\lambda_i} + \frac{1}{T_{1_i}})} \, . \tag{2.7}$$

2.2 Model Calculations for Brain Tissues

The calculated time-dependent build-up of polarized ^{129}Xe in brain tissue components is shown in Fig. 2-2. Steady state is achieved within approximately 60 seconds. The values for the model parameters used in calculating these concentrations are specified in Tables 2.1, 2.2 and 2.3 with references.

The fraction of ^{129}Xe in the inhaled gas mixture is determined by both the need to prevent any anesthetic effects and by the enrichment of the xenon with ^{129}Xe.

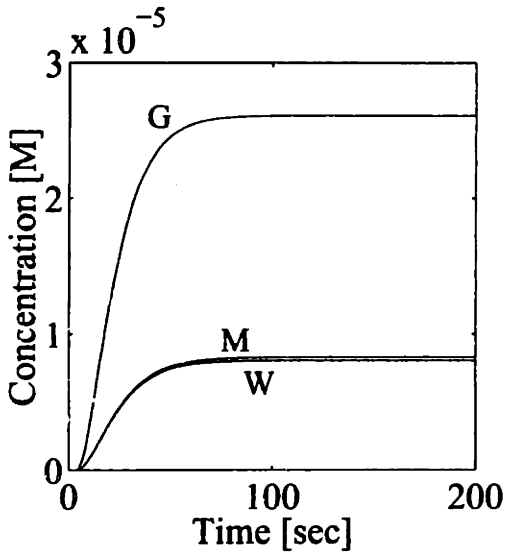

Figure 2-2: Calculated time-dependent accumulation of polarized ^{129}Xe in white matter (W), grey matter (G) and myelin (M).

Variable	R_F (liter/sec)	V_A (liter)	V_0 (liter)	P	f	λ	$\dot{Q}$ (liter/sec)
Value	0.088[a]	3[a]	18.5	0.5[b]	0.25†	0.17[c]	0.083[a]

† see text.
[a] from [105].
[b] from [25] and [21].
[c] from [23] at 37°C and 50% hematocrit estimated from a graph.

Table 2.1: General uptake model parameters

We have assumed enrichment of 70% and a maximal, sub-anesthetic concentration of 35% [13] to obtain $f = 0.25$ in Table 2.1. The arterial transit time, t_i, is estimated as 4 seconds for the brain.

^{129}Xe longitudinal relaxation times in blood and tissues are uncertain. Recent measurements by one of us and co-workers found T_1 values of 9.6±2 sec for plasma and 4.5±1 sec for RBC using thermally-polarized ^{129}Xe [5]. These T_1 measurements were obtained during approximately 8 hours of signal averaging which may have shortened T_1 because of blood oxidization and degradation. We choose to simplify our model by using an average value of 7 seconds for T_1 of blood, noting that this may represent a lower limit.

Measurements of ^{129}Xe T_1 in octanol as a function of oxygenation [6], give a value

Location	in the lung[a] ($T_{1_{air}}$)	in blood† ($T_{1_{blood}}$)	in tissue† (T_{1_i})
Value (sec)	16	7	12

† see text.
[a] from [83] at 23°C in oxygenated air.

Table 2.2: Estimated longitudinal relaxation times of ^{129}Xe in biological organs.

Tissue	F_i (min^{-1})	λ_i
Grey Matter	0.80[a]	0.79[b]
White Matter	0.21[a]	1.32[b]
Myelin	0.21[c]	17[d]
Muscle	0.05[a]	0.58[e]
Fat	0.02[a]	9.8[c]
Kidney	4.1[a]	0.66[e]
Liver	0.4[a]	0.72[e]
Heart	0.8[a]	0.69[e]

[a] from [66].
[b] from [23], in-vitro data from dogs; at 37°C and 50% hematocrit obtained from tissue/gas and blood/gas partition coefficients.
[c] assumed the same as white matter.
[d] based on the value given for octanol in Ref. [85].
[e] from [7], in-vivo data from rats; hematocrit 50%.

Table 2.3: Tissue perfusion rates (F_i) and tissue/blood partition coefficients for xenon (λ_i).

for T_1 in octanol, oxygenated to the level of venous blood (50 torr), of ~41 seconds. Since octanol is often used as a surrogate membrane in solubility studies [40], we also apply this analogy. If the effects of anisotropy-induced magnetic field fluctuations in membranes are compatible to those in liquid crystals [29], this parallel relaxation mechanism would reduce the ^{129}Xe T_1 in membranes to ~17 seconds. In the aqueous tissue components, we estimate the T_1 to be comparable to that measured in blood plasma (~10 seconds). For the model calculations, we estimated the ^{129}Xe T_1 in typical tissue to be 12 seconds, noting that this value is uncertain and may differ for specific tissues.

2.3 Calculation of SNR

The ratio of the intrinsic SNRs for polarized ^{129}Xe MR in specific tissue to ^{1}H MR in typical tissue is given by the ratio of magnetizations [34, 47], assuming that inductively coupled thermal noise in the tissue is the dominant source of noise as is typical in biological MR at fields of approximately 1 tesla [34]. Under such conditions, the proportionality relations for the signal (S), the noise (N), and the sample resistance (R_s) are given by:

$$S \propto \omega M \quad , \quad N \propto \sqrt{R_s} \quad , \quad R_s \propto \omega^2 \tag{2.8}$$

where ω is the Larmor frequency and M is the magnetization. Thus the ratio of SNRs for ^{129}Xe and ^{1}H MR is given by:

$$\frac{(SNR)_{Xe}}{(SNR)_H} = \frac{C_i(t)}{C_H B_H} \frac{\gamma_{Xe}}{\gamma_H}, \tag{2.9}$$

where γ_{Xe} and γ_H are the gyromagnetic ratios for ^{129}Xe and ^{1}H respectively, $C_i(t)$ is the concentration of polarized ^{129}Xe in tissue i, C_H is the concentration of ^{1}H in typical biological tissue - a representative value being 80 Molar, and B_H is the Boltzmann polarization fraction for ^{1}H given by the expression:

$$B_H = \frac{\hbar \gamma_H H_0}{2kT} \quad . \tag{2.10}$$

B_H evaluates to $5 * 10^{-6}$ for a field of $H_0 = 1.5$ tesla and a temperature of $T = 37°$C. (Note that B_H is linearly dependent on magnetic field strength, so that $\frac{(SNR)_{Xe}}{(SNR)_H}$ increases at low fields.) The gyromagnetic ratio of ^{129}Xe is given by $\gamma_{Xe} = 0.277\gamma_H$ [83]. Substitution of the values for C_i in steady state (calculated above and shown in Fig. 2-2) gives a SNR for grey matter in the brain of 2% relative to the SNR for ^{1}H in typical body tissue, with 0.6% for white matter. For comparison, imaging of sodium is performed in-vivo with a relative SNR of approximately 10^{-4}. The relative equilibrium SNR is 0.06% for myelin, calculated by multiplying the predicted myelin concentration by the myelin volume fraction in white matter - approximately $\frac{1}{10}$. Thus we expect the signal originating in myelin to have a significant effect on the resonance

frequency distribution and relaxation profile of the total signal received from white matter. Myelin membranes do not contribute observable signal in ^{1}H MR.

2.4 Discussion

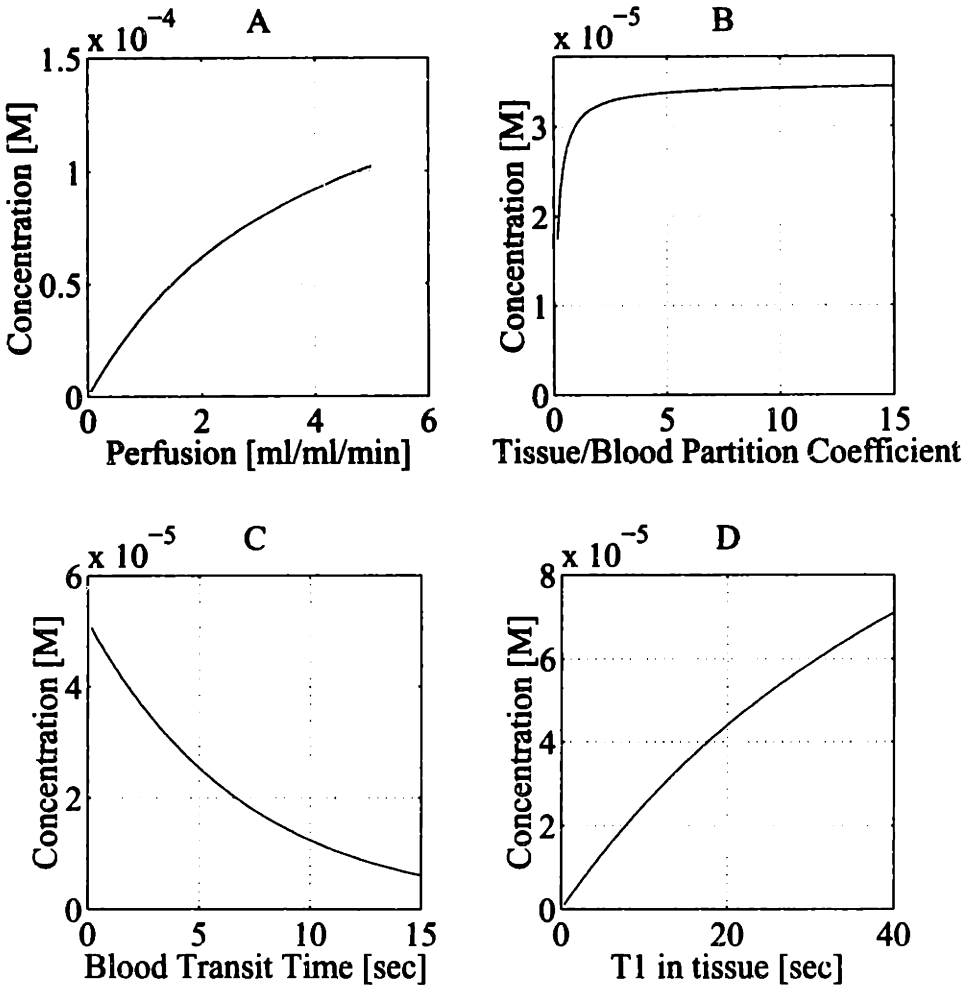

Figure 2-3: Dependence of the steady state tissue concentration of polarized ^{129}Xe on tissue-specific characteristics. The parameters not being varied correspond to the values for grey matter, given in Tables 2.1, 2.2 and 2.3.

We have presented a model of polarized ^{129}Xe uptake in human tissue and an assessment of the potential signal obtainable from ^{129}Xe MR in brain tissues. The model should be useful for the design and analysis of quantitative human experiments. Tissue contrast would be determined by the tissue-specific parameters in the model. Figure 2-3 shows the dependence of the steady state tissue concentration of polar-

ized ^{129}Xe on the tissue-specific parameters. The model indicates that the ^{129}Xe MR signal will be significantly larger from tissues with higher perfusion, shorter blood transit time and longer T_{1_i} but will not depend strongly on the tissue/blood partition coefficient. This conclusion has negative implications regarding the possibility of preferentially detecting ^{129}Xe in myelin.

Other factors, such as the possible depolarizing effects of passage through membranes and within blood vessels, have not been considered due to the lack of experimental data. Our uncertainty concerning ^{129}Xe T_1 times in the lung and in blood *in-vivo* is reflected in Fig. 2-4 which shows the change in the relative steady state SNR as a function of $T_{1_{air}}$ and $T_{1_{blood}}$. Incorrect estimation of these T_1 times leads to a large variation in relative SNR. The next chapter records our attempts to determine the value of $T_{1_{blood}}$. T_2 of ^{129}Xe in brain tissue does not influence the concentration of polarized ^{129}Xe but may greatly affect the obtainable SNR from imaging experiments and has yet to be conclusively determined.

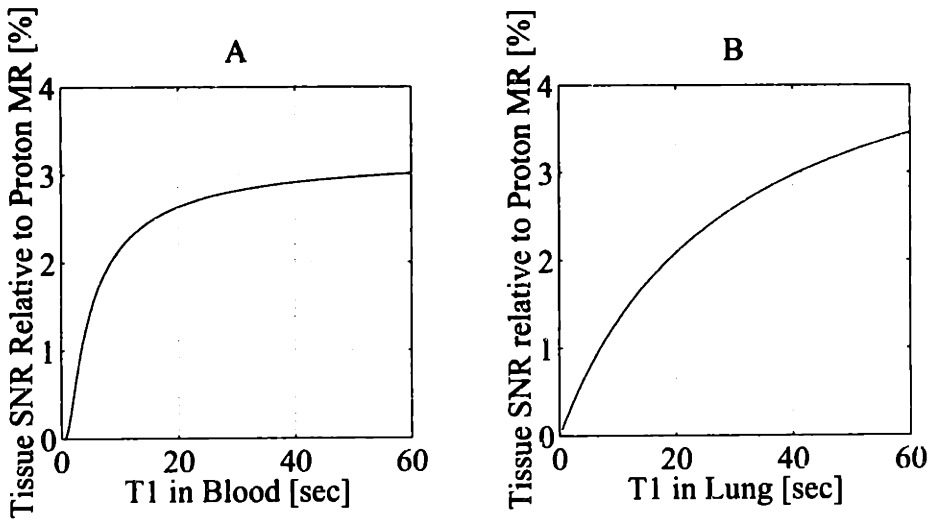

Figure 2-4: Dependence of the steady state ^{129}Xe signal from typical tissue on the T_1 times in the lung and in blood. Signal given in terms of the relative SNR compared to proton SNR from the tissue.

Chapter 3

T_1 of Laser-Polarized ^{129}Xe Dissolved in Blood[1]

3.1 Introduction

One of the most important unknown parameters in the model presented in Chapter 2 is the longitudinal relaxation time of ^{129}Xe in blood. This chapter deals with measurements made *in vitro* in order to set a value to T_1 in blood.

Laser polarized ^{129}Xe gas is a large non-equilibrium NMR signal source. Introduction of xenon into a liquid sample should ideally be rapid and leave no gas phase xenon in contact with the sample when measurements commence. Even a small residual amount of highly polarized gas would influence the observed relaxation times through exchange with the dissolved xenon in the sample. In their recent demonstration of an injectable polarized ^{129}Xe agent, Bifone et al. [14] found a 5 sec ^{129}Xe T_1 in blood using an open air sample tube, which may have affected the value obtained. In the reported *in vivo* rodent investigations of polarized ^{129}Xe dissolved in blood and other tissues [104, 89, 88], only effective polarization lifetimes were determined because of the ^{129}Xe exchange with the lung gas space and other tissues.

In contrast, the measurement reported here exploits the ^{129}Xe gas-blood phase

[1] C-H. Tseng, S. Peled, L. Nascimben, E. Oteiza, R. L. Walsworth and F. A. Jolesz. T_1 of Laser-Polarized ^{129}Xe in Blood Foam. *J. Magn. Reson.*, in press, 1997.

exchange in a closed *in vitro* system. The surface area for exchange was deliberately increased by shaking the blood-gas sample to create a foam. Because the gas phase ^{129}Xe has a longer T_1 and greater density than the blood phase ^{129}Xe, the gas phase served as a source of ^{129}Xe magnetization. Thus, the foam system increased the amplitude and lengthened the observed lifetime of the NMR signal from ^{129}Xe dissolved in the blood. The ^{129}Xe exchange between the gas and blood phases was accounted for in the analysis of the observed decaying ^{129}Xe NMR signals. Due to the dependence of the exchange on the surface area, the ^{129}Xe signal may also be an indicator of foam structure evolution such as coarsening or drainage.

3.2 Theory

Let the ^{129}Xe magnetization in the gas phase be labeled G, and that dissolved in the blood phase, B. Here and throughout this chapter, we use the term "magnetization" to describe the ensemble magnetic moment - an extensive variable. The ^{129}Xe NMR resonance frequencies of these phases are observed to be approximately 200 ppm apart which makes both separately measurable. The total number of xenon atoms is conserved in a closed system. The ^{129}Xe magnetization in each phase can change because of a) exchange between the phases, b) RF interrogation, or c) T_1 relaxation of the spin polarization back to thermal equilibrium.

From the relative initial signals of the ^{129}Xe gas and blood phase peaks and from the known solubility of xenon in blood [23], we determined that the xenon concentrations in the blood samples in our experimental system were approximately 2% of saturation. This low xenon concentration, and the observed speed with which the blood phase signal was affected by RF pulses on the gas resonance, implies that all the ^{129}Xe blood signal came from the blood foam. Thus we model the two-phase exchange system in the presence of a series of equally spaced RF pulses as a 2-site exchange system:

$$\frac{dG}{dt} = -R'_G G - k_G G + k_B B \tag{3.1}$$

$$\frac{dB}{dt} = -R'_B B - k_B B + k_G G, \tag{3.2}$$

where $R'_G = R_G - \frac{\ln\cos\theta_G}{\tau}$ and $R'_B = R_B - \frac{\ln\cos\theta_B}{\tau}$. The logarithm terms are due to the effect of the RF read pulses spaced time τ apart with flip angles $\theta_{G,B}$ on the gas and blood respectively. This effect can be derived by noting that the magnetization remaining at time $t = n\tau$, after n RF read pulses, is $G(t) = G_0(\cos\theta_G)^n$ assuming no exchange or T_1 relaxation. The constants, R_G and R_B, are the intrinsic longitudinal relaxation rates ($\frac{1}{T_1}$) of ^{129}Xe in the gas and the blood. k_G and k_B are the xenon gas-to-blood and blood-to-gas chemical exchange rates. These constants can be interpreted as reciprocal residence times.

The solutions of Eqs. 3.1 and 3.2 are of biexponential form [113]:

$$G = G_1 e^{-\mu_1 t} + G_2 e^{-\mu_2 t}, \tag{3.3}$$

$$B = B_1 e^{-\mu_1 t} + B_2 e^{-\mu_2 t}, \tag{3.4}$$

where

$$\mu_{1,2} = \frac{1}{2}\left[k_G + k_B + R'_G + R'_B \mp \sqrt{(k_G - k_B + R'_G - R'_B)^2 + 4k_G k_B}\right]. \tag{3.5}$$

The constants $G_{1,2}$ and $B_{1,2}$ depend on the initial conditions. Equations 3.3-3.5 describe well the measured signals in our experiments (see below).

For our system, the ^{129}Xe magnetization relaxation time in the gas phase is longer than in the dissolved phase i.e. $R_G < R_B$, resulting also in $R'_G < R'_B$. This analysis will not be effective for cases in which this condition does not hold. Due to the much larger quantity of gas-phase xenon than dissolved blood-phase xenon, detailed balance implies that the xenon residence time in the gas ($\tau_G = 1/k_G$) is much longer than in the blood, i.e., $k_G \ll k_B$. Under these conditions,

$$\mu_1 \simeq R'_B + k_B\ , \tag{3.6}$$

and from Eq. 3.2:

$$\frac{dB}{dt} \simeq -\mu_1 B + k_G G \,. \tag{3.7}$$

Note two important limiting cases: a) $G \gg B$, which results in $G \simeq G_2 e^{-\mu_2 t}$; and b) $G \to 0$, e.g. after reduction of G with 90° pulses, which results in $B \simeq B_1 e^{-\mu_1 t}$.

The time behavior of the total magnetization, $G + B$, does not depend on the exchange rates, as can be seen by adding Eqs. 3.1 and 3.2. R_B and R_G can be obtained if both $G(t)$ and $B(t)$ are known. In practice however, this approach cannot be effectively utilized because of sensitivity limitations. Therefore, to extract the pure T_1 value from the measured decay rate μ_1, the exchange rate, k_B, must be estimated. The lower bound for k_B is 0. Since the solubility of xenon in blood does not depend on the oxygenation level [91], an upper bound for k_B, using Eq. 3.6 and the definition of R'_B, is $\mu_{1(low)} + \frac{\ln \cos \theta_B}{\tau}$ where $\mu_{1(low)}$ is the lowest measured value of μ_1 for different oxygenations in a given sample type. When the values of μ_1 do not differ very much between sample types, the value for this upper limit is overestimated. Limits on the blood-phase ^{129}Xe T_1 are expressed in Eq. 3.8:

$$(\mu_1 + \frac{\ln \cos \theta_B}{\tau})^{-1} < \; T_1 \; < (\mu_1 - \mu_{1(low)})^{-1} \tag{3.8}$$

The determination of the ^{129}Xe T_1 in the dissolved phase should not depend on the initial relative magnetizations of the blood and gas phases or on the relaxation rate in the gas phase. Experimental tests were consistent with the model described above - see Results section.

3.3 Materials and Methods

3.3.1 Preparation of Polarized ^{129}Xe

Preparation of the polarized ^{129}Xe gas sample followed procedures described elsewhere [45, 21]. Angular momentum from circularly polarized light was transferred to electronic and then nuclear spins, through a process known as spin-exchange op-

tical pumping, producing a nuclear spin polarization far above thermal equilibrium [57, 17]. In the experiments reported here, the ^{129}Xe nuclei were polarized to about 10% of complete alignment through spin-exchange collisions with optically pumped rubidium vapor [45]. This 10% polarization should be compared to the thermal ^{129}Xe polarization of $\sim$ 0.002% at 4.7 T. The xenon was contained in a 25 ml cylindrical Pyrex cell coated with OTS (octadecyl-trichlorosilane) in order to reduce the effect of relaxation of the ^{129}Xe polarization due to wall interactions. The Pyrex cell contained a few grams of rubidium metal of natural isotopic abundance, about 100 torr of N_2, and 3 atm of xenon gas of natural isotopic abundance (26% rich in the ^{129}Xe isotope). During the optical pumping phase, the cell was placed in the fringe field ($\sim$100 Gauss) of the 4.7 Tesla Bruker small animal MR imager in which the NMR experiments were performed. A hot air oven maintained the cell at about 100°C. Circularly polarized 795 nm light from two Ga-Al-As multistripe diode lasers (manufactured by Optopower, Inc.) optically pumped the $5^2S_{1/2}$ to $5^2P_{1/2}$ transition (the D1 spectral line) of the rubidium atoms creating an electron spin polarization. These atoms then polarized the nuclei of the ^{129}Xe atoms through spin-exchange collisions. After about 20 min, the cell was removed from the oven and laser beam, and cooled to room temperature. The ^{129}Xe gas was cryopumped, using liquid nitrogen, into a second coated Pyrex cell with insignificant loss of ^{129}Xe polarization [38]. When this cell was warmed back up to room temperature, the polarized ^{129}Xe gas was ready to be released into the sample container.

3.3.2 Preparation of Test Solutions

The samples investigated were: freshly extracted human blood, plasma, hemoglobin solution, lysed red blood cell membranes (RBC "ghosts") in solution, and bovine serum albumin (BSA) solution. In each case, 25 ml of liquid were placed in a 60 cc capacity plastic syringe, which served as a sample container. Approximately 0.5 cc of sodium heparin per 25 ml of blood was added to prevent clotting. The samples of blood derivatives were prepared as follows. Plasma samples were obtained by centrifuging blood. The hemoglobin and red blood cell ghost samples were extracted

from fresh citrated (CDP) human blood by a standard washing and centrifuging procedure. The bovine serum albumin (BSA) solution was made by dissolving powdered BSA (Sigma Chemicals) in deionized water at a concentration of 5 mg/ml.

The samples were either oxygenated or partially deoxygenated. The oxygenated samples were produced by flushing a mixture of 95% O_2 and 5% CO_2 six times through the sample syringe. The partially deoxygenated samples were produced by flushing six times with 95% N_2 and 5% CO_2. The delay between blood withdrawal and the NMR measurements was less than 3 hours for all the samples. The blood samples were measured at room temperature but kept on ice during the time between measurements. Because of the gas space created when the xenon was introduced, the oxygenation levels changed from the initially prepared values. Under *in vivo* conditions, the average normal arterial oxygen saturation level, $S(O_2)$, of the hemoglobin is 97.5% at a partial pressure of oxygen, $P(O_2)$, of 100 mm Hg; and the venous oxygen saturation level is 75% at a $P(O_2)$ of 40 mm Hg [105]. Values for $S(O_2)$ and $P(O_2)$ for our samples were estimated using temperature-dependent oxygen dissociation curves, and in some cases were directly measured using a co-oximeter. The estimated values for these two parameters agreed well with the directly measured values. Thus the hemoglobin in the deoxygenated blood was less saturated than normal venous blood, and the hemoglobin saturation level of the oxygenated blood sample was approximately the same as normal arterial blood. The partial pressure of oxygen in the deoxygenated case was much less than venous conditions, while the partial pressure in the oxygenated case approximated normal venous conditions. In the case of the oxygenated plasma sample, the higher final oxygen partial pressure was a result of some residual oxygen bubbles in the syringe before introduction of the xenon.

Polarized ^{129}Xe gas introduced into the sample container expanded the enclosed volume in the syringe to 58 cc. The gas-sample mixture was vigorously agitated; for all sample types a fine foam was formed that appeared stable for more than 1 minute. This foam provided a very large surface area for interaction between the gas and the sample, allowing xenon gas to be dissolved quickly into the sample, and depolarized ^{129}Xe in the sample to be replenished by the gas reservoir. In our analysis, the

blood foam mixtures were treated as representative of xenon dissolved in bulk blood. This assumption is supported by our observation of similar NMR spectra from ^{129}Xe dissolved in bulk blood (from a measurement with thermally polarized ^{129}Xe and no foam) and ^{129}Xe dissolved in blood foam. After the series of experiments, samples of the blood used were checked under a microscope and it was verified that less than 5% of the red blood cells had hemolysed.

Once the polarized ^{129}Xe gas was mixed with a sample, the syringe was placed in a solenoid RF coil at the center of the spectrometer. Two sets of experiments were performed corresponding to the initial conditions of either $G \gg B$ or $G \sim B$. The case $G \gg B$ was the natural initial condition in our experimental setup. The case $G \sim B$ was produced by greatly reducing the ^{129}Xe gas magnetization by a series of four 90° pulses and field gradient crushers (following the saturation method in Ref. [83]) applied immediately prior to the measurement of $G(t)$ and $B(t)$. In addition to providing a consistency check, the case $G \sim B$ offers the advantage of analysing the simpler and higher signal-to-noise ratio gas resonance.

3.3.3 MR Pulse Sequence

A series of small flip angle RF pulses read out the ^{129}Xe magnetization. Since the frequency of dissolved ^{129}Xe in our samples was ~200 ppm downfield from the frequency of the ^{129}Xe gas, we increased the signal-to-noise ratio (SNR) by alternating the frequency of the transmitter and receiver between 0 and 207 ppm relative to the gas; that is, alternately on resonance with the gaseous and dissolved ^{129}Xe signals. This technique allowed for a narrower detection bandwidth and better utilization of the spectrometer's dynamic range. The duration of the rectangular read pulses was 87 μs, calculated to minimize the RF excitation 207 ppm away. Thus, each RF pulse selectively excited only one ^{129}Xe phase, gas or dissolved, without disturbing the other. For each run of the experiment, with a particular xenon-sample mixture, a total of 64 free induction decays (FIDs) were acquired; 32 FIDs each at the gas and dissolved phase frequencies as shown, for example, in Fig. 3-1. The interpulse delay was either 4 or 2 s. Crusher field gradients were applied after each signal acquisition.

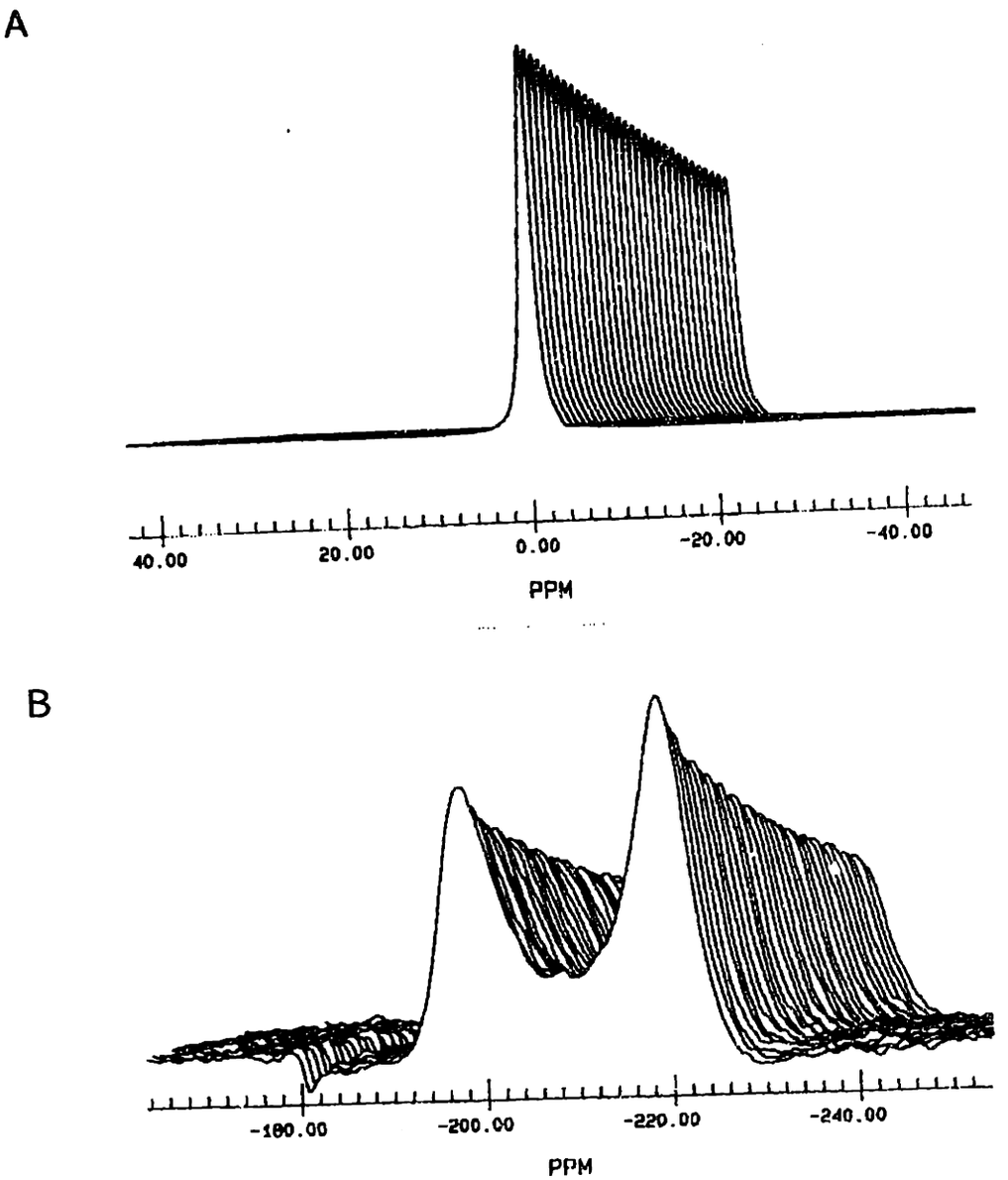

Figure 3-1: Observed time series (2 s intervals) NMR spectra of laser polarized ^{129}Xe dissolved in a sample containing oxygenated blood foam. (A) gas resonances, and (B) blood resonances. The first spectra are in the plane of the paper.

Because the laser polarization technique produces a highly non-thermal, and thus non-recoverable ^{129}Xe spin-polarization, RF pulses with small flip angles are necessary to interrogate but not destroy the ^{129}Xe magnetization. The RF pulse amplitudes were set to provide flip angles of ~2.5° on the gas and ~15° on the ^{129}Xe dissolved in the sample. The flip angle on the gas could be smaller than that on the dissolved phase because of the significantly larger ^{129}Xe magnetization in the gas. For the case $G \sim B$, the flip angles were set to ~15° for both the gas and dissolved ^{129}Xe phases. These angles were calibrated by measuring the magnetization destruction from a fast series of pulses and crusher gradients on a laser polarized ^{129}Xe gas sample in a coated glass container with a T_1 longer than 2 hours.

3.4 Results and Analysis

Typical NMR resonances observed for laser polarized ^{129}Xe dissolved in foam mixtures of blood, hemoglobin solution, red blood cell ghosts, plasma, and bovine serum albumin are shown in Figure 3-2. Two peaks, of about the same area, at 197 ppm and 220 ppm were observed for the blood samples. One narrow resonance at 197 ppm was observed in the plasma. All frequencies are in ppm relative to the ^{129}Xe gas resonance frequency at 0 ppm, not shown in Figure 3-2. We conclude that the 197 ppm resonance is ^{129}Xe dissolved in blood plasma, and the 220 ppm resonance is ^{129}Xe in red blood cells. Both ^{129}Xe blood resonances have broadened widths compared to the single component plasma case, indicating exchange between the components, and/or bulk magnetic susceptibility effects. The ghost sample has only one peak at 200 ppm with a broad pedestal which is probably due to residual hemoglobin. The albumin solution has one peak at 192.5 ppm, shifted upfield from the plasma. Table 3.1 summarizes the measured linewidths and chemical shifts for all the samples.

The chemical shifts of the blood RBC and hemoglobin solution ^{129}Xe resonances differ from the previously measured value of 229.5 ppm for ^{129}Xe in hemoglobin [97], presumably because of fast exchange with the surrounding liquid. According to solubility coefficients of xenon in red blood cells and plasma, 75% of the dissolved

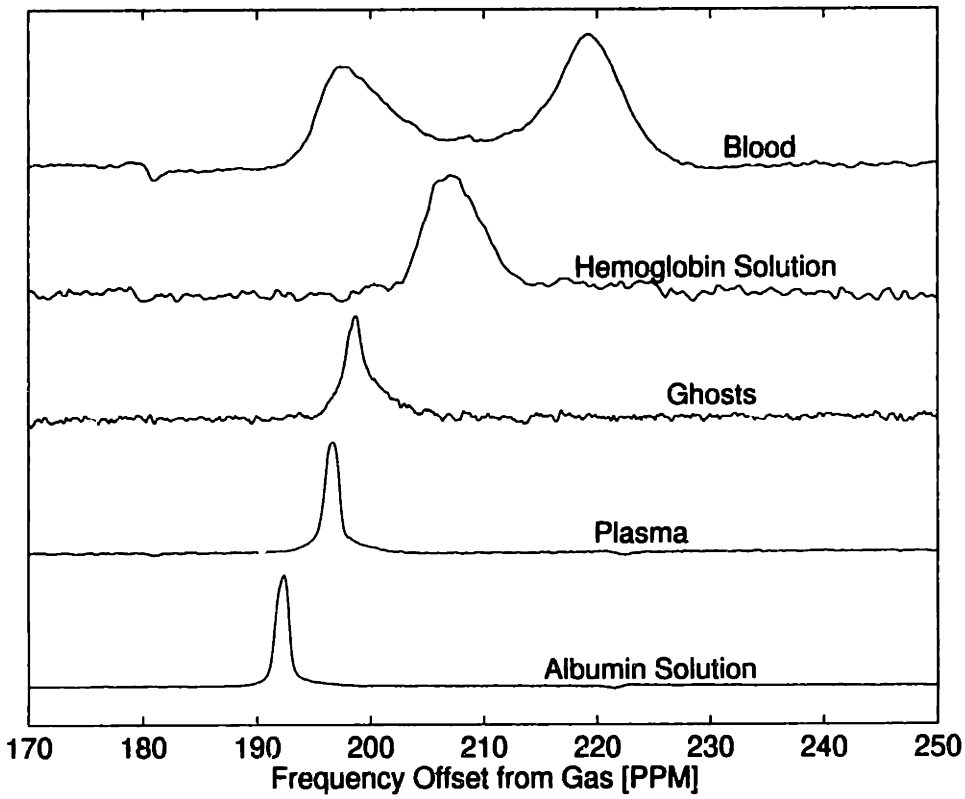

Figure 3-2: NMR spectra of laser polarized ^{129}Xe dissolved in foam preparations of blood, hemoglobin solution, red blood cell ghosts, plasma, and BSA. The small antiphase peak at ~180 ppm in the blood spectrum is an artifact caused by the gas peak folding in.

xenon in blood resides in the RBCs [23]; with 45% of the total amount adsorbed on the hemoglobin (oxygenated or deoxygenated) [91]. We infer that ^{129}Xe on the hemoglobin is in fast exchange with a subpopulation of the intracellular fluid, which in turn is in slower exchange (through the RBC membrane) with extracellular plasma. From the measured resonance linewidths, we estimate that the xenon exchange time between the RBC and plasma is >1 ms.

Figure 3-1 shows time resolved series spectra from the ^{129}Xe gas phase and from ^{129}Xe dissolved in oxygenated blood, obtained at an offset from the gas spectra collection times. From such data, the various ^{129}Xe magnetization decay rates can be determined, as discussed above. Since the two ^{129}Xe blood resonances were observed to decay at the same rate, they were treated as one population. The first spectrum of each experimental run was phase corrected, with this phase correction fixed for the

Sample	Oxygenation	Peak	Line width FWHM [Hz]	Chemical shift relative to gas [ppm]
Blood	oxygenated	RBC	289±12	220.0±0.2
		plasma	250±22	196.7±0.3
	deoxygenated	RBC	336±28	219.6±0.3
		plasma	292±29	197.0±0.4
Hb solution	oxygenated		300±90	208.8±2.0
	deoxygenated		305±56	207.6±1.1
RBC ghosts			157±30	200.2±0.4
Plasma	oxygenated		72±8	197.3±0.1
	deoxygenated		70±11	196.8±0.1
BSA			44.4±2.6	192.5±0.03

Table 3.1: Summary of ^{129}Xe linewidths and chemical shifts relative to the gas peak. The values given are the mean and standard deviation from eight consecutively acquired spectra.

rest of the run. The ^{129}Xe peak areas were calculated for a fixed spectral width for each experimental run, and were assumed to yield values proportional to the ^{129}Xe magnetizations in the blood and gas phases represented by $B(t)$ and $G(t)$ respectively.

The observed decay of the ^{129}Xe NMR peak integrals for blood, plasma, and gas phases for the initial conditions ($G \gg B$) are shown in Figure 3-3. The observed gas decays for the case $G \gg B$ were monoexponential and were fitted with less than a 2% error in μ_2. The observed monoexponential behavior confirmed that, for $G \gg B$, the term $k_B B$ is negligible in the gas rate equation, Eq. 3.1. The time behaviors of the integrals of the ^{129}Xe blood and plasma peaks were fitted using the Marquardt-Levenberg algorithm to a biexponential function (Eq. 3.4) in which one of the decay rates was constrained to be the observed gas decay rate, μ_2.

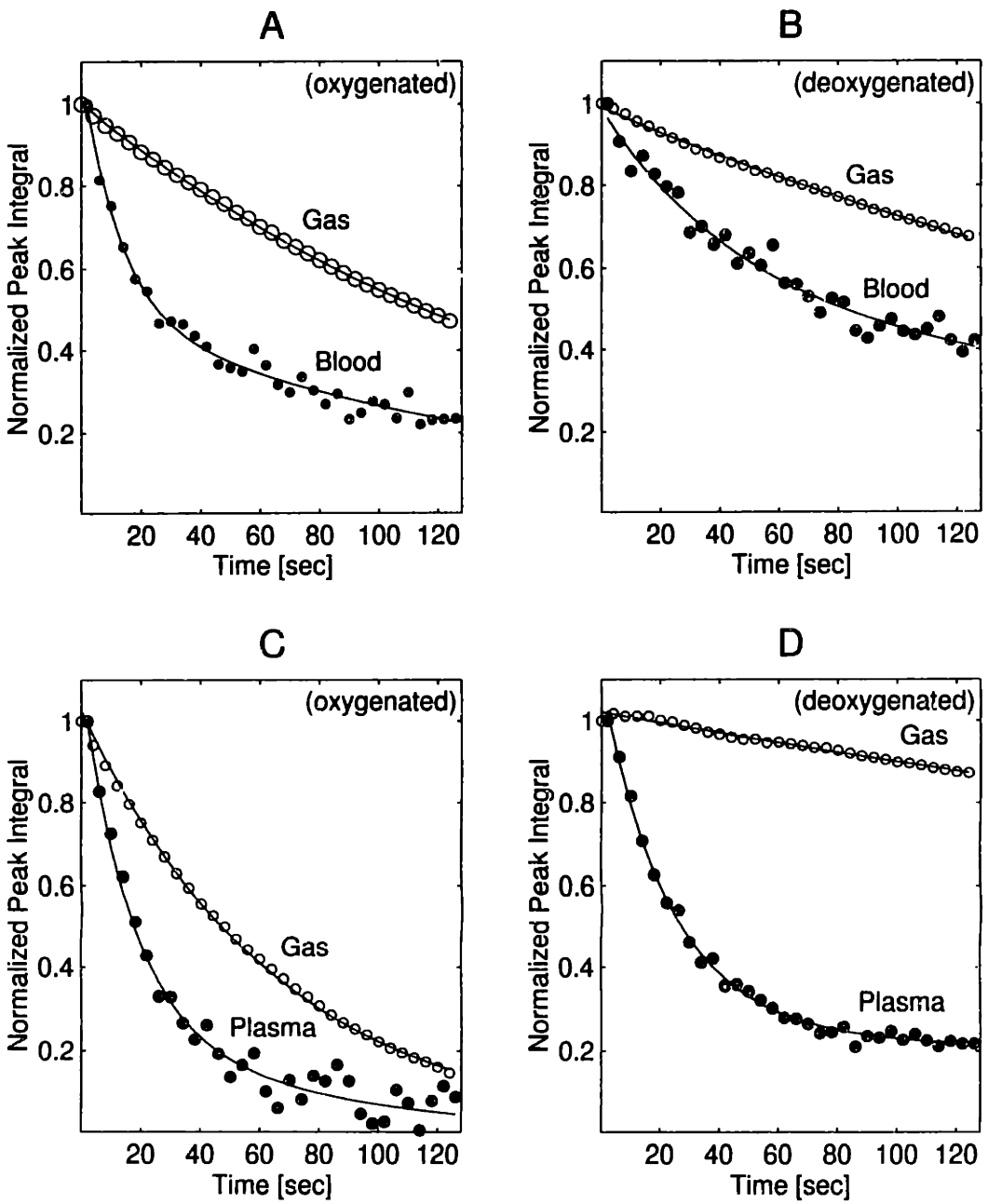

Figure 3-3: Observed decay of NMR peak integrals for laser polarized ^{129}Xe dissolved in foams with $G \gg B$. (A) oxygenated blood foam, (B) deoxygenated blood foam, and (C) oxygenated and (D) deoxygenated plasma foam. Decay of the accompanying ^{129}Xe gas component (○) is shown above the blood and plasma signals (●). The gas signals were fitted to monoexponentials and the blood and plasma signals were fitted to bi-exponential functions (solid lines) with one exponential rate given by the observed gas signal decay rate. All ^{129}Xe peak integrals were normalized to the first point in the time series.

From such 3-parameter fits, the second exponent, $\mu_1 = R_B - (\ln\cos\theta_B)/\tau + k_B$, was found. Table 3.2 summarizes the measured characteristic decay times corrected for the RF read pulses, $(\mu_1 + \frac{\ln\cos\theta_B}{\tau})^{-1}$. These corrected decay times represent a lower limit on ^{129}Xe T_1 in the dissolved phase, see Eq. 3.8.

Similar measurements were performed for the initial condition $G \sim B$. This condition was obtained, as described earlier, by reducing the gas magnetization G with four 90° pulses applied immediately prior to the acquisitions. Figure 3-4 shows the ^{129}Xe blood, hemoglobin, and gas phase peak integrals for the initial conditions $G \sim B$. For this condition, the dissolved phase decay rate is best obtained from the gas phase behavior due to the higher signal-to-noise ratio. Thus, the gas signal was fitted to a biexponential, and the low signal from the dissolved phase was not analyzed. The inital rise (0-10 s) of the gas signal and the fall of the blood/hemoglobin signal indicates ^{129}Xe magnetization leaving the dissolved phase and entering the gas phase. In the blood samples, $(\mu_1 + \frac{\ln\cos\theta_B}{\tau})^{-1}$ decreased upon oxygenation, consistent with results from the experiments where initially $G \gg B$ (see Table 3.2).

(1) Sample	(2) Oxygenation	(3) Initial Conditions	(4) $P(O_2)$ [mm Hg]	(5) $S(O_2)$ [%]	(6) $(\mu_1 + \frac{\ln\cos\theta_B}{\tau})^{-1}$ [s]	(7) std. deviation [s]	(8) T_1 [s]
Blood	oxygenated	$G \gg B$	40[a]	97[a]	17.6	+10.6/-4.8	17.6-22.9
		$G \sim B$	40.1	96.7	15.8	+5.2/-3.0	15.8-25.9
	deoxygenated	$G \gg B$	13[a]	58[a]	76	+∞/-42	>76
		$G \sim B$	12.9	58.1	40.6	+1.8/-1.6	>40.6
Plasma	oxygenated	$G \gg B$	50[a]	n/a	23.1	+8.4/-6.5	23.1-96.2
	deoxygenated	$G \gg B$	0[a]	n/a	30.4	+2.5/-2.5	>30.4
Hb solution	oxygenated	$G \sim B$	40[a]	96[a]	14.5	+4.1/-2.9	>14.5
	deoxygenated	$G \sim B$	13[a]	58[a]	13.5	+0.9/-1.2	>13.5

[a] estimated values.

Table 3.2: Summary of measured ^{129}Xe magnetization relaxation times for all samples. Column (6) shows the lower limit of T_1; column (7) shows the calculated one standard deviation error on the lower limit of T_1; column (8) shows the calculated range for T_1 from Eq. 3.8.

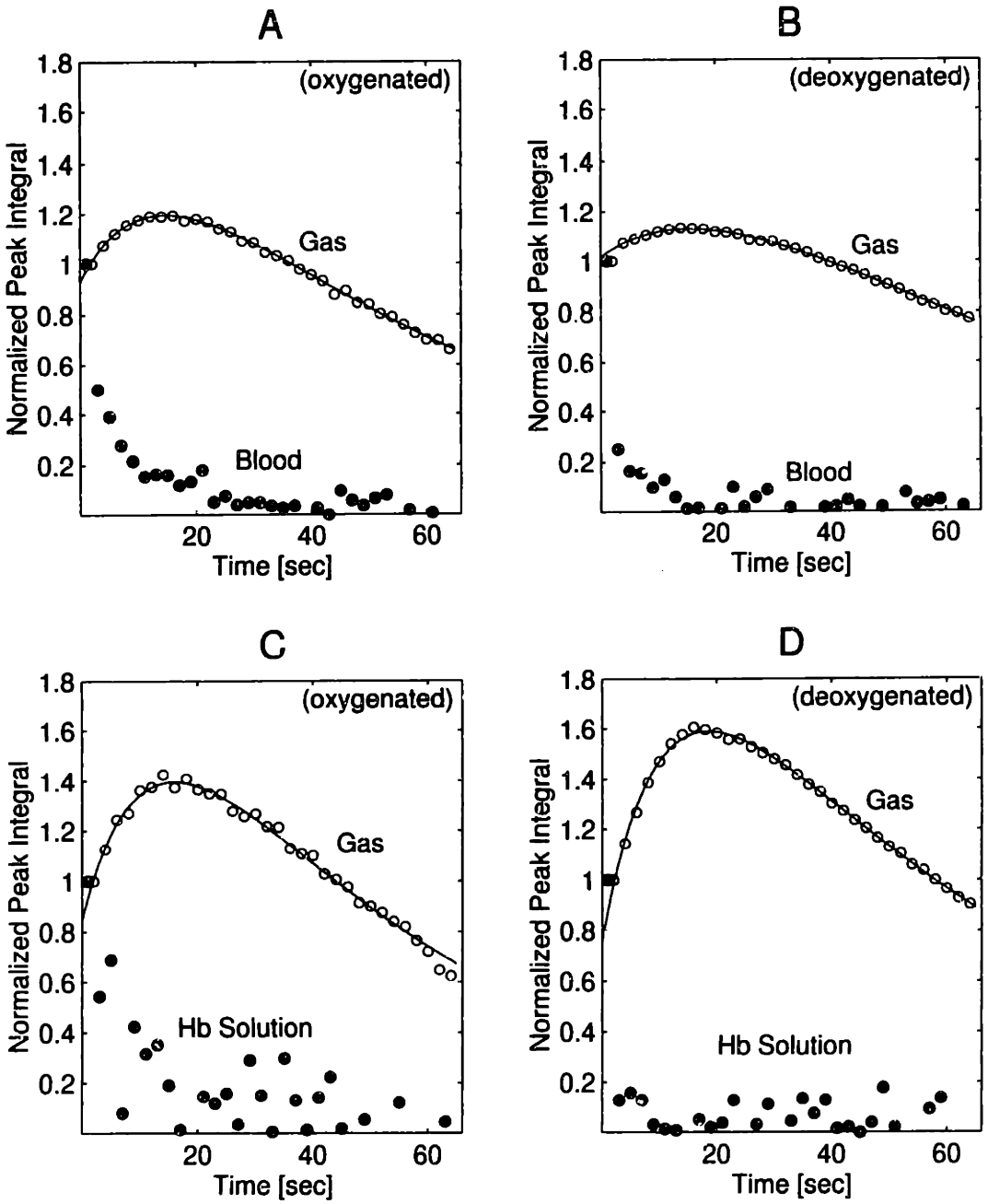

Figure 3-4: Observed decay of NMR peak integrals for laser polarized ^{129}Xe dissolved in foams with $G \sim B$ The gas phase ^{129}Xe magnetization was greatly reduced by RF pulses prior to acquisition. (A) oxygenated blood foam, (B) deoxygenated blood foam, and (C) oxygenated and (D) deoxygenated hemoglobin foam. Decay of the accompanying ^{129}Xe gas component (o) is shown above the blood and plasma signals (•). The gas signals were fitted to bi-exponential functions (solid lines). All ^{129}Xe peak integrals were normalized to the first point in the time series.

The noise error of each ^{129}Xe dissolved phase spectrum was estimated by calculating the average noise per point for a section of the off-resonant baseline. The appropriate average noise was added to the peak integral value, and provided the noise seed for the non-linear curve-fit. Uncertainties in the fitted μ_1 values were ascertained using standard χ^2 procedures for non-linear least-squares fits [12]. Specifically, μ_1 was varied until χ^2 of the three parameter fit deviated by 3.67 from the minimum χ^2 value, thus giving the one standard deviation errors (70% confidence limit) of the lower limit for T_1 shown in Table 3.2, column (7).

An additional, very early transient behavior (< 4 sec) is evident in the data with $G \sim B$ initial conditions. As shown in Fig. 3-4, the earliest data points in each decay indicate a rapid response to the large change in G induced by the 90° pulses. The time scale for the rapid return to pseudoequilibrium between G and B depends on the diffusion time of xenon atoms to the liquid/gas interface. After pseudoequilibrium is destroyed by making $G \sim B$, the ^{129}Xe polarization contained in the thin bubble walls of the blood/hemoglobin foam will quickly diffuse out of the liquid phase to re-establish $G \gg B$. Thus, the ^{129}Xe liquid phase signal will drop suddenly and the ^{129}Xe gas signal will rise quickly. Further from the gas/liquid interface, the dissolved ^{129}Xe magnetization will not be as tightly coupled to the gas behavior, and will decay with the slower rate, μ_1. Thus the behavior characterized by μ_1 will only be evident once the transient return to pseudoequilibrium is complete. Note that even though the ^{129}Xe blood signal behavior in Fig. 3-4A (oxygenated) appears to have a longer time constant than the behavior in Fig. 3-4B (deoxygenated), the intrinsic T_1 information is contained in the points subsequent to the first few points. This information is reflected (with better SNR) in the ^{129}Xe gas behavior, which yields instead a longer T_1 in Fig. 3-4B (deoxygenated). For the case $G \gg B$ there is no such very early transient behavior because the system begins (and remains) in a pseudoequilibrium between G and B.

To illustrate the rapidity of ^{129}Xe exchange between the gas and liquid ^{129}Xe phases, and to examine the transient response to a large change in G, a 180° pulse was applied to the gas phase of a xenon-plasma system halfway through the polarization

decay time series. The pulses on each phase were chosen so as not to excite the other phase. Fig. 3-5 shows the rapid change ($\sim$ 1 sec) in the sign of the ^{129}Xe plasma peak after the 180° inversion pulse on the gas. This change in sign reflects, because of gas-plasma exchange, the magnetization inversion of the gas reservoir source.

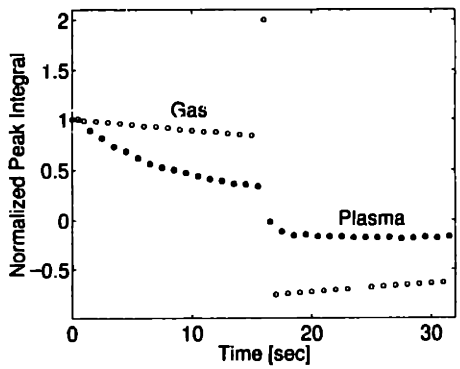

Figure 3-5: Observed inversion of magnetization from polarized ^{129}Xe gas and from ^{129}Xe dissolved in plasma. At t = 16 sec, a 180° pulse is placed on the gas resonance. The plasma ^{129}Xe peak passed through zero and changed sign because of the plasma ^{129}Xe exchange with the inverted ^{129}Xe magnetization of the gas reservoir.

The gas phase xenon above each of the samples decayed differently in the presence of the four types of blood/plasma samples as can be seen in Fig. 3-3; that is, μ_2 differed for the four cases. This difference is probably due to the different partial pressures of gas phase 0_2 which is paramagnetic and will cause ^{129}Xe depolarization [52]. That these different values of μ_2 would nevertheless lead to the same extracted value for R_B was explicitly tested as follows. Two measurements on an albumin-xenon sample were made using different flip angles on the ^{129}Xe gas phase, effectively changing the gas decay time constant R'_G (R'^{-1}_G= 94 sec and 330 sec). The extracted albumin-phase ^{129}Xe decay rate was similar for the two R'_G values. Similarly, ^{129}Xe NMR measurements using a different pulse delay (τ = 2 sec instead of 4 sec) were made on a plasma sample, as well as on an oxygenated blood sample. Consistent dissolved phase ^{129}Xe decay rates were found for the two pulse delays.

Our measurements suggest that ^{129}Xe retains its polarization for a significantly longer time in deoxygenated blood foam than in oxygenated blood foam. The measured characteristic decay times corrected for the RF pulses, $(\mu_1 + \frac{\ln\cos\theta_B}{\tau})^{-1}$ are

summarized in Table 3.2. Since the solubility of xenon does not depend on the partial pressure of oxygen [91], the values of k_B should be approximately the same for a given type of sample regardless of oxygenation. Hence, the comparison of the measured ^{129}Xe magnetization decay rates as a function of oxygenation should reflect the actual trend of T_1. The plasma samples also follow this trend. The measured decay times $(\mu_1 + \frac{\ln \cos \theta_B}{\tau})^{-1}$, are lower limits to the intrinsic relaxation time T_1; the upper limit for T_1 is determined according to Eq. 3.8 with $\mu_{1(low)}$ given by μ_1 found in the deoxygenated cases assuming the exchange rates to be the same for a given sample, independent of oxygenation level. The calculated ranges for T_1 in the dissolved phase for each of the samples are listed in Table 3.2.

3.5 Discussion

Oxygenation levels do not significantly affect the ^{1}H T_1 in whole blood or plasma and when red blood cells are lysed, ^{1}H T_1 in the solution increases with oxygenation [41, 70]. Thus, it may be surprising that the measurements reported here indicate that T_1 of ^{129}Xe in blood decreases with oxygenation. This trend may be due to motion past paramagnetic sites created by O_2 dissolved in the aqueous solution, a depolarizing effect much like that of O_2 on ^{129}Xe in the gaseous state [52]. This effect may be more pronounced for ^{129}Xe than for ^{1}H due to the much shorter typical ^{1}H T_1 which may mask any oxygenation effect. Deoxygenated hemoglobin has 4 unpaired electrons [79], which may compete with the paramagnetic oxygen sites in solution in determining the T_1 trend with oxygenation. The absence of an oxygenation T_1 trend in the hemoglobin solutions may be due to a balance between these effects, or to the long times spent in the non-polar binding sites of ^{129}Xe on hemoglobin. The reduced xenon and hemoglobin mobility in intact RBC compared to lysed cell solutions may create a subpopulation (intracellular) with a weak oxygenation dependence in exchange with a subpopulation in the plasma with a stronger oxygenation dependence. These possibilities require further study.

Exchange and oxygenation are two major issues to be considered when comparing

the results reported here with previous work. Earlier *in vitro* measurements of the T_1 of polarized ^{129}Xe dissolved in blood found an oxygenation-T_1 trend opposite to that reported here. However, these preliminary measurements did not adequately account for gas-liquid exchange [3]. Other experiments (*in vivo* and *in vitro*) [89, 104, 88, 14] reported only effective T_1s because the measurements had xenon and oxygen exchange between dissolved and gas phases. From these measurements, the effective T_1 of resonances attributed to blood phase ^{129}Xe range from 5 sec to $\sim$ 50 sec. Also, no ^{129}Xe T_1 oxygenation trends were determined by these experiments. A thermal *in vitro* ^{129}Xe T_1 measurement [4] in a closed system found different T_1 values for plasma (10 sec) and RBC (4.5 sec), and no significant oxygenation trend. However, this experiment required several hours of acquisition time during which the $P(O_2)$ is suspected to have changed, and the blood components to have sedimented and degraded. To avoid these uncertainties, the $P(O_2)$ and $S(O_2)$ in our closed system experiments were measured explicitly, and laser polarized ^{129}Xe was used to allow rapid measurement and hence insignificant blood sedimentation and degradation.

Systematics that could affect our T_1 measurements include: (i) coarsening of the foam; and (ii) RBC depletion in the foam. Foam coarsening would reduce k_B and B during the measurement period, thereby causing our model to underestimate T_1. RBC depletion (and hence plasma enrichment) in the foam could cause the extracted T_1 to overestimate the T_1 of *in vivo* blood. However, no visual evidence of either foam coarsening or RBC depletion (as indicated by the color of the foam) was observed during our measurements; also the decay of G was well fitted by a monoexponential implying time-independent exchange constants thus no foam coarsening.

The correspondence between the blood foam system studied here and *in vivo* blood requires further study. Yet, it should be noted that generally *in vivo* measurements of the ^{129}Xe blood phase T_1 would be in an open system, and therefore would probably not be reliable. *In vitro* measurements can be made in closed systems, and thus allow the determination of a true T_1. Our *in vitro* measurements indicate that the ^{129}Xe blood T_1 decreases with increasing blood oxygenation in this experimental setup. The dependence of ^{129}Xe T_1 on the oxygenation level in the blood may

provide a way to detect local oxygenation levels as an indicator of neuronal activity. Our measured values for the ^{129}Xe blood T_1s were made with partial pressures of oxygen and hemoglobin oxygen saturation levels that differ from *in vivo* conditions. Nevertheless, if these results are extrapolated and applied to *in vivo* conditions, the ^{129}Xe T_1 is about 5 sec, or roughly a lung-brain circulation time. This suggests that a significant amount of inhaled polarized ^{129}Xe could be transported to distal tissues such as the brain, barring any unforseen relaxation surfaces along the way. The measurement technique using a foam gas-liquid exchange interface may also be useful for studying foam coarsening and other liquid physical properties [42].

Acknowledgements for this chapter

This work was carried out in collaboration with Ching-Hua Tseng and Luigi Nascimben [98, 82]. We are indebted to Robert Mulkern for valuable discussions and suggestions. We also thank Samuel Patz and Daniel Williamson for useful comments and the members of the Ingwall Lab for providing blood samples.

Chapter 4

Myelin in vitro

4.1 Objectives

This chapter records some NMR measurements made on a preparation of purified myelin. A spectrum of ^{129}Xe in the myelin solution was obtained for information about binding and relaxation interactions of xenon and myelin. Ultimately any applications of laser-polarized ^{129}Xe MR in white matter will depend not only on the longitudinal magnetization state of the xenon reaching the brain, but also on the character of these interactions. The same myelin solution furnished ^{1}H transverse relaxation decay curves, providing an estimate of the effect of myelin on T_2 of the surrounding water. This is useful for the compartmental assignment discussed in the next chapter.

Purified myelin was prepared from the brains of six 9-week old rats according to the protocol in Ref. [77]. This procedure preserves much of the multilammelar structure of the myelin bilayers and the proteins. Each rat brain weighed about 1.6 g. According to Ref. [77], the yield from a 9-week old rat by this method is approximately 40 mg of purified myelin. Thus the final volume of 6 ml solution was at a concentration of $\sim$40 mg/ml.

4.2 ^{129}Xe Spectroscopy

Measurements were first performed on ^{129}Xe in olive oil. Olive oil is often used as a model for lipid membranes in solubility studies because the efficacy of general anesthetics has been found to match very closely with their solubility in olive oil. T_1 in the olive oil at a xenon pressure of 2.5 atm was measured to be 15 s; we also measured 5.4 s for T_2, and 0.2 μ^2/ms for the diffusion constant. Then thermally polarized ^{129}Xe was bubbled through 2.5 ml of the myelin solution for a few minutes. The final xenon pressure was adjusted to 2.5 atm.

The partition coefficient for xenon in myelin was roughly calculated from the partition coefficients in brain and water at 20°C from Ref. [23] (see Table 4.1). Myelin represents approximately 50% of the dry weight of white matter [77] which is approximately 20% of the wet weight. If we assume that the partition coefficient of the other 50% of dry material in white matter is similar to that of the dry material in grey matter, the partition coefficient for myelin compared to water turns out to be approximately 12.5 ml/g. From Table 4.1 the partition coefficient for xenon in olive oil compared to water is 17.5 ml/g. The values of the coefficients at 37°C tend to be lower than those at 20°C by about 15-30%.

Temp.	water [ml/ml]	olive oil [ml/ml]	white matter [ml/g]	grey matter [ml/g]
20°C	0.122	2.14	0.26	0.18
37°C	0.085	1.83	0.22	0.14

Table 4.1: Xenon partition coefficients (relative to gas) in brain, olive oil and water, from Ref. [23].

The amount of xenon in the myelin solution can be calculated from the partition coefficent and concentration to be approximately 9% of the amount in the same volume of olive oil, with one third of the total volume of xenon in the myelin solution within the myelin itself. We tried to maximize the SNR by optimal signal averaging, i.e. by choosing appropriate flip angles (θ) and recovery times (τ). The equation describing the time evolution of longitudinal magnetization in the absence of RF

pulses is:

$$M(t) = M_i e^{-t/T_1} + M_0(1 - e^{-t/T_1}) \tag{4.1}$$

where M_i is the initial value and M_0 is the value at equilibrium. In the steady state, after each RF pulse,

$$M_i = M \cos\theta \tag{4.2}$$

which results in the equation for M:

$$M = M_0 \frac{1 - e^{-\tau/T_1}}{1 - e^{-\tau/T_1}\cos\theta}, \tag{4.3}$$

and the SNR from a total measurement time $N\tau$ is:

$$S = \sqrt{N} M \sin\theta \tag{4.4}$$

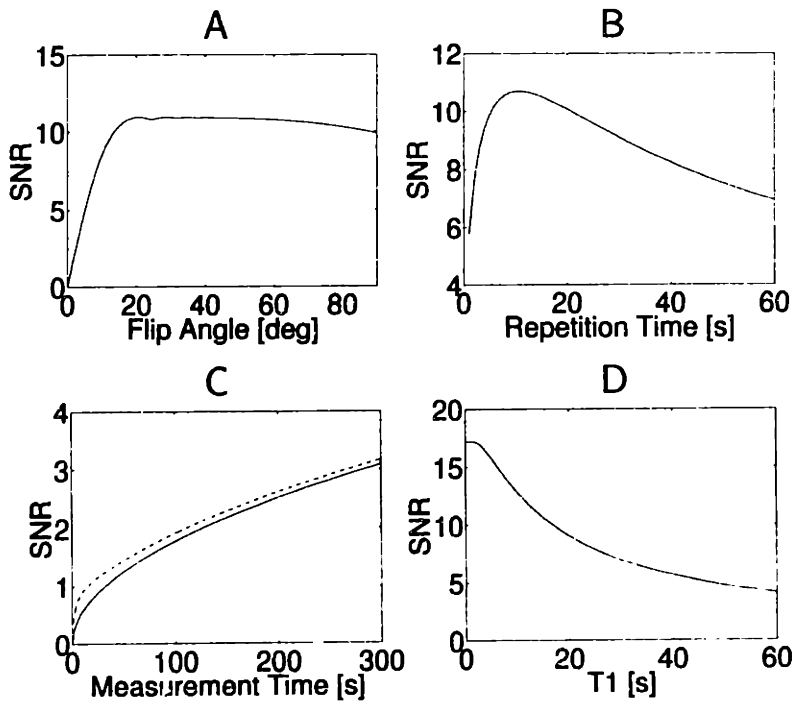

Figure 4-1: Averaging to increase SNR. (A) Maximum SNR obtainable after one hour signal averaging versus pulse flip angle. (B) SNR after one hour versus repetition time for flip angle of 65°. (C) Steady state solution versus exact solution (dashed line). In (A), (B) and (C) T_1=15 s. (D) SNR after one hour versus T_1 for flip angle of 65° and repetition time of 10s.

The solution for the SNR before steady state is achieved is given in the appendix. Figure 4-1 shows how we chose a flip angle of 65° and a repetition time of 10 s for our measurements. The estimated longitudinal relaxation time used for the calculation was that of olive oil, 15 s. Figure 4-1D shows that the decrease in SNR for the chosen sequence of pulses would be by maximally a factor of 2 if T_1 of the solution were much longer than 15 s.

The ^{129}Xe peak from the xenon-myelin solution with 1024 acquisitions was wider than the peak from the xenon-olive oil solution (16 acquisitions) by approximately a factor of 6 (240 Hz vs. 30 Hz). Figure 4-2 shows the spectra obtained. The peak from the myelin solution is at ~193 ppm downfield from the gas peak. The ratio of peak areas, adjusted for the number of acquisitions for each sample, approximately corresponds to the ratio of xenon concentrations.

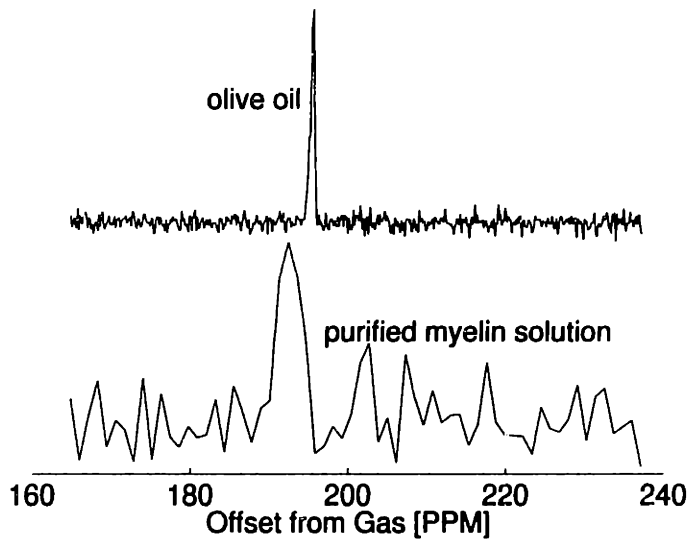

Figure 4-2: Spectra from ^{129}Xe in myelin solution (1024 averages) and in olive oil (16 averages).

To elucidate the origin of the short T_2 observed in the myelin solution, additional measurements should be performed in the same experimental setup, namely xenon dissolved in the following liquids: 1. water, 2. olive oil and water emulsion at different concentrations, and 3. isolated myelin lipids in solution.

4.3 ^{1}H Relaxation

The myelin preparation used in the previous section was used here too, at a slightly higher concentration. A transverse relaxation decay curve was obtained using the CPMG pulse sequence with an echo spacing of 0.5 ms. One data point is acquired at the center of every even echo resulting in 8192 data points measured over 8.2 s. No quantitative dependence on the echo spacing was observed in our measurements.

The CPMG curves obtained in the experiment were fitted using the Non-Negative Least Squares (NNLS) method as first implemented in the context of NMR relaxation by Whittal and MacKay [107] from an algorithm by Lawson and Hanson [62]. 286 logarythmically spaced time points were chosen so as to cover all the possible T_2 times in the sample. The data is fitted in a least squares sense to all the possible exponentials with smoothing of the resulting "relaxogram" incorporated into the algorithm. The method has been tested for accuracy and is now commonly used for analyzing multiexponential relaxation, but T_2 values that are close together cannot be well separated. The data and analysis results for the myelin sample are shown in Fig. 4-3. The relaxation times for the myelin sample were {30 ms, 130 ms, 275 ms, 1000 ms} with relative proportions of {2%, 18%, 77%, 3%}.

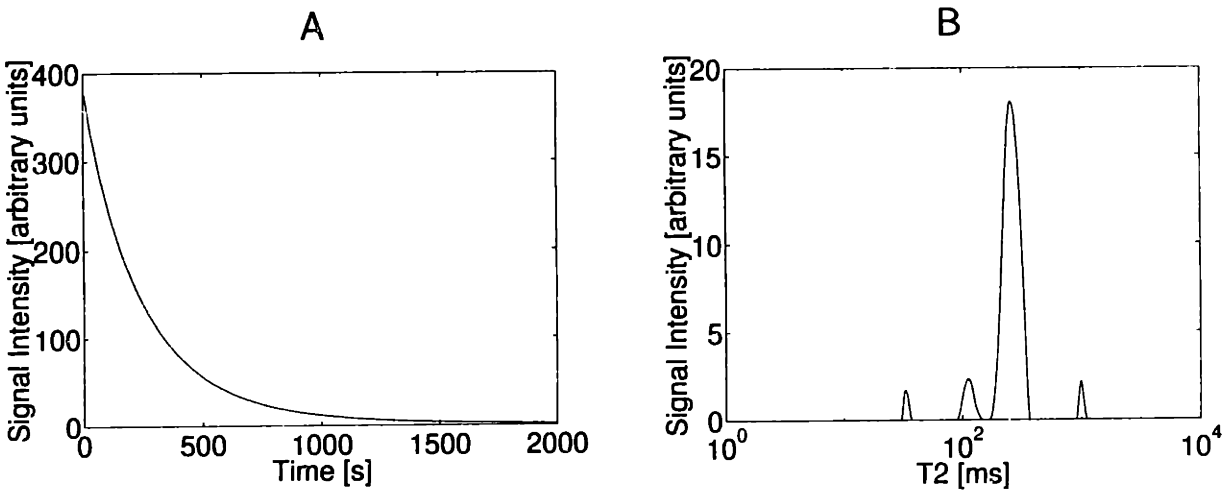

Figure 4-3: Decomposition of transverse relaxation decay curves. (A) Transverse relaxation decay curve from CPMG sequence applied to myelin preparation. (B) NNLS decomposition of decay curve.

4.3.1 Interpretation

In this experimental setup, the free water has to be in exchange with the bound water otherwise the relaxation time would be on the order of 1.5 s. If we assume that the exchange is fast because the majority of the signal is from one T_2 component, the observed relaxation rate, R, is then a weighted average of the relaxation rate of the water while bound, R_b and the relaxation rate of free water, R_f:

$$R = P_b R_b + P_f R_f, \tag{4.5}$$

where P_b is the proportion of bound water and P_f is the proportion of free water. If the concentration of myelin is represented by C_m in units of mg myelin per mg total weight, and the weight of bound water per mg of myelin is p, then we get the following equations for P_b and P_f:

$$\begin{aligned} P_b &= \frac{pC_m}{1 - C_m}, \\ P_f &= \frac{1 - C_m - pC_m}{1 - C_m}. \end{aligned} \tag{4.6}$$

Using this simplified model, we can estimate the expected relaxation time for water associated with myelin under *in vivo* conditions. Let us group the variables R_b and p together and call $x = R_b p$ the relaxivity of myelin. Eqs. 4.5 and 4.6 combine to give Eq. 4.7 under the condition $C_m \ll 1$:

$$R \simeq xR_b + (1 - pC_m)R_f\,. \tag{4.7}$$

From our experiment, we can substitute $R > 1/0.275\,\mathrm{s}^{-1}$, $R_f = 1.5\,\mathrm{s}^{-1}$ (free water) and $C_m \simeq 0.04$ mg/mg. If we assume that no more than 2 mg of water is bound to each mg of myelin ($0 < p < 2$), then the solution for x is insensitive to p and we get $x < 75\,\mathrm{s}^{-1}$.

Under *in vivo* conditions we can assume that water occupies approximately 80% by weight of the myelin sheath. In this case $C'_m \simeq 0.2$ and we can determine R' from

Eq. 4.5,

$$R' = \frac{xC'_m}{1 - C'_m} + \frac{1 - pC'_m - C'_m}{1 - C'_m} R_f \,. \tag{4.8}$$

Also the value for R' is insensitive to p, and $R' > 19.5$. From this calculation, a lower limit for the value for T_2 of intramyelinic water *in vivo* is 50 ms.

4.4 Afterword: Effect of Surface Charge on Diffusion

From electrophoretic mobility studies, Moscarello *et al.* showed that myelin vesicles created from non-plaque white matter in Multiple Sclerosis (MS) brains have a much higher negative surface charge than those from normal myelin [73]. As a result of this and other differences between normal and MS myelin vesicles, the authors concluded that myelin in MS is abnormal and consequently more readily susceptible to breakdown by any one of several environmental, immunological or infective agents.

4.4.1 Lipid Bilayer Interaction

Many different mechanisms of attraction and repulsion between lipid bilayers have been identified. At relatively large separations between the bilayers, the main forces are the electrostatic force and the van der Waals force which together form the basis for the DLVO theory of colloidal stability, after Derjaguin and Landau [28], and Verwey and Overbeek [103]. When the spacing between the bilayers becomes closer than a few nm, other non-DLVO interactions become important. These other forces are repulsive and result from water binding strongly to the surfaces (hydration forces), or from thermal fluctuation interactions (steric forces).

The electrostatic interaction is assumed to be between two infinite surfaces with fixed surface charge and a liquid with mobile charges between them [103]. The surface charge is conventionally assumed positive. The mobile charges in the liquid, both counter- and co-ions, distribute themselves in response to the electric potential. At thermal equilibrium the ions between the bilayers distribute according to Boltzmann's

equation. Following an approximation of small interactions, The three equations expressing the electrostatic force, F_{es}, in terms of the surface charge, σ, and the intermyelinic distance, x_d, can be calculated to be:

$$F_{es} = 2nkT(\cosh y_d - 1)\,, \tag{4.9}$$

$$\tanh \frac{y_d}{8} = \tanh \frac{y_0}{4} e^{-\kappa x_d}\,, \tag{4.10}$$

$$\sigma^2 = \frac{kTn\varepsilon}{\pi}(\cosh y_0 - \cosh y_d)\,. \tag{4.11}$$

with the values for the physical constants and parameters listed in Table 4.2. The parameter y_0 is proportional to the electric potential at the surface of the membrane, $y_0 = \frac{q\psi_0}{kT}$, and y_d corresponds to the potential halfway between two apposing membranes, at location x_d.

	symbol	value	units
elementary charge	q	4.803×10^{-10}	esu
Boltzmann constant	k	1.38×10^{-16}	erg Kelvin^{-1}
Avogadro constant	A_0	6.022×10^{23}	Mol^{-1}
dielectric constant for water	ε	79	
temperature	T	298	Kelvin
ionic concentration	I	150	mMol liter^{-1}
		$= 1.5 \times 10^{-4}$	Mol cm^{-3}
ion density	$n = IA_0$	9.033×10^{19}	cm^{-3}
	$\kappa = q\sqrt{\frac{8\pi n}{\varepsilon kT}}$	133.923	

Table 4.2: Values for physical constants and parameters with a role in determining the intermyelinic spacing.

The van der Waals force is a universal attraction between all atoms and molecules [103]. The force is due to the attraction between the dipoles which the interacting particles induce in each other. The attractive van der Waals force in myelin, F_{vdw} can be shown to be:

$$F_{vdw} = \frac{H}{6\pi}\left(\frac{1}{(2x_d)^3} + \frac{1}{(2x_d + 2d_{ex})^3} - \frac{2}{(2x_d + d_{ex})^3}\right)\,. \tag{4.12}$$

where H is called the Hamaker coefficient, which depends on the polarizability of the

particles in which dipoles are induced, and d_{ex} is the exclusion length (see Fig. 1-1). We will follow the authors of Ref. [50] and assign an average value of 5×10^{-14} erg to H.

Hydration forces arise from the structuring or ordering of water molecules around strongly hydrophilic or hydrophobic groups and can be repulsive or attractive or oscillatory. In the case of lipid bilayers, the water molecules bind strongly to hydrophilic surface groups and energy is needed to dehydrate these groups as the two surfaces approach each other. Empirically, the hydration repulsion between two hydrophilic surfaces appears to follow the equation:

$$F_h = Ke^{-2x_d/L} . \tag{4.13}$$

Of the different steric forces only the undulation force does not decay rapidly to zero beyond a certain distance roughly equal to the lengths of the lipid molecules [51]. Fluid membranes can be considered as elastic sheets which have an undulatory wave-like motion associated with the membrane's bending modulus, k_b. A repulsive force arises from the entropic confinement of their undulation waves as two membranes approach each other. The equation for the undulation force is:

$$F_{und} = \frac{(kT)^2}{16k_b x_d^3} . \tag{4.14}$$

Steric-hydration forces often dominate over DLVO forces at small separations, and are responsible for the lack of strong adhesion or aggregation of bilayers and vesicles composed of uncharged lipids such as lecithin and those posessing polyoxyethylene and sugar headgroups [51]. Given the spacing conditions in myelin, these forces are generally ignored under the assumption that their effect is small compared to the DLVO forces. The surface charge can be assessed by equating the two DLVO forces:

$$F_{es} = F_{vdw} ,$$

resulting in an expression for y_d from Eq. 4.9:

$$\cosh y_d = \frac{F_{vdw}}{2nkT} + 1\,, \tag{4.15}$$

which allows Eq. 4.10 to define y_0. From Eq. 4.11, y_d and y_0 specify the surface charge, σ. Fig. 4-4 shows the surface charge as a function of x_d for the parameter values given in Table 4.2.

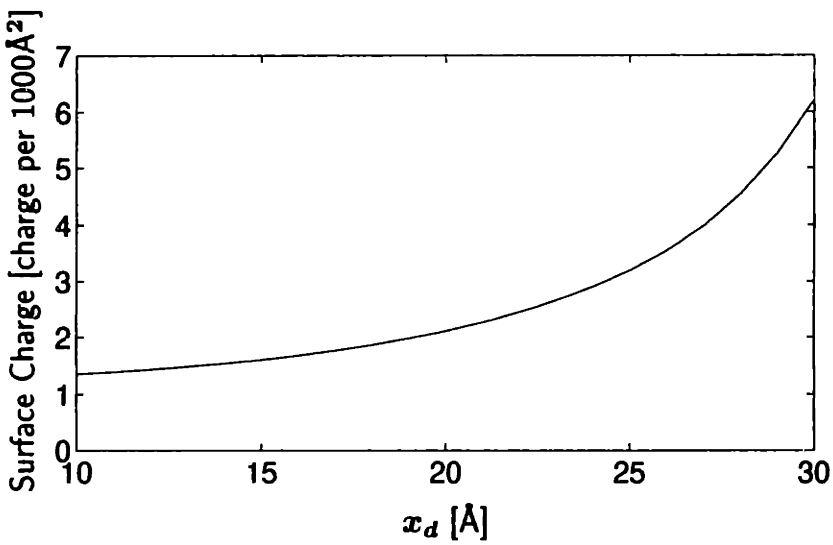

Figure 4-4: Surface charge calculated from equating Van der Waals and Electrostatic forces; $d_{ex} = 120$Å.

4.4.2 Diffusion in Myelin

Pulsed gradient spin-echo (PGSE) NMR diffusion measurements can be used to find the average distance travelled by water molecules. When spins diffuse within a regular lattice, the attenuation of the NMR signal as a function of the gradient strength reveals information about the lattice structure.

For myelin the spacing between the membrane layers might be directly observed with a very strong magnetic field gradient. For a period of $d \simeq 170$Å, and if the gradient duration should be no more than 5 ms to fall within the narrow pulse approximation, this would require an immense gradient strength of approximately 23,000 G/cm.

Instead we can focus on the apparent diffusion coefficient in the myelin. When the period increases, the apparent diffusion will also increase if we assume that the major impediment to diffusion is the presence of membranes. This means that a spin traversing the same number of membranes, will travel further if the distance between the membranes is greater. If n is the average number of membranes traversed in time Δ, then:

$$n\frac{d}{4} = \sqrt{2D\Delta}\,, \tag{4.16}$$

and the width of the diffusive envelope depends on d^{-2} if Δ is held constant.

A change in the surface charge of myelin could, theoretically, through the effect on the period, be observed by NMR, although in disease states other parameters can change too. The first steps would be to identify the component/s of the NMR signal associated with the intermyelinic water and then to measure the diffusion in this population of spins. The following chapter starts to discuss these issues.

Chapter 5

Correlation of NMR Diffusion and Transverse Relaxation with Structural Compartmentation in Frog Sciatic Nerve

5.1 Introduction

In this chapter the exchange between the populations characterized by different T_2 times in bullfrog peripheral nerve is quantified, and the water mobility and restriction in each population is assessed. The data acquired, combined with the known geometry of the nerve, is used to assign T_2 components to structural compartments.

5.1.1 T_2 and Compartmentation

The transverse relaxation decay curve in frog sciatic nerve *in vitro* was first decomposed by Vasilescu *et al.* (1977) [101]. The following values for T_2 of the nerves were found: 17±6 ms, 70±14 ms and 310±21 ms with relative proportional representation of 29%, 21% and 50%. These results were compared to the time-dependent D_2O fraction found in the nerve during H_2O-D_2O diffusion-mediated exchange, described

in a previous paper by some of the same authors [102]. In that study the inflow of D_2O could be fitted by a biexponential with 50% by weight of the water in a fast exchanging compartment, 21% in a slowly exchanging compartment, and 29% non-exchanging water. The almost exact correspondence between the relative populations in both experiments prescribed the structural assignments of the T_2 components: the short T_2 component was attributed to non-exchanging water closely associated with proteins and phospholipids, the intermediate T_2 component to axoplasmic water and the long T_2 component to extracellular water. A problem with this analysis is the association of a transverse relaxation as long as 17 ms with non-exchanging water. Similar values to those in Ref. [101] for the relaxation times in frog sciatic nerves *in vivo* were found later by Does and Snyder [30], namely 16±2 ms, 78±6 ms, and 317±18 ms, with populations of 16%, 48% and 36% respectively. The same authors also studied the T_2 spectrum of toad sciatic nerves *in vitro* and *in vivo* during the course of Wallerian degeneration [31]. They found that the disappearance of three well resolved T_2 components correlated with the loss of myelin after the injury.

Assignment of the short T_2 component to water associated with the myelin sheath has its roots in many papers. In 1984 Jolesz *et al.* found a lengthening of T_2 in rat sciatic nerves after Wallerian degeneration [55] and in 1987 these investigators compared the NMR relaxation in myelinated and non-myelinated nerves from a garfish [54]. The results suggested that the component with the shortest relaxation time may be water associated with the myelin membranes and that myelin limits the rate of exchange between the intraaxonal and extraaxonal compartments.

From comparison with compartmental volumes as shown in a microscopic cross-section, the three populations of spins contribuing to tri-exponential transverse decay curves in crayfish abdominal nerve cord were associated with structural compartments [69]. In this report, the intra-axonal space of the giant axons in the nerve trunk was hypointense compared to the region including much smaller axons, connective tissue and extracellular space on a T_2-weighted NMR microscopy image. The compartmental assignments were: intramyelinic water protons T_2=50±20 ms; intra-axonal water T_2=200±30 ms; extra-axonal water T_2=600±200 ms with respective

population fractions of 7±4%, 59±12% and 32±9%. The microscopy image supports the assignment of the longest T_2 component to a compartment other than the axonal cytoplasm. One potential problem with a comparison of NMR signal to compartmental volumes is the possible existence of a certain amount of non-exchanging water (30% according to Ref. [102]) which may not contribute measurable signal.

In the squid giant axon which has a diameter of about 500μ, T_2 in the cytoplasm was measured to be 348 ± 36 msec [22]. The value was almost the same when the cytoplasm was removed and thus isolated from the surface membrane. This finding led to the conclusion that the observed shortening of T_2 compared to free water is unrelated to the bounding membrane and must be caused by interactions between water molecules and the fibrous protein matrix in the axoplasm. Schoeniger *et al.* (1994) found an average T_2 of 78 ms in the nucleus and 29 ms in the cytoplasm from imaging single isolated neurons from the sea hare Aplysia Californica [90].

In the white matter of the brain, one of the earliest studies which looked at continuous relaxation time distributions found three components with T_2's of 13.1 ± 1.1 ms, 89 ± 3 ms and 306 ± 59 ms in freshly excised cat brain [68]. The proportions were 7%, 86% and 3% respectively. The remaining 4% were attributed to extremely short T_2 times. Note that the pulse sequence requirements for imaging allow acquisition of many fewer points on the transverse relaxation decay curves which also have a much lower SNR. The assignment of the short T_2 to myelin-associated water has been used for imaging myelin in studies in which the proportion of the short T_2 component from a CPMG imaging sequence was shown to approximately follow the distribution of white matter [65, 108]. Short T_2 maps of the brains of multiple sclerosis patients have shown an overall reduction in this component in the lesions, and in the case of one patient showed the most reduction in lesions which were at least four years old.

In summary, evidence exists to support the assignment of different T_2 times in nervous tissue to different structural compartments but no data is available on the extent of exchange between compartments. The assignment of the short T_2 component in both the peripheral nervous system (PNS) and the central nervous system (CNS) to intra-myelinic water is supported by many observations and also by the

results from Chapter 4. Extracellular water is assumed to contain a lower concentration of macromolecules and thus have a longer characteristic transverse relaxation time. Transverse relaxation may, however, reflect only the influence of a very small number of binding sites, giving limited information about the rotational mobility of most of the water molecules in the tissue [36]. We shall see that the characteristics of the diffusion corresponding to the transverse relaxation times measured in nerves indicate that the longer T_2 time is associated with the intracellular space.

5.1.2 Diffusion in Neural Tissue

The use of diffusion to elucidate the structural dimensions of compartments too small to image was pioneered by Cory and Garroway (1990) [27]. Diffusion anisotropy has been frequently reported for biological tissue. A paper by Henkelman *et al.* (1994) provides a good summary of the orientational dependence of the NMR properties of a number of tissue samples on the direction of the static magnetic field, and on the applied magnetic field gradients in the case of diffusion [46]. This paper also demonstrates a deviation from linearity in the semi-log plot of the diffusion attenuation versus b in optic nerves oriented in the direction of the field gradient. The lack of any obvious physical restriction in the direction parallel to the fibers leads to the supposition that compartments with different diffusion coefficients exist within the tissue.

Beaulieu *et al.* (1994) found that the diffusion in the giant squid axon (diameter 0.2-1 mm) is nearly isotropic which rules out a significant contribution from the neurofilaments [11]. Studies by Anderson *et al.* (1996) showed that the apparent diffusion coefficient (ADC) in rat optic nerve increases when the extracellular volume increases and vice versa and that the changes are independent of membrane polarization and cellular energy metabolism [8].

The origin of the anisotropic diffusion in brain white matter was studied by Le Bihan *et al.* (1993) who determined that the ADC remains unchanged for diffusion times longer than 20 ms, which would seem to indicate that there is no true restriction on this timescale, although the maximal gradient used was only 3.5 G/cm [15].

Instead, a model of hindered diffusion with permeable barriers was postulated. Diffusion would be considered hindered due to the tortuosity of the diffusion paths around the axons. Another study of diffusion was undertaken in cat brain before and after occlusion of the middle cerebral artery to simulate stroke [72]. Here too no change was reported in the diffusion constant for longer diffusion times (>50ms) in both healthy and stroke-damaged tissue.

5.2 Methods

5.2.1 Sample preparation

One large bullfrog which had been kept at 4°C, was decapitated and pithed and both sciatic nerves dissected from the spinal cord till the knee. The nerves were cleaned of blood and fat under a dissecting microscope, but for longevity not desheathed. Each nerve was cut into two 4 cm long sections giving 4 samples. The ends were tied with silk thread, placed in frog Ringer's solution [50], and while not undergoing measurement, stored at 4°C. For the NMR measurement, the samples were pulled into 2.2 ID NMR tube with Ringer's and the ends of the tube were sealed.

The experiments commenced 12 hours after dissection and lasted 4 hours for each nerve sample. The first sample measured was measured again at the end of the sequence of experiments to see if time from dissection had any effect on the results. The sequence of acquisition for this sample was reversed as well to check dependence on time in the tube. Neither condition qualitatively affected the result. Bullfrog sciatic nerves with intact sheaths remain functional for a week after dissection if kept refrigerated which implies that the structure did not change very much during the time it took to perform all the measurements.

5.2.2 Hardware

The NMR equipment consisted of a vertical bore magnet at a field of 2.35 Tesla with the RF and gradient coils controlled by a Bruker console. The maximum gradient

strength was approximately 460 G/cm over a sample size of 2.2 mm. The duration of the π pulse was set to 3 μs. The gradients were calibrated on a water sample in which the diffusion constant was assumed to be 2.3 μ^2/ms at room temperature. Gradient mismatch was tested for by using the maximum gradients on a sample of cis Polybutadiene. Since the protons do not diffuse in this sample, no signal attenuation was expected or found after application of a pulsed gradient diffusion sequence.

5.2.3 Pulse Sequences

The two main pulse sequences are based on the Carr-Purcell-Meiboom-Gill (CPMG) sequence, preceded by either diffusion weighting or T_2 weighting. The details of the CPMG sequence are described in chapters 1 and 4. The raw data thus consists of transverse relaxation decay curves with 8192 points sampled 1 ms apart.

The sequence used to obtain a measure of the exchange between different T_2 components was proposed by Lee *et al.* (1993) and refered to as ARTDECO [63]. The sequence, shown in Fig. 5-1A, starts with a variable-length CPMG which reduces the transverse magnetization, followed by a $\pi/2$ pulse to store the remaining magnetization in the z direction. The spins are allowed to exchange during a mixing time of Γ = 100ms before a full length CPMG is acquired. The number of pulses in the first CPMG correspond to 74 different time durations approximately logarythmically spaced from 0 to 4095 ms, represented by t_1 in Fig. 5-1A.

The principle of this sequence bears some resemblance to exchange spectroscopy (EXSY) described in Ref. [53]. Exchange is similar to relaxation in that within certain limits of exchange magnitude, its effect on the spectrum is to broaden the peaks. Since in EXSY spectra are acquired, the observed resonance frequencies reflect the true resonance frequencies. In ARTDECO on the other hand, the measured relaxation times, which supposedly characterize the compartments, are perhaps not the true relaxation times of the system precisely because of exchange. So the exchange measured is between the apparent T_2 components, not between the true T_2 components.

The second pulse sequence quantifies the diffusion according to T_2 with a pulsed gradient stimulated echo (PGSTE) immediately followed by a CPMG sequence as

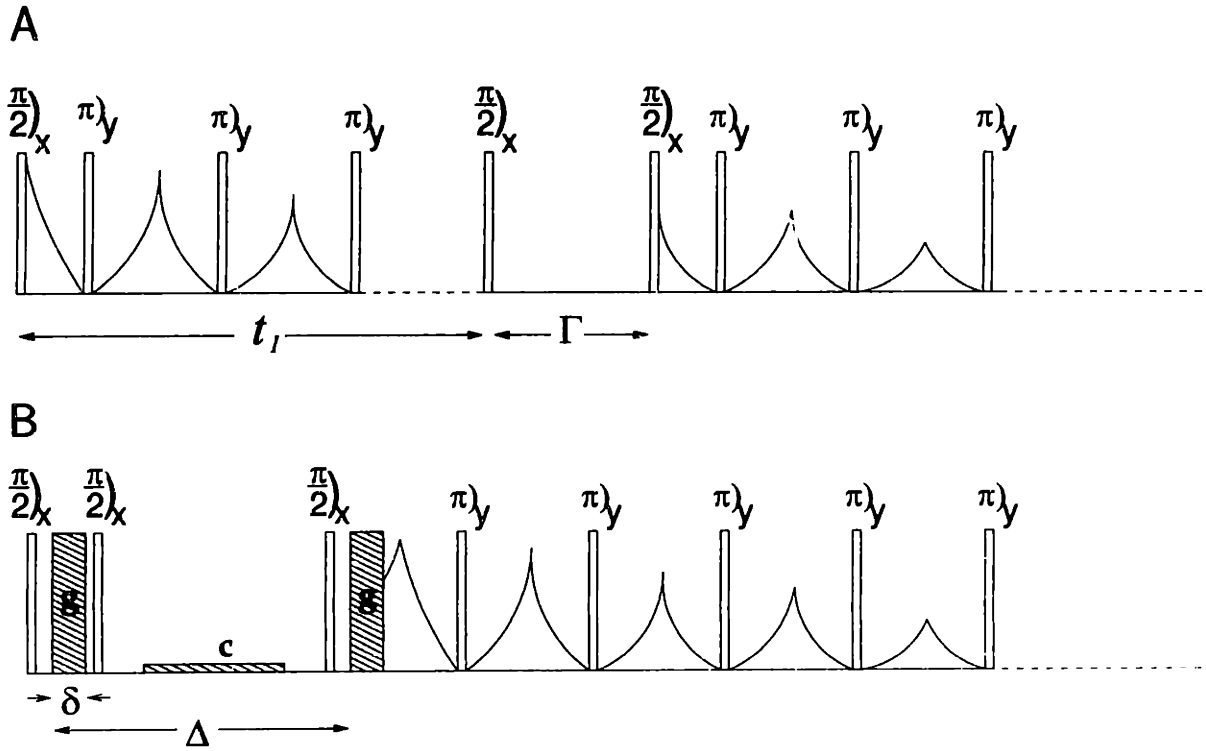

Figure 5-1: Pulse Sequences: (A) ARTDECO - the dashed lines indicate a varying number of π pulses in the first interval and continuation of the sequence for a total of 8192 π pulses in the second interval. (B) PGSTE-CPMG - the dashed lines indicate 8192 pulses; pulsed gradients are indicated by "g"; low "crusher" gradient indicated by "c".

shown in Fig. 5-1B. This type of sequence was also recently suggested by Laicher *et al.* and tested in rat lung [60]. We look only at cross-sectional diffusion, because of technical constraints and the lack of compartmentalization in the longitudinal direction, although longitudinal diffusion could give information about diffusion coefficients in non-restricted settings.

The PGSTE-CPMG data were acquired for four different diffusing times, Δ, to evaluate restriction, specifically: Δ = 6.1, 10.8, 30.55 and 100.4 ms. A crusher gradient ensured complete dephasing of transverse signal during the diffusing delay, Δ. The pulsed gradient duration, δ, in the PGSTE-CPMG sequence was chosen so as to give approximately the same maximum b-factor of $\sim 20\,\mathrm{ms}/\mu^2$ for each of the values of Δ, and was in all cases less than 2 ms. Data were collected for 30 b-factors for each diffusing time by stepping the gradient. Both sequences include phase cycling with 2 averages to eliminate baseline and reduce T_1 effects during the mixing time.

Specifically, the second and third 90° pulses in the sequences are phase shifted 180° relative to the first pulse on the 2nd acquisition.

For one sample, longitudinal and transverse relaxation were correlated using a saturation recovery sequence followed by a CPMG. We used saturation recovery here to prevent any negative contributions to the decay curve and to save time. Data from 42 time delays, logarythmically spaced between 2 ms and 20.5 s, were collected. English *et al.* (1991) used a similar principle with inversion recovery, subtracting from a baseline CPMG to fulfill the non-negativity requirement for NNLS [35].

5.2.4 Data Analysis

The CPMG curves obtained in all the experiments were initially fitted using the Non-Negative Least Squares algorithm to 286 logarythmically spaced relaxation time points (see Chapter 4 for more details). The average NNLS-fitted T_2 values for a sample were chosen from the peaks created by adding all the relaxograms of the sample, thus reducing the sensitivity to individual aberrations. This naturally gave more weight to the earlier measurements which had higher signal. The decay curves from each specimen were then force-fitted to multiexponential functions in which the average T_2 values found for that specimen served as the fixed characteristic decay times. Information about the diffusion, exchange and T_1 of the population of spins whose T_2 was given by each of the averaged T_2 values was provided by the amplitudes of the forced fit. Our analysis method differs from that in Ref. [63] in that we do not use a 2D Laplace transform. Here we rely on the fact that the apparent relaxation rates do not depend on the initial conditions and thus should be constant irrespective of any spin manipulation before the CPMG.

5.3 Results

Fig. 5-2A shows all the relaxograms for one of the samples. The sum of relaxograms in Fig. 5-2A is shown in Fig. 5-2B. The Roman numerals II to IV designate the values of T_2 around which most of the measurable spin populations in the nerve appear to

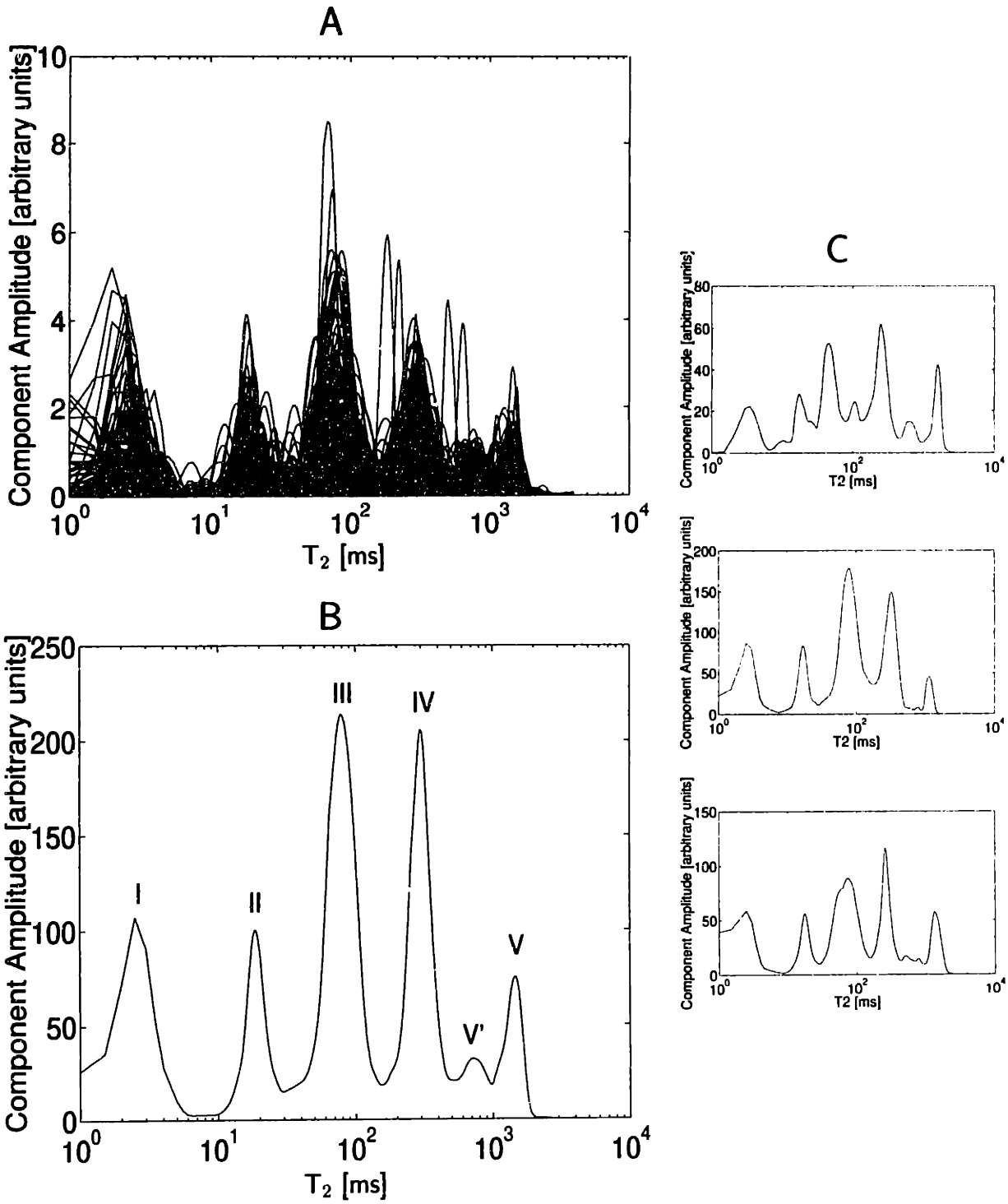

Figure 5-2: NNLS decomposition of transverse relaxation decay curves for all nerve specimens. (A) All the NNLS decompositions for one nerve sample; (B) Sum of curves in (A); (C) Results for other specimens.

concentrate. The existence or location of peak I cannot be accurately determined because the sampling rate in the CPMG is not high enough. Peak V corresponds to the buffer solution. Peak V' does not appear in all the samples and according to its corresponding T_1 time (see below) also originates in the buffer solution. Figure 5-2C shows the results from the other 3 nerve samples and Table 5.1 summarizes the average tissue T_2 values obtained. All further discussion of the results alludes to the population fractions found from the forced fit of the decay curves to the characteristic T_2 values as described in the previous section.

	II		III		IV	
sample #	T_2 [ms]	[%]	T_2 [ms]	[%]	T_2 [ms]	[%]
1	17	12	45	54	250	34
2	19	20	78	50	300	30
3	17	16	78	57	320	27
4	17	21	70	53	255	26

Table 5.1: Tissue T_2 values after forced fit, and relative populations for all samples.

Fig. 5-3 shows the measured points and the fitted curves for the saturation recovery T_1 measurement. The three nerve components are labeled as in Fig. 5-2B. The fitted T_1 values are listed in Table 5.2. The data from the short T_2 component (II) was best fitted by two T_1 values. The component labeled V' in Fig. 5-2, had the same T_1 as the component labeled V corresponding to the bathing solution, so it too was assumed to originate therein.

Peak Label	T_1 [ms]
II	424 (30%) and 1430 (70%)
III	1310
IV	1730
V'	3030
V	3150

Table 5.2: T_1 values from one measurement.

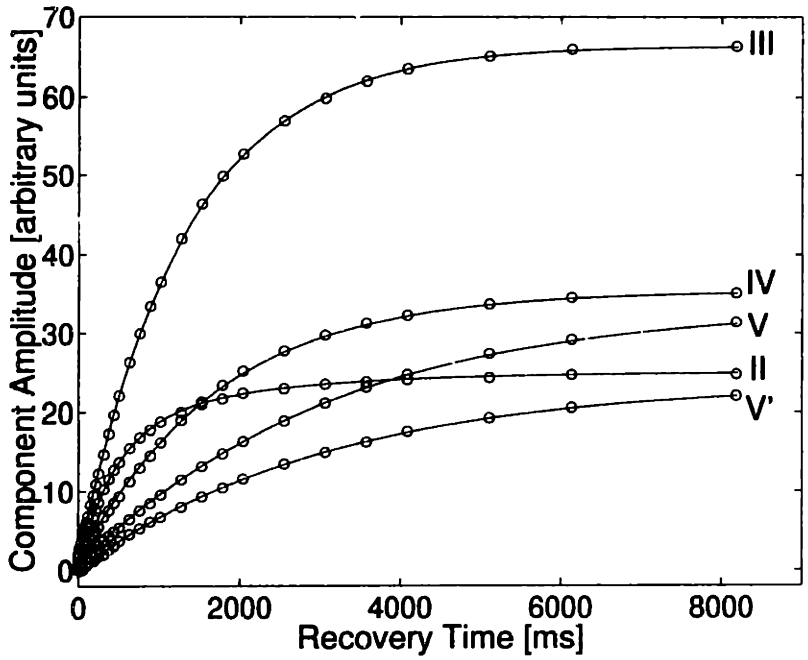

Figure 5-3: Longitudinal relaxation of different T_2 components from a saturation recovery experiment.

5.3.1 Exchange between T_2 Components

Once the original CPMG curves had been fitted to the characteristic T_2 times of the sample, new decay curves were obtained from the amplitudes corresponding to each one of the T_2 times with the time axis given by t_1 - see Fig. 5-1A. These were in turn fitted to the average T_2 values. Let us designate the amplitude of component T_{2i} in the fit of the data from component T_{2j} by P_{ij}. P_{ij} is proportional to the number of spins with an initial T_2 time of T_{2i} which transferred during the experiment to be measured with the spins contributing to the component with T_2 time T_{2j}.

The results for P_{ij} from the ARTDECO experiment are shown schematically in Fig. 5-4. Each sample is represented by one graph. The columns give the initial T_2 "affiliation" of the spin and the rows give the final T_2. The shading in Fig. 5-4 is proportional to the number of spins measured in the T_2 component corresponding to its row which originated in the T_2 component corresponding to its column. If there were no exchange between the components, only the diagonals would be shaded. Some exchange is apparent during the 100 ms mixing time, mostly between the shortest

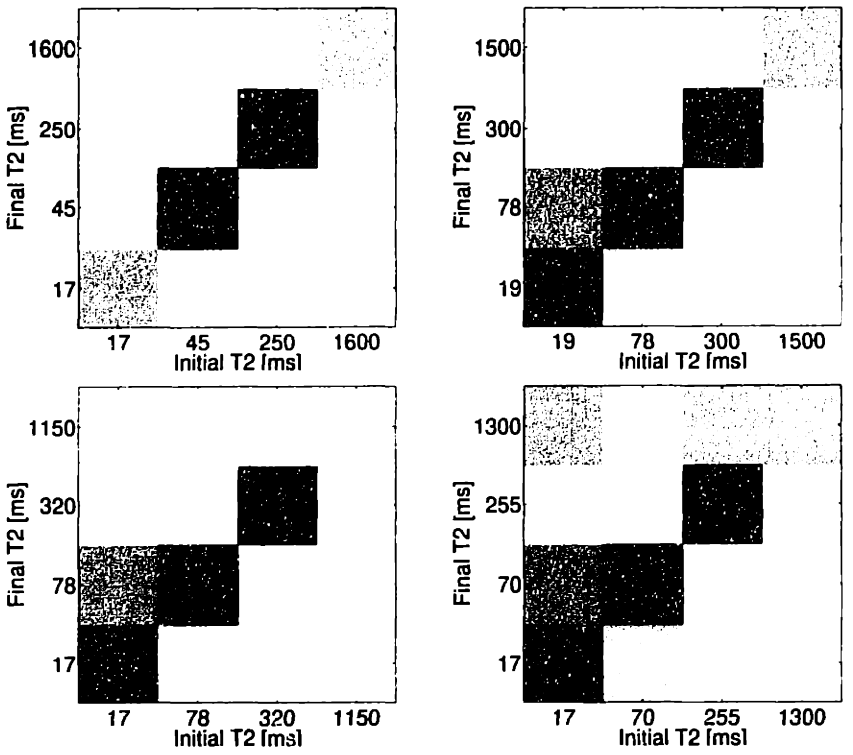

Figure 5-4: ARTDECO results shown schematically for the four nerve samples. The shading is proportional to the number of spins exchanging. Non-exchanging populations are represented in the diagonals.

and intermediate tissue components.

The exchange rates, k_{ij}, can be calculated from the data by approximating the reduction in component i due to spins transferring to component j as an exponential process in the following manner:

$$P_{i0} - P_{ij}(t) = P_{i0}e^{-k_{ij}t}, \tag{5.1}$$

where P_{i0} is proportional to the total population of component i,

$$P_{i0} = \sum_j P_{ji}. \tag{5.2}$$

Substituting a mixing time $t = \Gamma$ in Eq. 5.1 gives the solution for the exchange

rates k_{ij}:

$$k_{ij} = -\frac{\log(1 - P_{ij}/P_{i0})}{\Gamma} \tag{5.3}$$

The exchange times ($\tau_{ij} = 1/k_{ij}$) calculated in this manner are listed for all samples in Table 5.3.

	Exchange Times [ms]					
sample #	$\tau_{II\to III}$	$\tau_{III\to II}$	$\tau_{II\to IV}$	$\tau_{IV\to II}$	$\tau_{III\to IV}$	$\tau_{IV\to III}$
1	194	∞	477	∞	1,700	1,670
2	177	2,100	943	1,700	∞	∞
3	124	2,450	710	∞	2,890	864
4	156	996	∞	2,560	∞	∞

Table 5.3: Exchange times between tissue T_2 components for all samples. When no exchange was detected on the timescale of 100 ms the exchange time is designated by ∞.

Substitution of the apparent exchange rates and the apparent relaxation rates and proportions in the finite difference solution for the 3-site exchange equations results in <3% change in the populations of the intermediate and long T_2 components (III and IV) and <14% change in the population of the short T_2 component (II). This argument is used to justify the statement that exchange does not significantly affect the relative proportions corresponding to the different T_2 times in the transverse relaxation decay curve.

5.3.2 Diffusion according to T_2 Components

Figure 5-5 shows the diffusion attenuation curves for one of the samples. The curves corresponding to the shortest mixing time ($\Delta \sim 5$ms) for all the T_2 components show an unphysical tail which may be an artefact of the gradients which are very strong in this case. Each T_2 component has a strikingly individual diffusion signature. The results are qualitatively the same for all four nerve samples.

The longest relaxation component (V with $T_2 \sim 1{,}500$ ms) indeed appears to correspond to the buffer since the fitted diffusion constants are high. The diffusion from this component does decrease with increasing Δ though, from 2.6 to 1.8 μ^2/ms. The data from the intermediate T_2 component of the CPMG (III with $T_2 \sim 78$ ms)

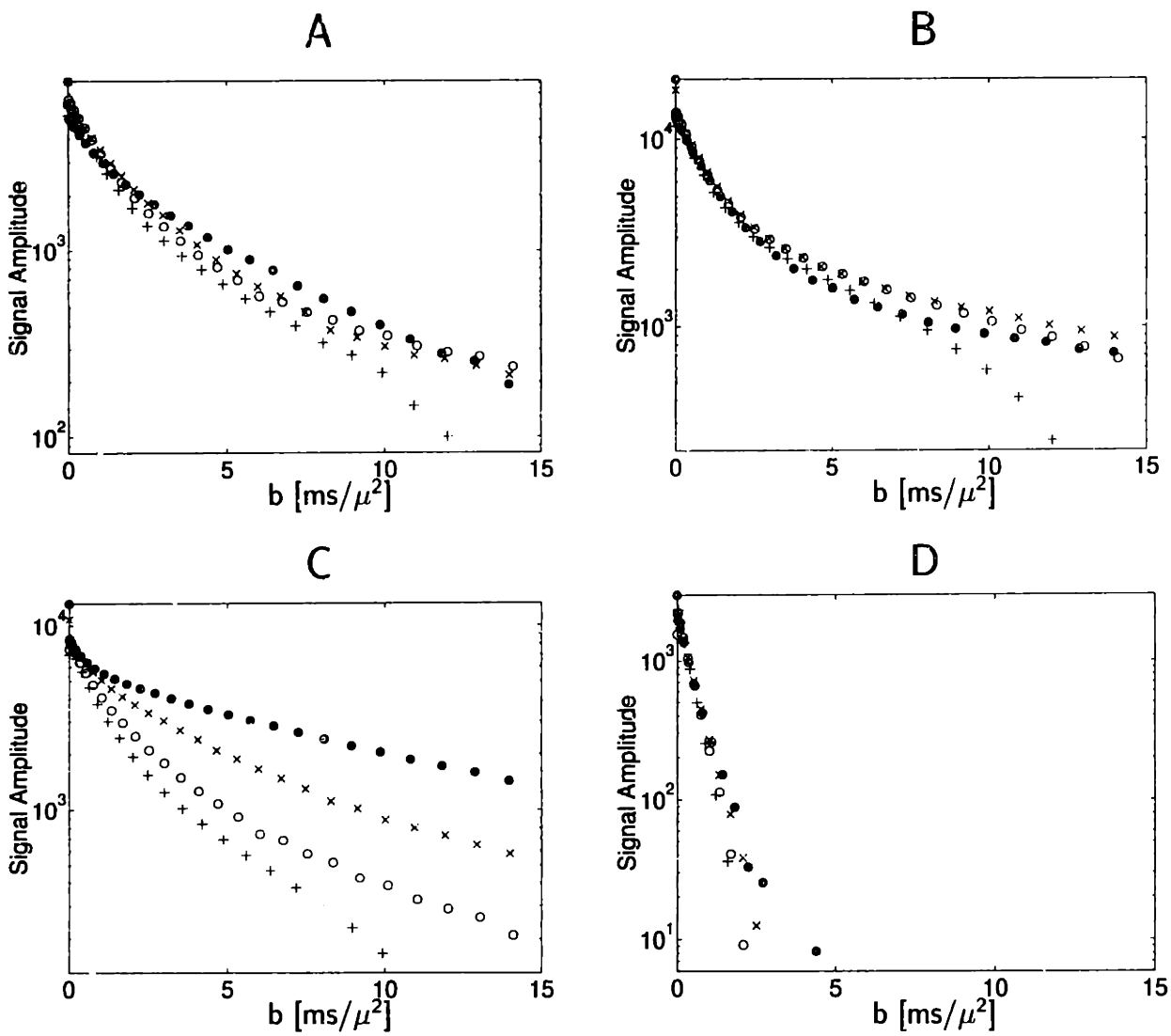

Figure 5-5: Diffusion attenuation from T_2 components of the NMR signal from nerve. Key: $\bullet \mapsto \Delta \sim 100$ ms; $\times \mapsto \Delta \sim 30$ ms; $\circ \mapsto \Delta \sim 10$ ms; $+ \mapsto \Delta \sim 5$ ms. (A) Component II, T_2=19 ms; (B) Component III, T_2=78 ms; (C) Component IV, T_2=300 ms; (D) Component V, T_2=1,500 ms.

exhibits no significant restriction over the timescales measured. This data can be fitted very well by the biexponential function: $E = 0.8e^{-0.95b} + 0.2e^{-0.1b}$. A biexponential analysis would imply that 40% (0.8×50% - see Table 5.1) of the NMR-visible water in the nerve is diffusing in an unrestricted manner on the timescale of 100 ms at quite a fast rate. The 1D mean displacement in 100 ms with D=0.95 μ^2/ms is $\sim 14\mu$. The lack of significant dependence of the diffusion attenuation curves on the diffusing time, Δ, means that the data cannot be fitted by a model in which diffusion is in

any way restricted. This implies that either the signal from this T_2 component is not from the intra-axonal space, or if it is, that there is no effective compartmentation in the nerve. Our data support the former argument.

The long T_2 component (IV with $T_2 \sim 300$ ms) is the most restricted. None of the curves describing the diffusion attenuation corresponding to T_2 times in nerves can be fitted by monoexponential functions. The non-exponential diffusion attenuation could be due to multiple water fractions possessing similar T_2s. Alternatively, the geometry of the underlying structure may prescribe the shape of the diffusion attenuation curve.

5.4 Discussion

Insofar as MRI can be used as a diagnostic tool to discover tissue abnormalities, an understanding of the origin of the contributions to the NMR parameters in normal tissue is important. Recently, a number of attempts have been made to define the relation between local and spatial mobility by correlating diffusion and T_2 in biological samples [59, 60, 100]. In all cases no more than two water fractions were assumed to exist in the sample. Knauss *et al.* (1996) [59] found that the local mobility of particles does not necessarily correspond to their spatial mobility in two water fractions in hydrated collagen II. The diffusion was measured using a pulsed gradient stimulated echo sequence which was preceded by a Hahn spin echo. The spin echo time was varied to produce diffusion attenuation curves with different T_2 weighting. The contribution of the fast diffusing water to the signal decreased with increasing time of T_2 relaxation. It was concluded that the rotationally "free" water is confined to channels formed by the holes between collagen molecules and is thus spatially restricted. In excised lung tissue, Laicher *et al.* (1996) [60], using a 13-interval stimulated echo sequence followed by a CPMG, qualitatively matched the appearance of more rapid decay in the CPMG with the application of stronger diffusion gradients. Van Dusschoten *et al.* (1996) [100] proposed a pulse sequence consisting of a CPMG imaging sequence incorporating pulsed field gradients around the first inversion pulse. The T_2 information from the CPMG was used to define two populations of spins in

order to fit to each one a diffusion constant. The sequence was applied with limited success to the differentiation of tissue and cerebrospinal fluid in cat brain.

Our aim has been to find out if components of the NMR signal in an amphibian peripheral nerve can be assigned to structural compartments in the nerve. The clear existence of multiple T_2 times indicates some type of compartmentation. According to our measurements, exchange exists between the compartments as manifested in the results from ARTDECO. Once exchange is quantified, the permeability constant of barriers can be determined according to Eq. 5.4:

$$k = \frac{1}{\tau} = \frac{PS}{V} \tag{5.4}$$

where P is the permeability coefficient, S is the surface area and V is the volume. Since the mixing time in our ARTDECO experiment was only 100 ms, any measured exchange between components probably indicates that the exchange time is less than 5s. Limits on the permeability of the whole myelin sheath for an average axon radius of 5μ can then be calculated from the exchange between components III and IV:

$$\begin{aligned} 860\,\text{ms} < \quad \tau \quad &< 5,000\,\text{ms}\,, \\ \Rightarrow \; 5 \times 10^{-5}\text{cm/s} < \quad P \quad &< 2.9 \times 10^{-4}\text{cm/s}\,. \end{aligned}$$

In our case, the exchange rates are relatively low so we have ignored the effect of exchange on the CPMG curve itself and have considered the rates to represent the exchange between the true T_2 components. When the water dynamics of a two-site exchange system are of interest as, for example, in red blood cells [75], a more rigorous analysis of the ARTDECO experiment may provide accurate permeability coefficients.

Based on the diffusion data corresponding to the different T_2 values, we make the following compartmental assignments: 1) the component with the intermediate T_2 shows relatively high and unrestricted diffusion on a timescale of 100 ms which can be compatible only with the extracellular space since otherwise compartmentation would

not be maintained; 2) the component with the longest T_2 appears to exhibit the most restricted diffusion and is thus assigned to the intracellular space. The cause of the faster relaxation in the extracellular space compared to the intra-axonal space may by the abundance of collagen I. Collagen is definitely a relaxing factor in tendon and studies have shown that tumors that are relatively acellular and have more collagen exhibit a shorter T_2 than tumors with an otherwise similar histological composition [94]. The assignment of the short T_2 component of the signal to the intramyelinic water follows from the data of many studies, including the measurement outlined in Chapter 4. In Chapter 6 models of diffusion are proposed for each compartment in the nerve.

Pulse sequences designed to image diffusion anisotropy in nervous tissue may benefit from a long echo time which would emphasize the tissue component exhibiting the most restricted diffusion. When the objective is to display fiber tracts, then not the total diffusion is important but the extent of anisotropy. In more technical terms, the difference between the eigenvectors of the diffusion tensor in each voxel determines the ability to create a map of oriented fibers. Future plans include application of the ARTDECO and PGSTE-CPMG sequences to CNS white matter *in vitro*, and application of the pulse sequence used in Chapter 7 with different echo times to check for restriction of water mobility in white matter *in vivo*. The data will be compared to that of Le Bihan *et al.* [15].

Acknowledgements for this chapter

Thanks to Yuan Cheng for the use of his RF and gradient coils and to both Yuan and Xiaowu Tang for their technical help.

Chapter 6

Models of Diffusion in Myelinated Neural Tissue

6.1 Introduction

New, robust methods for quantitative diffusion tensor imaging *in vivo* call for a better understanding of the connection between measured diffusion and microstructure [43, 84]. Various models exist for water diffusion in tissues [96, 61, 92]. Szafer *et al.* (1995) made a model consisting of a periodic array of boxes which was studied both analytically and numerically [96]. Stanisz *et al.* (1997) used prolate ellipsoids to describe the axons, and spheres to describe the glia, in a model of optic nerve. The diffusion data is fitted to a 9-parameter model. Latour *et al.* (1994) studied packed erythrocytes as their model system. None of these models take into account either the distribution of cell sizes in biological tissue or the added information provided by T_2 measurements.

In this chapter the experimental results from Chapter 5 are compared to models of diffusion in the nerve which are consistent with the underlying geometry and the variability in axonal size. We shall see presently that taking into account the distribution of fiber diameters in nervous tissue can greatly affect the shape of the diffusion attenuation curve. The histogram in Fig. 6-1 shows the volume percent of intra-axonal space represented by each size of fiber in a bullfrog sciatic nerve. The

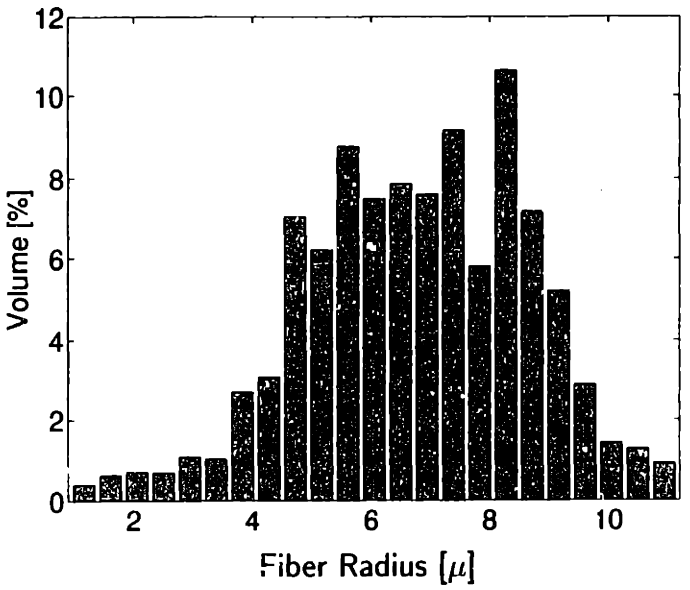

Figure 6-1: Volume percent of intracellular space plotted versus axonal radii in bullfrog sciatic nerve. Data from Ref. [109].

exact distribution of fiber diameters in the frog nerve, which will depend on the location of the cross section, is less important than the general range of dimensions. In the white matter of the brain the axons are in general smaller and more tightly packed but, as shown in the case of the corpus callosum in Ref. [1], they can also exhibit a wide range of sizes.

6.2 Diffusion Attenuation in Annular Cylindrical Geometry

The results from the ARTDECO experiment in Chapter 5 indicate that the exchange between the short T_2 component of the signal and both of the other components is low. Here we model the myelin membranes as a series of impermeable (on the timescale of milliseconds) concentric cylinders.

The general equation describing diffusion attenuation of the NMR signal (Eq. 1.20) is:

$$E(t,\vec{g}) = \iint \rho(\vec{r})P(\vec{r}|\vec{r}',t)e^{i\gamma\delta\vec{g}\cdot(\vec{r}'-\vec{r})}d\vec{r}'d\vec{r}. \tag{6.1}$$

The spatial displacement probability in an annulus of radius r is given by the gaussian function:

$$P(\theta|\theta',t) = \frac{1}{\sqrt{2\pi\sigma^2}} e^{-r^2(\theta'-\theta)^2/2\sigma^2}. \tag{6.2}$$

where σ^2 is the average squared displacement. The normalized spin density is:

$$\rho(\vec{r}) = \frac{1}{2\pi r}. \tag{6.3}$$

The diffusion attenuation in a ring of radius a after diffusion time Δ is then:

$$E(r=a,t=\Delta,\vec{g}) = \frac{1}{2\pi a\sqrt{2\pi\sigma^2}} \iint e^{-a^2(\theta'-\theta)^2/2\sigma^2} e^{i\gamma\delta\vec{g}\cdot(\vec{r}'-\vec{r})} d\vec{r}' d\vec{r}. \tag{6.4}$$

The standard deviation of the displacement is related to the diffusion constant by $\sigma = \sqrt{2D\Delta}$. Making the substitution $\psi = \theta' - \theta$ and adding limits to the integration:

$$E(a,\Delta,q) = \frac{1}{2\pi a\sqrt{4\pi D\Delta}} \int_{-\infty}^{\infty} e^{\frac{-a^2}{4D\Delta}\psi^2} \int_{-\pi}^{\pi} e^{iqa(\cos(\theta+\psi)-\cos\theta)} a^2 d\theta d\psi, \tag{6.5}$$

with $q = \gamma\delta g_x$ (assuming that the the gradient is in the x-direction). The integral over θ in Eq. 6.5 can be solved using the following expansion:

$$e^{ix\cos\alpha} = J_0(x) + 2\sum_{k=1}^{\infty} i^k J_k(x)\cos k\alpha \ . \tag{6.6}$$

After some simple math, the solution of Eq. 6.5 becomes:

$$E(a,\Delta,q) = J_0^2(qa) + 2\sum_{k=1}^{\infty} J_k^2(qa) e^{-\frac{k^2 D\Delta}{a^2}} \ . \tag{6.7}$$

The diffusion attenuation from Eq. 6.7 is plotted in Fig. 6-2 for an annulus of radius 5μ and the different diffusing times in our experiments, Δ. The diffusion constant used is 2.3 μ^2/ms.The two plots in Fig. 6-2 are based on the same simulated data but have different axes.

The only free parameters in the calculation so far are a, the annular radius, and the diffusion constant, D. Once we constrain the solution by summing over the axonal

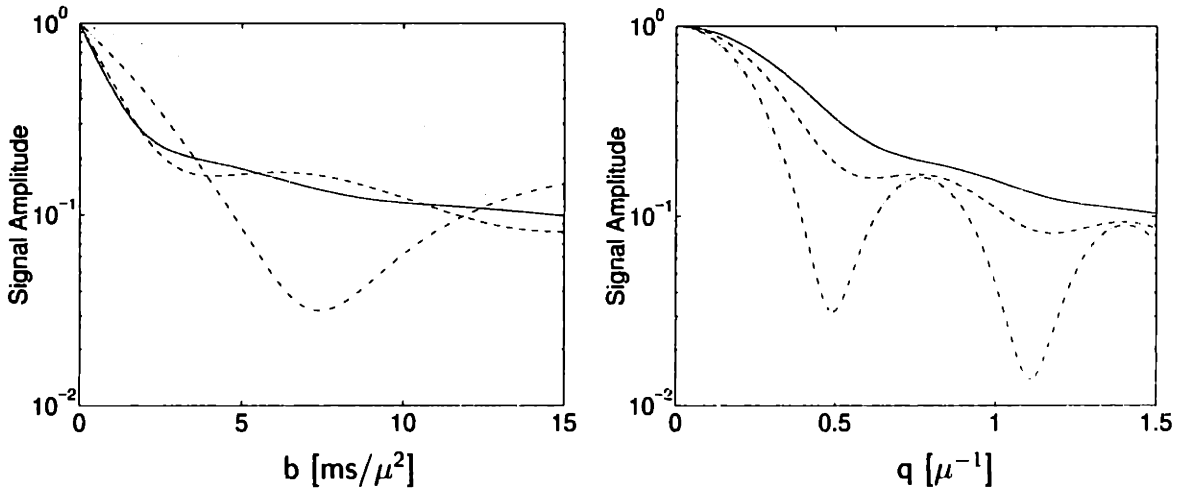

Figure 6-2: Theoretical diffusion in an annulus of radius 5μ for diffusing times Δ = 6.1 (—), 10.8 (– – –), 30.55 (·····) and 100.4 ms (·–·–·).

radii and relative populations from the histogram in Fig. 6-1, the only remaining free parameter is D. Figure 6-3 shows the curves obtained from summing these contributions assuming that the width of the myelin sheath extends from the axon radius to 4/3 times the axon radius. The diffusion constant used is again 2.3 μ^2/ms.

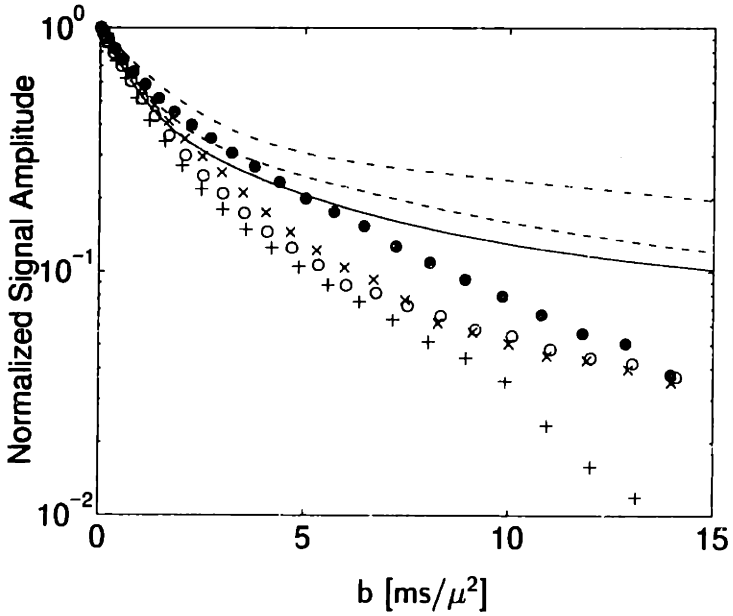

Figure 6-3: Diffusion attenuation from short T_2 component of the NMR signal from nerve compared to a model of diffusion in annular geometry. Curves calculated for the axonal distribution in Fig. 6-1 with D = 2.3 μ^2/ms are superimposed. Key: as in Figs. 5-5 and 6-2.

6.3 Tortuosity of Diffusion in the Extracellular Spaces

Tortuosity is generally defined as a factor which reduces the apparent diffusion due to the geometry of the path. The tortuosity coefficient, λ, is related to the increase in path length of a diffusing particle in a complex medium compared to that in a simple one. In the approximation of non-exchanging compartments, the water in between the axons has to deal with obstacles in the diffusion path. This effectively reduces the diffusion coefficient measured in any linear direction. We can write this as:

$$D_{app} = \frac{D}{\lambda^2}, \tag{6.8}$$

where D_{app} is the apparent diffusion coefficient. As an example, let us suppose that the increase in diffusion paths is equally distributed between all the possible values of $1/\lambda$, i.e. the diffusion attenuation would be:

$$E = \frac{1}{1/\alpha - 1} \int_1^{1/\alpha} e^{-bD/\lambda^2} d(\frac{1}{\lambda}). \tag{6.9}$$

This integral becomes:

$$E = \frac{\sqrt{\pi}[\mathrm{erf}(\sqrt{bD}/\alpha) - \mathrm{erf}(\sqrt{bD})]}{2\sqrt{bD}[1/\alpha - 1]}. \tag{6.10}$$

In principle, for diffusion in spaces between cylinders, the maximal value of λ can be $\pi/2$. It turns out that to approximate the data from the intermediate T_2 component with Eq. 6.10, we need to take a value of about 5 for α instead of $\pi/2$. The value used for the free diffusion constant, D, is 2.3 μ^2/ms. Figure 6-4 shows the data from the intermediate T_2 component, fitted by Eq. 6.10 (solid line) with $\alpha = 5$. The dotted line shows the curve described by Eq. 6.10 with $\alpha = \pi/2$.

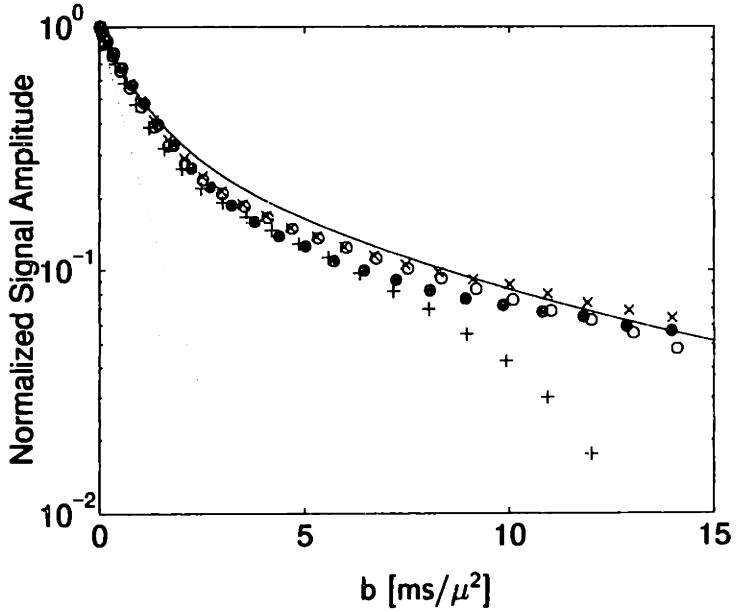

Figure 6-4: Diffusion attenuation from intermediate T_2 component of the NMR signal from nerve fitted to tortuosity model with $\alpha = 5$. The dashed line corresponds to $\alpha = \pi/2$. Key: as in Fig. 5-5.

6.4 Intracellular Restricted Diffusion

Here we model the intra-axonal spaces as cylinders and compare the corresponding diffusion attenuation curves with the data from Chapter 5. The solution for diffusion attenuation in cylindrical pores with reflecting boundaries has been calculated by Callaghan in Ref. [19]:

$$\begin{aligned} E(a,\Delta,q) &= \sum_k 4e^{-\beta_{0k}^2 D\Delta/a^2}\left[\frac{qaJ_0'(qa)}{(qa)^2-\beta_{0k}^2}\right]^2 + \\ &+ \sum_{nk} 8e^{-\beta_{nk}^2 D\Delta/a^2}\frac{\beta_{nk}^2}{\beta_{nk}^2-n^2}\left[\frac{qaJ_n'(qa)}{(qa)^2-\beta_{nk}^2}\right]^2 \end{aligned} \tag{6.11}$$

with β_{nk} defined by:

$$\beta_{nk}J_n'(\beta_{nk}) = 0 \quad , \quad n = 0,1,2,\ldots \tag{6.12}$$

Figure 6-5 shows the diffusion attenuation curves based on Eq. 6.11 for a few different values of the diffusion time, Δ. The simulated cylinder radius is $a = 5\mu$.

Here, as in the case of annular geometry, when a distribution of cylinder radii is

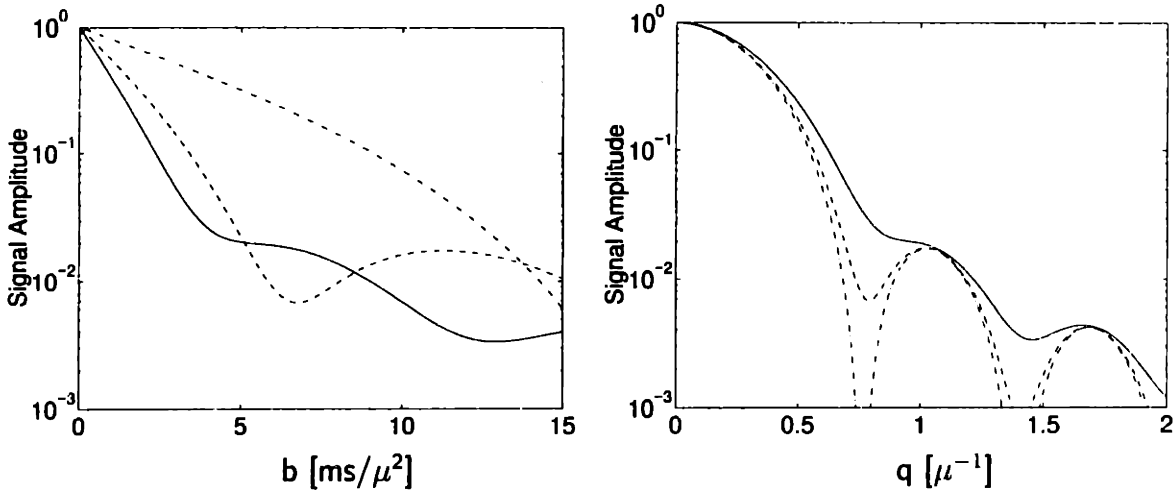

Figure 6-5: Theoretical diffusion attenuation in cylindrical pores of radius 5μ from Ref. [19]. Key: as in Fig. 6-2.

taken into account, such as exists in our simplified model of a peripheral nerve, the curves look "biexponential". Fig. 6-6 shows the data from the long T_2 component compared to the result of summing over cylinder radii. The value for the diffusion constant used here was $D = 1\ \mu^2/\text{ms}$.

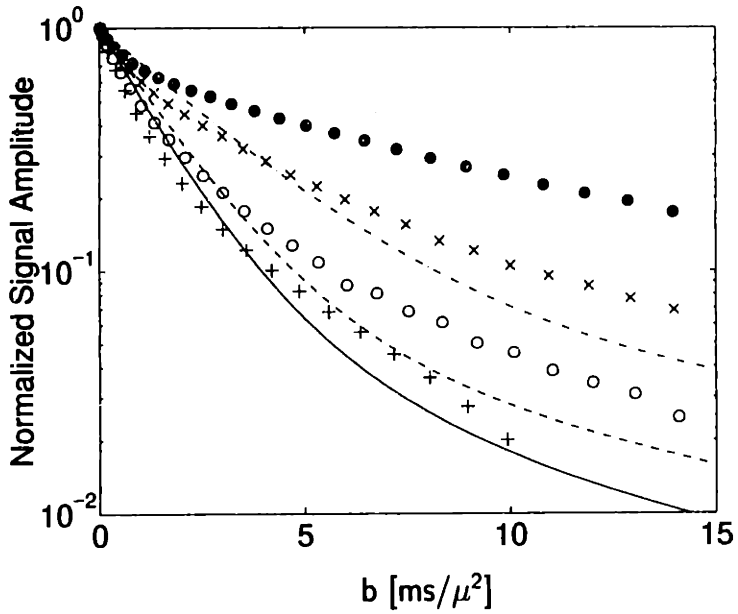

Figure 6-6: Diffusion attenuation from T_2=300 ms component of the NMR signal from nerve compared to model of differently sized cylindrical pores. Key: as in Figs. 5-5 and 6-2.

6.5 Summary

The two general cases in which the shape of a diffusion attenuation curve differs from a decaying monoexponential function are both associated with compartmentation. In the first case, diffusion is spatially restricted by barriers which may be partially permeable. The other case involves more than one population of diffusing spins that are in intermediate or slow exchange relative to the diffusing time in the experiment. The models presented here take the former approach and do not very well approximate the data from Chapter 5. Their value, however, lies in their simplicity and paucity of free parameters, and in their demonstration of the important contribution of pore size variability to the shape of the diffusion attenuation curve.

Chapter 7

Diffusion Tensor Imaging of White Matter[1]

7.1 Introduction

The demonstration of anisotropic diffusion in brain by magnetic resonance [74, 24, 9, 84] has opened a way to explore the structural anatomy of the white matter *in vivo*. Distinct bands of white matter fibers with parallel orientation may be distinguished from others running in different directions if MRI techniques are sensitized to water diffusion and the preferred direction of diffusion is determined.

Magnetic resonance diffusion imaging suffers from debilitating motion artefact unless steps are taken to ensure that all the acquisitions have the same phase or an adequate phase correction method is employed, for example, navigated echos. The most successful diffusion imaging sequences have been the ultrafast sequences, such as the diffusion-sensitized echo-planar imaging (EPI) technique [99], which acquire a complete image in one shot thus avoiding phase problems.

For this project we applied a modified version of the recently proposed Line Scan Diffusion Imaging (LSDI) technique [43]. Unlike EPI, LSDI exhibits minimal image

[1]S. Peled, H. Gudbjartsson, C-F. Westin, R. Kikinis and F. A. Jolesz. Magnetic resonance imaging shows orientation and asymmetry of white matter fiber tracts. *Brain Research*, in press, 1997.

distortion, does not require cardiac gating, head restraints or post-processing image correction, and can be implemented without specialized hardware on all standard MRI scanners. The linescan technique is relatively insensitive to bulk motion and physiologic pulsations of vascular origin due to the complete absence of phase encoding. The technique had not, however, been used for tensor imaging because of the inherently low SNR. After testing it turned out surprisingly, that for tensor imaging the results from this sequence surpass those of other sequences and this may be due to the long echo time (TE=121 ms) which emphasizes the components of the tissue with long T_2.

Scalar measures of anisotropy or geometry can easily be displayed in two dimensions but the display of tensors or vectors poses more of a problem. Previous display methods have depicted octahedra or ellipsoids in each pixel [87, 9], but this does not really allow for high spatial resolution. Limited success was achieved by using different intensities of the three colors red, green and blue to indicate the size of the apparent diffusion coefficient in each of the three cartesian directions [32, 76]. We developed a simple, intuitive solution to the problem using colors and lines. As a result we are able to present clear and detailed *in vivo* images of human white matter tracts. The orientation and distribution of most of the known major fiber tracts are demonstrated and clear evidence of hemispheric laterality in the anterior limb of the internal capsule is shown.

7.1.1 Methods

The gradient cycle in the LSDI interleaving scheme was modified to provide acquisition of more gradient directions and to allow elimination of the crusher gradients. Our data were acquired at the Brigham and Women's Hospital on a GE Signa 1.5 Tesla 5.4 system with standard 1 gauss/cm field gradients. The time required for acquisition of the diffusion tensor data for one slice was 3 min. By using 3/4 field of view with 95 columns. and by increasing the gradient duty cycle, it is possible to reduce the imaging time by 40%. Low slew rates were used on the diffusion gradients to minimize eddy current distortion. Imaging parameters were: effective TR=1.4 s, TE=121 ms,

δ=46 ms, Δ=56 ms (b_{high}=1 ms/μm^2, b_{low}=5x10^{-3} ms/μm^2), field of view 24 cm, effective voxel size 7.3×2.7×1.8 mm^3, 4 kHz readout bandwidth, acquisition matrix 127×128.

For each slice, 8 images are collected with different diffusion weightings and non-collinear gradient directions. If S_0 represents the signal intensity in the absence of a diffusion-sensitizing field gradient and S the signal intensity in the presence of gradient $\mathbf{G} = (G_x, G_y, G_z)$, the equation for the loss in signal intensity due to diffusion is given by the Stejskal-Tanner formula [93]:

$$\ln S = \ln S_0 - \gamma^2 \delta^2 (\Delta - \delta/3) \mathbf{G}\mathbf{D}\mathbf{G}^T, \tag{7.1}$$

where γ is the gyromagnetic ratio of ^{1}H, δ is the duration of the diffusion sensitizing gradient pulses and Δ is the time between the centers of the two gradient pulses. The eight images provide eight equations for S in each voxel which are solved in a least-squares sense for the 6+1 unknowns consisting of the six independent components of the symmetric diffusion tensor, $\mathbf{D}$, and $\ln S_0$. In the LSDI sequence, it is easy to show that cross terms between the slice select gradient for the 180° pulse and the diffusion sensitizing gradients account for less than 0.1% of the diffusion weighting, and have therefore been neglected here. Diffusion attenuation due to imaging gradients is already factored into S_0, as is T_2 weighting.

7.1.2 Geometrical Measures of Diffusion

In order to relate the measure of diffusion anisotropy to the structural geometry of the tissue a mathematical description of the diffusion tensors and their quantitation is necessary [9]. Any quantitative measure describing the diffusion should be invariant to rotation. Since $\mathbf{D}$ is symmetric it can be diagonalized and its eigenvalues calculated; all functions of the eigenvalues are rotation invariant. Let $\lambda_1 \geq \lambda_2 \geq \lambda_3 \geq 0$ be the eigenvalues of the diffusion tensor $\mathbf{D}$. The derivation of one set of useful and intuitive scalar measures based on the symmetry properties of the diffusion ellipsoid is described in the appendix [106]. The two most useful scalar measures for our

purposes are:

$$C_l = \frac{\lambda_1 - \lambda_2}{\lambda_1 + \lambda_2 + \lambda_3} \tag{7.2}$$

$$C_a = \frac{\lambda_1 + \lambda_2 - 2\lambda_3}{\lambda_1 + \lambda_2 + \lambda_3} . \tag{7.3}$$

These two measures, assigned from the tensor basis, describe the linearity and the anisotropy in each voxel. When applied to white matter, the linear measure, C_l, reflects the uniformity of tract direction within a voxel because it will be high only if the diffusion is restricted in two orthogonal directions. The anisotropy measure, C_a, indicates the relative restriction of the diffusion in the most restricted direction and will emphasize white matter tracts which within a voxel exhibit at least one direction of relatively restricted diffusion.

7.2 Anisotropy Display

Figures 7-1A and 7-1B show coronal images of the geometrical measures C_l and C_a. Major tracts, such as the corpus callosum and the posterior limb of the internal capsule, exhibit high linearity. Calculations show that in these areas $\lambda_1/\lambda_2 \approx 4$ and $\lambda_1/\lambda_3 \geq 10$.

Figure 7-1D shows a example of the detail and clarity of the acquired tensor images. We display the vector $C_a\hat{\mathbf{e}}_1$ on the background of the corresponding anatomical image ($\hat{\mathbf{e}}_1$ is the eigenvector corresponding to the largest eigenvalue). The blue headless arrows represent the in-plane components of $C_a\hat{\mathbf{e}}_1$. The out-of-plane components of $C_a\hat{\mathbf{e}}_1$ are shown in colors ranging from green through yellow to red, with red indicating the highest value for this component. Although choosing C_a as the weighting factor displays structure in all of the anisotropic areas, in the extreme case of planar diffusion in which $\lambda_1 \simeq \lambda_2 \gg \lambda_3$ the choice of $\hat{\mathbf{e}}_1$ over $\hat{\mathbf{e}}_2$ to represent the direction of the diffusion is arbitrary. Note also that there is ambiguity in the representation of diagonal fibers with both in-plane and out-of-plane components. Addressing this problem would very much complicate the two-dimensional display.

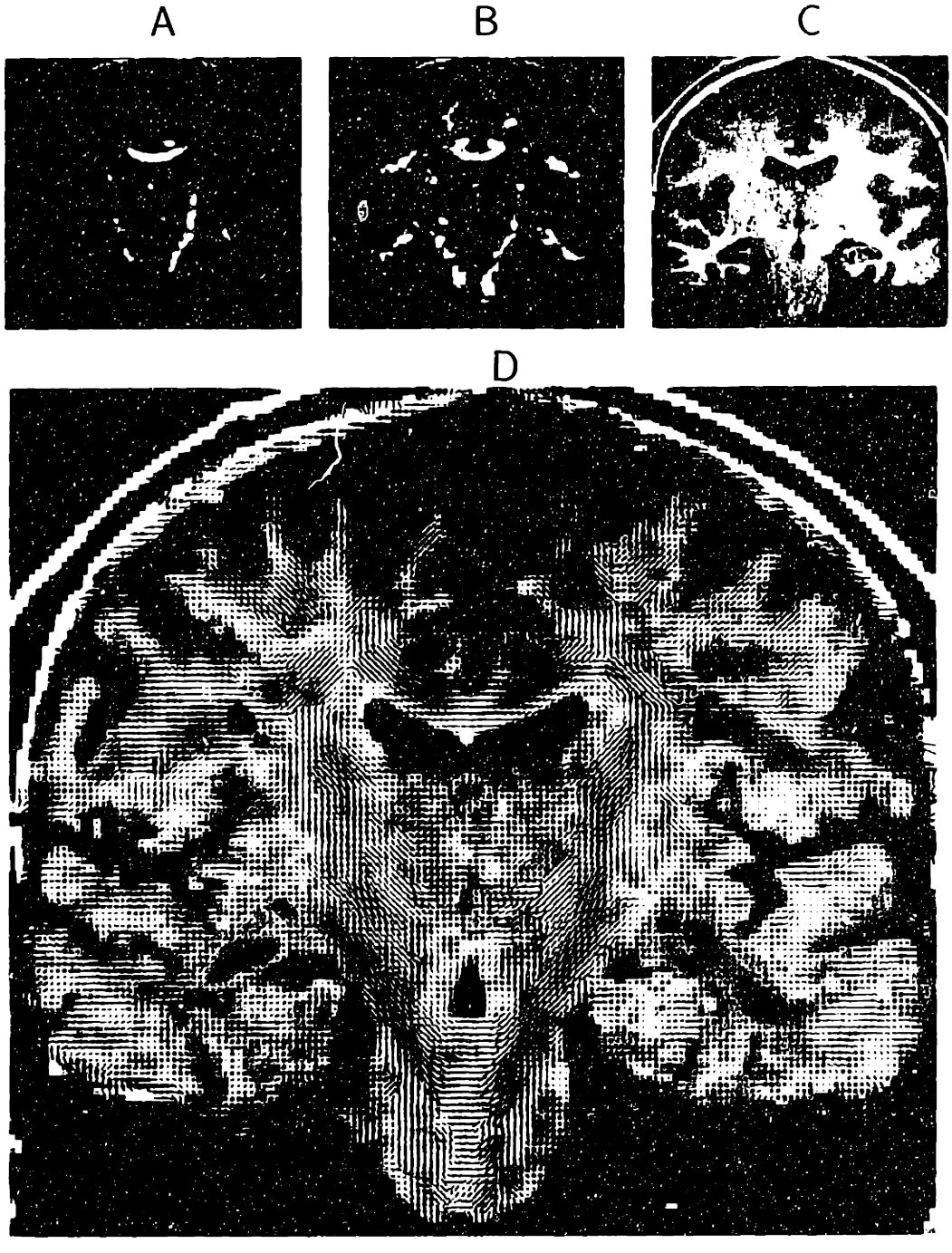

Figure 7-1: Coronal brain images of quantitative measures of diffusion and tensors. (A) Linear measure, C_l, scaled linearly such that 0=black and 0.5=white. (B) Anisotropic measure, C_a, (scaled 0.1 - 0.7) highlights all of the white matter tissue. (C) Corresponding anatomical magnetic resonance image for comparison. (D) Diffusion tensor display of the vector $C_a \hat{\mathbf{e}}_1$ on the background of the corresponding anatomical image.

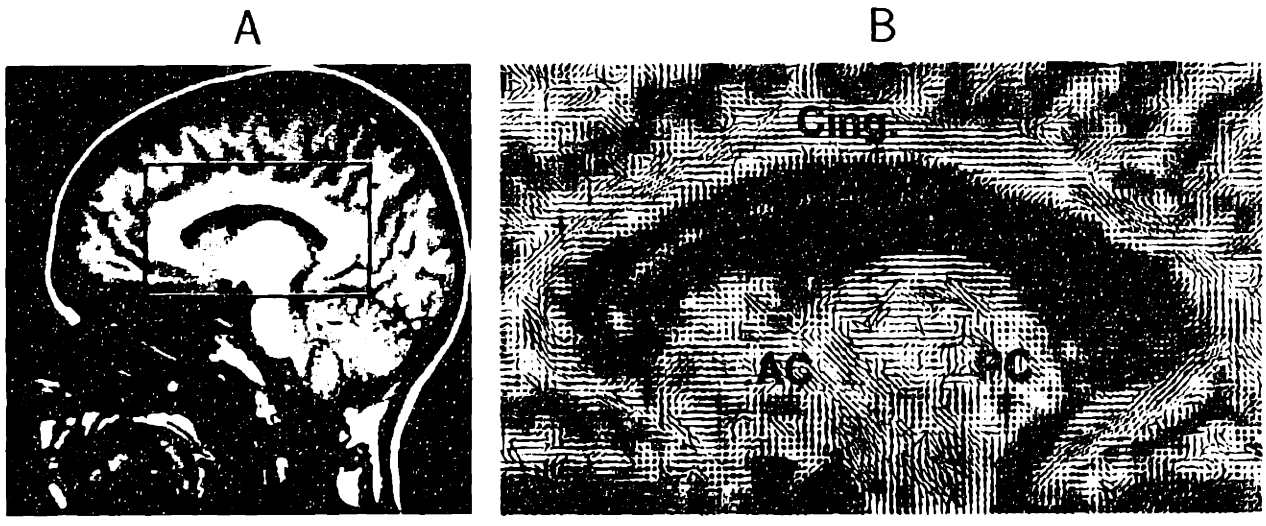

Figure 7-2: Sagittal diffusion tensor image with anatomical correlate. (A) Anatomical sagittal magnetic resonance image. (B) Diffusion tensor display of $\mathcal{C}_a \dot{\mathbf{e}}_1$ in the region indicated by the red box in (A). Red areas show perpendicular fiber tracts such as the corpus callosum (CC), and the anterior and posterior commissures (AC,PC). Blue lines above the corpus callosum represent the in-plane fibers of the cingulum (Cing.).

A closer look at anatomy is provided in figure 7-2B which shows the diffusion tensor map of the outlined region in figure 7-2A.

7.3 Hemispheric Asymmetry in White Matter

We applied the MRI technique, together with the mathematical description of the diffusion and the new display method, for the demonstration of major fiber tracts in the human brain using axial slices which include the corpus callosum, the internal capsule and the corticospinal tract. In addition we used the quantitative diffusion measures to investigate asymmetry in relation to sex and handedness. A comparison of anatomy between the right and left hemispheres of the brain derives its importance from the relationship between anatomical and functional asymmetry. Left hemispheric dominance for language skills is hypothesized to be associated with the average larger size of the left planum temporale found in 100 post-mortem adult brains [39]. Handedness has been found to affect hemispheric asymmetry, for example, in white right-handed individuals the anterior portion of the right hemisphere is generally wider and protrudes further anteriorly than the left, and the posterior

portion of the left hemisphere is commonly wider and protrudes further posteriorly than the right. Although numerous investigations report cortical asymmetry, very few relate to white matter [112, 37, 111, 64].

Diffusion tensor imaging was performed on 24 healthy volunteers between the ages of 18 and 44. Of the subjects, 8 were right-handed women (mean age = 29.5), 8 were right-handed men (mean age = 31.3) and 8 were non-right-handed men (mean age = 30.6). Handedness was verified with a standard questionnaire [78] resulting in a mean laterality quotient (LQ) of 0.82, 0.79 and ·0.58 for the respective groups. The LQ factor is defined to be in the range [-1,1] where a score of 1 indicates near inability of the subject to perform common everyday tasks with the left hand. Regions of interest within the major fiber tracts were selected to evaluate asymmetry and are shown in figure 7-3A. Relative asymmetry indices, defined by $\frac{R-L}{R+L}$, were calculated for each individual. R and L indicate the values of C_l in the right and in the left hemispheres for any particular anatomical structure. Three people independently chose anatomical regions of interest in 6 randomly chosen subjects giving an intraclass correlation coefficient of 0.91 from repeated-measures analysis of variance (ANOVA).

Large regional differences in the value of C_l, calculated for the average diffusion tensor in the regions of interest shown in figure 7-3A, are apparent in Table 7.1. C_l was calculated from the averaged apparent diffusion tensor in each region of interest. Note the high values of C_l in the corpus callosum and the posterior limb of the internal capsule versus the values in the mixed tracts of the frontal and occipital lobes. For this sample size, analyses of variance revealed no statistically significant dependence of the asymmetry indices on sex or handedness ($p > 0.01$). Two-tailed paired t tests of the asymmetry indices in the 8 regions revealed statistically significant asymmetry in the anterior limb of the internal capsule where C_l was higher in the right hemisphere than in the left ($p < 0.01$). The asymmetry is also directly visible in most of the individual tensor maps, as demonstrated in figure 7-3B.

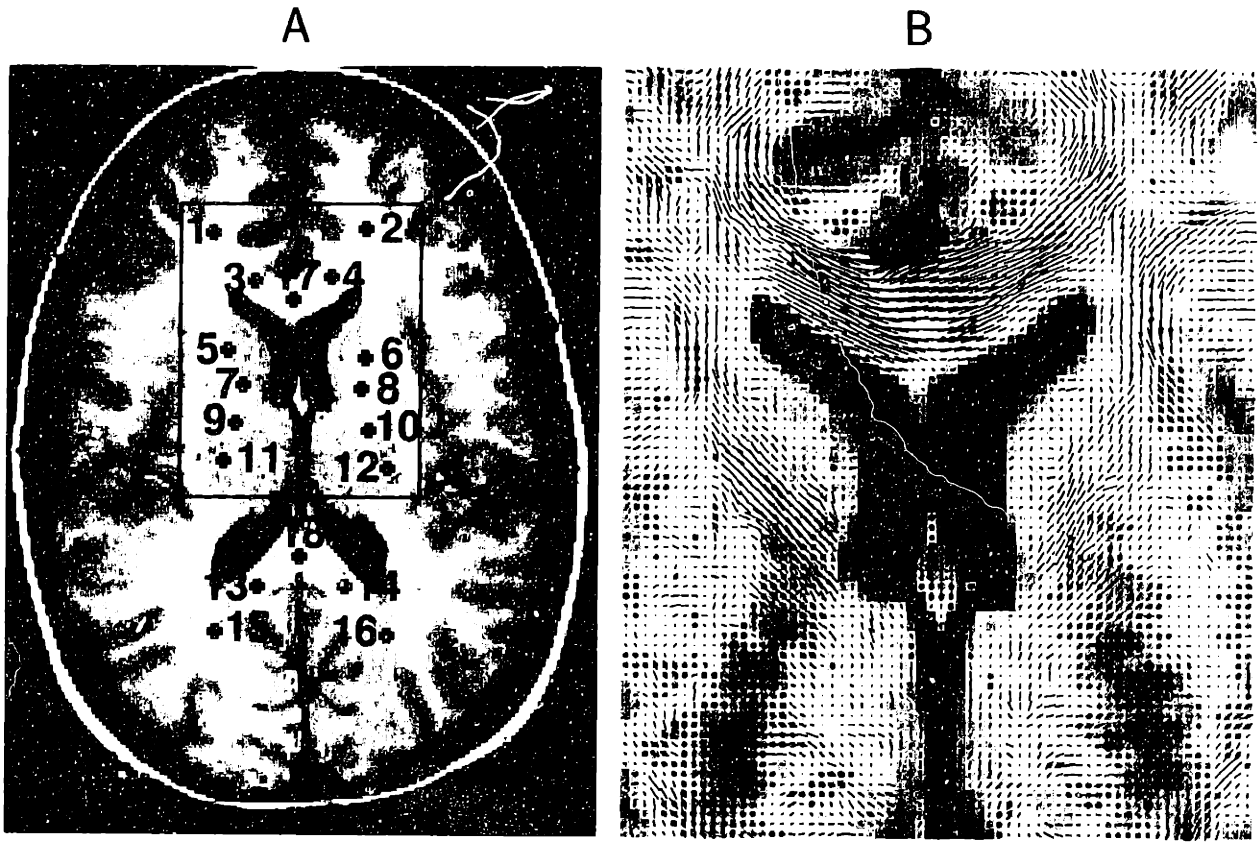

Figure 7-3: Laterality in white matter. (A) Regions of interest in the white matter. Each outlined region is 10.5 mm^2 in area (12 pixels). (B) Diffusion tensor display of $C_l\hat{\mathbf{e}}_1$ in the zoomed-in area indicated by the red box in (A). The fibers in the anterior limb of the internal capsule are more aligned in the right hemisphere (region no. 5 in (A)) than in the left hemisphere (region no. 6 in (A)). This is the anatomical location of the anterior thalamic peduncle.

7.4 Discussion

A low value for the measure of linearity, C_l, in a voxel within the white matter may indicate the existence of fibers crossing or fanning out from the direction of the main tract. Factors other than the directional similarity of fibers, that may affect the measure of diffusion linearity in a voxel are the average fiber diameter and the degree of myelination. Note that MRI methods always provide a macroscopic measure of a microscopic quantity which necessarily entails intravoxel averaging. Moreover, due to the multicompartmental nature of tissue, the apparent diffusion tensor will be time dependent even in the ideal case without macroscopic volume averaging. Thus the voxel dimensions and the imaging sequence timing parameters influence the measured diffusion tensor at any particular location in the brain.

#	Location	Right-Handed Females (n=8)	Right-Handed Males (n=8)	Left-Handed Males (n=8)
1	R. frontal	0.10±0.014	0.17±0.020	0.18±0.024
2	L. frontal	0.14±0.020	0.14±0.016	0.12±0.029
3	R. genu CC	0.47±0.031	0.43±0.022	0.46±0.028
4	L. genu CC	0.43±0.019	0.38±0.026	0.47±0.011
5	R. ant. IC	0.24±0.013	0.30±0.025	0.26±0.011
6	L. ant. IC	0.21±0.020	0.23±0.029	0.21±0.020
7	R. genu IC	0.34±0.019	0.34±0.013	0.35±0.020
8	L. genu IC	0.32±0.019	0.31±0.019	0.28±0.029
9	R. post. IC(1)	0.37±0.021	0.38±0.032	0.41±0.028
10	L. post. IC(1)	0.37±0.022	0.34±0.019	0.37±0.019
11	R. post. IC(2)	0.37±0.025	0.36±0.025	0.43±0.018
12	L. post. IC(2)	0.40±0.028	0.37±0.015	0.41±0.014
13	R. splen. CC	0.53±0.031	0.49±0.027	0.54±0.035
14	L. splen. CC	0.53±0.035	0.41±0.047	0.42±0.047
15	R. occipital	0.21±0.029	0.20±0.033	0.17±0.032
16	L. occipital	0.20±0.025	0.17±0.010	0.14±0.021
17	CC genu	0.50±0.036	0.51±0.043	0.52±0.037
18	CC splen.	0.58±0.022	0.63±0.022	0.59±0.038

Table 7.1: Mean values and standard errors of the mean of the measure of linearity, C_l, according to brain region. Abbreviations are: L=left; R=right; CC=corpus callosum; IC=internal capsule; ant.=anterior limb; post.=posterior limb; splen.=splenium.

This *in vivo* technique has several conceivable uses. Besides the possibility of studying the structure and geometry of white matter and the connectivity of the brain, diffusion tensor imaging and quantitation may have some utility in studying neural development and plasticity. It should also be possible to associate lesions in the white matter with particular fiber tracts for functional correlation.

Acknowledgements for this chapter

The work for this project was carried out with the collaboration of Hákon Gudbjartsson and Carl-Fredrik Westin [80]. The project was inspired and made possible by the development of the Line Scan Diffusion Imaging sequence by Gudbjartsson *et al.* [43]. We are grateful to Dr. Deepak Pandya and Dr. Marjorie LeMay for their contributions, and to all the volunteers for their time in the magnet.

Appendix A

A.1 Two-Site Exchange

Exchanging systems occupy a prominent position in many of the preceding chapters. The equations describing transverse relaxation for two populations M_A and M_B in a two-component system are described below [113].

$$\begin{aligned} \dot{M}_A &= -R_A M_A - k_A M_A + k_B M_B \,, \\ \dot{M}_B &= -R_B M_B - k_B M_B + k_A M_A \,. \end{aligned}$$

R_A and R_B are relaxation rates and $k_{A,B}$ are exchange rates between the components. If the initial conditions are $M_A(0) = P_A$ and $M_B(0) = P_B$, the solution for each component is given by:

$$\begin{aligned} M_A &= A_1 e^{-\mu_1 t} + A_2 e^{-\mu_2 t} \,, \\ M_B &= B_1 e^{-\mu_1 t} + B_2 e^{-\mu_2 t} \,, \end{aligned}$$

where

$$\mu_{1,2} = \frac{1}{2}(R_A + k_A + R_B + k_B \mp \sqrt{(R_B - R_A + k_B - k_A)^2 + 4k_A k_B}) \,, \qquad \text{(A.1)}$$

and

$$A_1 = \frac{(-R_A - k_A + \mu_2)P_A + k_B P_B}{\mu_2 - \mu_1} \quad , \qquad A_2 = P_A - A_1 \ ,$$
$$B_1 = \frac{(-R_B - k_B + \mu_2)P_B + k_A P_A}{\mu_2 - \mu_1} \quad , \qquad B_2 = P_B - B_1 \ .$$

Often the only detectable signal is a superposition of the two components, i.e., one biexponential curve. The amplitudes of each exponential term are given by:

$$\begin{aligned} M_1 &= A_1 + B_1 = \frac{(-R_A + \mu_2)P_A + (-R_B + \mu_2)P_B}{\mu_2 - \mu_1} \ , \\ M_2 &= A_2 + B_2 = \frac{(R_A - \mu_1)P_A + (R_B - \mu_1)P_B}{\mu_2 - \mu_1} \ . \end{aligned} \tag{A.2}$$

Detailed balance at equilibrium implies that $P_A k_A = P_B k_B$ which will constrain the solution. Under conditions of fast exchange, i.e. $k_A \gg R_A$ and $k_B \gg R_B$, the signal will decay as a monoexponential with a rate λ equal to the weighted average of the true decay rates [113]:

$$\lambda = P_A R_A + P_B R_B \ . \tag{A.3}$$

Equations A.1 and A.3 also describe two-compartment diffusion if $q^2 D_{A,B}$ are substituted for $R_{A,B}$ and the time dependence is determined by the diffusing time, Δ [56]:

$$E_\Delta(q) = E_1 e^{-\nu_1 \Delta} + E_2 e^{-\nu_2 \Delta} \ ,$$

with,

$$\nu_{1,2} = \frac{1}{2}(q^2 D_A + k_A + q^2 D_B + k_B \mp \sqrt{(q^2 D_B - q^2 D_A + k_B - k_A)^2 + 4 k_A k_B})$$

and

$$\begin{aligned} E_1 &= \frac{(-q^2 D_A + \nu_2)P_A + (-q^2 D_B + \nu_2)P_B}{\nu_2 - \nu_1} \\ E_2 &= \frac{(q^2 D_A - \nu_1)P_A + (q^2 D_B - \nu_1)P_B}{\nu_2 - \nu_1} \ . \end{aligned}$$

If the motion of the spins is not restricted i.e. the apparent diffusion constants do not change with Δ, then this is a biexponential in Δ. This is a bi-exponential function in $b = q^2\Delta$ only if the exchange rates are negligible.

A.2 Short Time Averaging for Increased SNR

Let θ be the flip angle of the RF pulses and the initial longitudinal magnetization be given by M_0; then after the first pulse, the remaining magnetization will be $M_0 \cos\theta$ and the measured magnitude of the signal will be $S_1 = M_0 \sin\theta$. During the time between pulses, τ, the magnetization will recover to the extent:

$$M(\tau) = M_0 \cos\theta e^{-\tau/T_1} + M_0(1 - e^{-\tau/T_1}).$$

The signal from the second pulse will then be:

$$S_2 = \left[M_0 \cos\theta e^{-\tau/T_1} + M_0(1 - e^{-\tau/T_1})\right] \sin\theta.$$

Replacing $\cos\theta e^{-\tau/T_1}$ by A, and $M_0(1 - e^{\tau/T_1})$ by B, we continue in the same way finding the signal from the nth pulse:

$$S_n = \left[M_0 A^{n-1} + B(\frac{1 - A^{n-1}}{1 - A})\right] \sin\theta.$$

The total signal-to-noise ratio from a series of N pulses in time $N\tau$ becomes:

$$\begin{aligned} SNR &\propto \frac{\sum_{n=1}^{N} S_n}{\sqrt{N}} \\ &\propto \left[M_0(1 - A^N) + BN - B(\frac{1 - A^N}{1 - A})\right] \frac{\sin\theta}{(1 - A)\sqrt{N}}. \end{aligned}$$

A.3 Geometric Decomposition of Diffusion Tensors

Diffusion can be divided into three basic cases depending on the rank, i.e. the number of non-zero eigenvalues, of the representation tensor [106]:

1) Linear case ($\lambda_1 \gg \lambda_2 \simeq \lambda_3$): diffusion is mainly in the direction corresponding to the largest eigenvalue,

$$\mathbf{D} \simeq \lambda_1 \mathbf{D}_l = \lambda_1 \hat{\mathbf{e}}_1 \hat{\mathbf{e}}_1^T.$$

2) Planar case ($\lambda_1 \simeq \lambda_2 \gg \lambda_3$): diffusion is restricted to a plane spanned by the two eigenvectors corresponding to the two largest eigenvalues,

$$\mathbf{D} \simeq 2\lambda_1 \mathbf{D}_p = \lambda_1 (\hat{\mathbf{e}}_1 \hat{\mathbf{e}}_1^T + \hat{\mathbf{e}}_2 \hat{\mathbf{e}}_2^T).$$

3) Spherical case ($\lambda_1 \simeq \lambda_2 \simeq \lambda_3$): isotropic diffusion,

$$\mathbf{D} \simeq 3\lambda_1 \mathbf{D}_s = \lambda_1 (\hat{\mathbf{e}}_1 \hat{\mathbf{e}}_1^T + \hat{\mathbf{e}}_2 \hat{\mathbf{e}}_2^T + \hat{\mathbf{e}}_3 \hat{\mathbf{e}}_3^T).$$

The coordinates of $\mathbf{D}$ in the trace-normalized tensor basis $\{\mathbf{D}_l, \mathbf{D}_p, \mathbf{D}_s\}$ are measures of how close the diffusion is to the generic cases line, plane and sphere. When only the shape of the diffusion tensor is of interest, the coordinates derived should be normalized. For example, normalization using $\mathrm{Tr}\{\mathbf{D}\}$ gives for the linear, planar and spherical measures:

$$c_l = \frac{\lambda_1 - \lambda_2}{\lambda_1 + \lambda_2 + \lambda_3}, \quad c_p = \frac{2(\lambda_2 - \lambda_3)}{\lambda_1 + \lambda_2 + \lambda_3}, \quad c_s = \frac{3\lambda_3}{\lambda_1 + \lambda_2 + \lambda_3}.$$

$$c_l = \frac{\lambda_1 - \lambda_2}{\lambda_1 + \lambda_2 + \lambda_3}, \quad c_p = \frac{2(\lambda_2 - \lambda_3)}{\lambda_1 + \lambda_2 + \lambda_3}, \quad c_s = \frac{3\lambda_3}{\lambda_1 + \lambda_2 + \lambda_3}.$$

Each of these measures lies in the range from zero to one, and their sum is one. An anisotropy measure describing the deviation from the spherical case is achieved

as follows:

$$C_a = C_l + C_p = 1 - C_s = \frac{\lambda_1 + \lambda_2 - 2\lambda_3}{\lambda_1 + \lambda_2 + \lambda_3} .$$

Bibliography

[1] F. Aboitiz, A. B. Scheibel, R. S. Fisher, and E. Zaidel. Fiber composition of the human corpus callosum. *Brain Research*, 598:143–153, 1992.

[2] A. Abragam. *The Principles of Nuclear Magnetism*. Oxford: The Clarendon Press, 1961.

[3] M. S. Albert, D. Balamore, K. Sakai, D. Kacher, R. L. Walsworth, E. Oteiza, and F. A. Jolesz. Hyperpolarized ^{129}Xe lifetimes in blood. In *Proc., ISMRM 4th Annual Meeting, New York*, page 1357, 1996.

[4] M. S. Albert, G. D. Cates, B. Driehuys, W. Happer, B. Saam, C. S. Springer Jr, and A. Wishnia. Biological magnetic resonance imaging using laser-polarized ^{129}Xe. *Nature*, 370:199–201, 1994.

[5] M. S. Albert, V. D. Schepkin, and T. F. Budinger. Measurement of ^{129}Xe T_1 in blood to explore the feasibility of hyperpolarized ^{129}Xe MRI. *J. Comput. Assist. Tomogr.*, 19(6):975–978, 1995.

[6] M. S. Albert, C. S. Springer, and A. Wishnia. ^{129}Xe relaxation catalysis by oxygen. In *Proc., SMRM 11th Annual Meeting*, page 4710, 1992.

[7] A. M. Andersen and J. Ladefoged. Partition coefficient of ^{133}Xenon between various tissues and blood in vivo. *Scand. J. Clin. Lab. Invest.*, 19:72–78, 1967.

[8] A. W. Anderson, J. Zhong, O. A. C. Petroff, A. Szafer, B. R. Ransom, J. W. Prichard, and J. C. Gore. Effects of osmotically driven cell volume changes on diffusion-weighted imaging of the rat optic nerve. *Magn. Reson. Med.*, 35:162–167, 1996.

[9] P. J. Basser and C. Pierpaoli. Microstructural and physiological features of tissues elucidated by quantitative-diffusion-tensor MRI. *J. Magn. Reson. Ser. B*, 111:209–219, 1996.

[10] C. Beaulieu and P. S. Allen. Determinants of anisotropic water diffusion in nerves. *Magn. Reson. Med.*, 31:394–400, 1994.

[11] C. Beaulieu and P. S. Allen. Some magnetization transfer properties of water in myelinated and nonmyelinated nerves. In *Proc. SMR 2nd annual meeting*, page 169, 1994.

[12] P. Bevington. *Data Reduction and Analysis for the Physical Sciences.* McGraw-Hill, New York, 1969.

[13] A. M. Bidabé, D. Gense de Beaufort, A. M. Gin, and J. M. Caillé. Measurement of cerebral blood flow by the stable xenon computerized tomography method. *J. Neuroradiol.*, 17:103–1241, 1990.

[14] A. Bifone, Y. Q. Song, R. Seydoux, R. E. Taylor, B. M. Goodson, T. Pietrass, T. Budinger, G. Navon, and A. Pines. NMR of laser-polarized xenon in human blood. *Proc. Natl. Acad. Sci.*, 93:12932–6, 1996.

[15] D. Le Bihan. Is water diffusion restricted in human brain white matter? An echo-planar NMR imaging study. *NeuroReport*, 4:887–890, 1993.

[16] F. Bloch. Nuclear induction. *Phys. Rev.*, 70:460–474, 1946.

[17] M. A. Bouchiat, T. R. Carver, and C. M. Varnum. *Phys. Rev. Lett.*, 5:373–377, 1960.

[18] P. T. Callaghan. *Principles of nuclear magnetic resonance microscopy.* Oxford Science, 1991.

[19] P. T. Callaghan. Pulsed-gradient spin-echo NMR for planar, cylindrical, and spherical pores under conditions of wall relaxation. *J. Magn. Reson. ser. A*, 113:53–59, 1995.

[20] G. D. Cates, C. Charles, R. Black, B. Driehuys, W. Happer, A. Johnson, J. Macfall, H. Middleton, C. Ravin, B. Saam, K. Sauer, J. Swartz, M. Wagshul, and A. Wishnia. *Bull. Amer. Physical Soc.*, 41:1104, 1996.

[21] G. D. Cates, R. J. Fitzgerald, A. S. Barton, P. Bogorad, M. Gatzke, N. R. Newbury, and B. Saam. Rb-^{129}Xe spin-exchange rates due to binary and three-body collisions at high Xe pressures. *Phys. Rev. A*, 45:4631–4639, 1992.

[22] D. C. Chang and C. F. Hazlewood. Nuclear magnetic resonance study of squid giant axon. *Bichimica et Biophysica Acta*, 630:131–136, 1980.

[23] R. Y. Z. Chen, F-C. Fan, S. Kim, K-M. Jan, S. Usami, and S. Chien. Tissue-blood partition coefficient for xenon: temperature and hematocrit dependence. *J. Appl. Physiol.*, 49:178–183, 1980.

[24] T. L. Chenevert, J. A Brunberg, and J. G. Pipe. Anisotropic diffusion in human white matter: Demonstration with MR techniques in vivo. *Radiology*, 177:401–405, 1990.

[25] T. E. Chupp, R. J. Hoare, R. L. Walsworth, and B. Wu. Spin-exchange pumped ^{3}He and ^{129}Xe Zeeman masers. *Phys. Rev. Lett.*, 72:2363–2366, 1994.

[26] F. D. Colgrove, L. D. Schearer, and G. K. Walters. Polarization of ^{3}He gas by optical pumping. *Phys. Rev.*, 132:2561–2572, 1963.

[27] D. G. Cory and A. N. Garroway. Measurement of translational displacement probabilities of NMR: an indicator of compartmentation. *Magn. Reson. Med.*, 14:435–444, 1990.

[28] B. V. Derjaguin and L. Landau *Acta. Physicochim. URSS*, 14:633–662, 1941.

[29] P. Diehl and J. Jokisaari. Nuclear magnetic relaxation of the ^{129}Xe and ^{131}Xe isotopes of xenon gas dissolved in isotropic and anisotropic liquids. *J. Magn. Reson.*, 88:660–665, 1990.

[30] M. D. Does and R. E. Snyder. T2 relaxation of peripheral nerve measured in vivo. *Magn. Reson. Imag.*, 13:575–580, 1995.

[31] M. D. Does and R. E. Snyder. Multiexponential T2 relaxation in degenerating peripheral nerve. *Magn. Reson. Med.*, 35:207–213, 1996.

[32] P. Douek, R. Turner, J. Pekar, N. Patronas, and D. Le Bihan. MR color mapping of myelin fiber orientation. *J. Comp. Assist. Tomogr.*, 15(6):923–929, 1991.

[33] G. Eckert, W. Heil, M. Meyerhoff, E. W. Otten, R. Surkau, M. Werner, M. Leduc, P. J. Nacher, and L. D. Schearer. A dense polarized ^{3}He target based on compression of optically pumped gas. *Nucl. Instr. Meth. A*, 320:53–65, 1992.

[34] W. A. Edelstein, G. H. Glover, C. J. Hardy, and R. W. Redington. The intrinsic signal-to-noise ratio in NMR imaging. *Magn. Reson. Med.*, 3:604–618, 1986.

[35] A. E. English, K. P. Whittall, M. L. G. Joy, and R. M. Henkelman. Quantitative two-dimensional time correlation relaxometry. *Magn. Reson. Med.*, 22:425–434, 1991.

[36] K. R. Foster, H. A. Resing, and A. N. Garroway. Bounds on "bound water": transverse nuclear magnetic resonance relaxation in barnacle muscle. *Science*, 194:324–326, 1976.

[37] A. M. Galaburda, M. LeMay, T. L. Kemper, and N. Geschwind. Right-left asymmetries in the brain. *Science*, 199:852–856, 1978.

[38] M. Gatzke, G. D. Cates, B. Driehuys, D. Fox, W. Happer, and B. Saam. Extraordinarily slow nuclear spin relaxation in frozen laser-polarized ^{129}Xe. *Phys. Rev. Lett.*, 70:690–693, 1993.

[39] N. Geschwind and W. Livitsky. Human brain: left-right asymmetries in temporal speech region. *Science*, 161:186–187, 1968.

[40] F. A. Gobas, J. M. Lahittete, G. Garofalo, W. Y. Shiu, and D. Mackay. A novel method for measuring membrane-water partition coefficients of hydrophobic organic chemicals: comparison with 1-octanol-water partitioning. *J. Pharm. Sci.*, 77:265–72, 1988.

[41] J. Gomori, R. Grossman, C. Yu-Ip, and T. Asakura. NMR relaxation times in blood: dependence on field strength, oxidation state, and cell integrity. *J. Comput. Assist. Tomogr.*, 11(4):684–690, 1987.

[42] C.P. Gonatas, J.S. Leigh, and A.G. Yodh. Magnetic resonance images of coarsening inside a foam. *Phys. Rev. Lett.*, 75:573–576, 1995.

[43] H. Gudbjartsson, S. E. Maier, R. V. Mulkern, I. Á. Mórocz, S. Patz, and F. A. Jolesz. Line scan diffusion imaging. *Magn. Reson. Med.*, 36:509–519, 1996.

[44] E. L. Hahn. Spin echoes. *Phys. Rev.*, 80:580, 1950.

[45] W. Happer, E. Miron, S. Schaefer, D. Schreiber, W. A. van Wijngaarden, and X. Zeng. Polarization of the nuclear spins of noble-gas atoms by spin exchange with optically pumped alkali metal atoms. *Phys. Rev. A*, 29:3092–3110, 1984.

[46] R. M. Henkelman, G. J. Stanisz, J. K. Kim, and M. J. Bronskill. Anisotropy of NMR properties of tissues. *Magn. Reson. Med.*, 32:592–601, 1994.

[47] D. I. Hoult and P. C. Lauterbur. The sensitivity of the zeugmatographic experiment involving human samples. *J. Magn. Reson.*, 34:425–433, 1979.

[48] P. S. Hüppi, S. Peled, G. P. Zientara, S. E. Maier, H. Gudbjartsson, and F. A. Jolesz. Microstructural development of the human newborn brain assessed in vivo by diffusion tensor MRI. In *Proc. ISMRM 5th Annual Meeting, Vancouver, Canada.*, page 77, 1997.

[49] E. I. Eger II. A mathematical model of uptake and distribution. In E.M. Papper and R.J. Kitz, editors, *Uptake and Distribution of Anesthetic Agents*, pages 73–87. McGraw-Hill, 1963.

[50] H. Inouye and D. A. Kirschner. Membrane interactions in nerve myelin. I: Determination of surface charge from effects of pH and ionic strength on period. *Biophys. J.*, 53:235–246, 1988.

[51] J. Israelachvili. *Intermolecular and Surface Forces.* Academic Press, 1991.

[52] C. J. Jameson, A. K. Jameson, and J. K. Hwang. Nuclear spin relaxation by intermolecular magnetic dipole coupling in the gas phase. ^{129}Xe in oxygen. *J. Chem. Phys.*, 89:4074–4081, 1988.

[53] J. Jeener, B. H. Meier, P. Bachmann, and R. R. Ernst. Investigation of exchange processes by two-dimensional NMR spectroscopy. *J. Chem. Phys.*, 71(11):4546–4553, 1979.

[54] F. A. Jolesz, J. F. Polak, D. F. Adams, and P. W. Ruenzel. Myelinated and nonmyelinated nerves: Comparison of proton MR properties. *Radiology*, 164:89–91, 1987.

[55] F. A. Jolesz, J. F. Polak, P. W. Ruenzel, and D. F. Adams. Wallerian degeneration demonstrated by magnetic resonance: spectroscopic measurements on peripheral nerve. *Radiology*, 152:85–87, 1984.

[56] J. Kärger, H. Pfeifer, and W. Heink. Principles and application of self-diffusion measurements by nuclear magnetic resonance. *Adv. Magn. Reson.*, 12:1, 1988.

[57] A. Kastler. *J. Phys. Radium*, 11:255, 1950.

[58] S. S. Kety. The theory and applications of the exchange of inert gas at the lungs and tissues. *Pharmacol. Rev.*, 3:1–41, 1951.

[59] R. Knauss, G. Fleischer, W. Gründer, Jörg Kärger, and A. Werner. Pulsed field gradient NMR and nuclear magnetic relaxation studies of water mobility in hydrated collagen II. *Magn. Reson. Med.*, 36:241–248, 1996.

[60] G. Laicher, D. C. Ailion, and A. G. Cutillo. Water self-diffusion measurements in excised rat lungs. *J. Magn. Reson. Ser. B*, 111:243–253, 1996.

[61] L. L. Latour, K. Svoboda, P. P. Mitra, and C. H. Sotak. Time-dependent diffusion of water in a biological model system. *Proc. Natl. Acad. Sci.*, 91:1229–1233, 1994.

[62] C. L. Lawson and R. J. Hanson. *Solving least squares problems.* Prentice-Hall, Englewood Cliffs NJ., 1974.

[63] J-H. Lee, C. Labadie, C. S. Springer Jr, and G. S. Harbison. Two-dimensional inverse laplace transform NMR: altered relaxation times allow detecti · of exchange correlation. *J. Am. Chem. Soc.*, 115:7761–7764, 1993.

[64] M. LeMay. Left-right dissymmetry, handedness. *AJNR*, 13:493–504, 1992.

[65] A. L. MacKay, K. P. Whittall, J. Adler, D. K. P. Li, D. W. Paty, and D. A. Graeb. *In-vivo* visualization of myelin water in brain by magnetic resonance. *Magn. Reson. Med.*, 31:673–677, 1994.

[66] W. W. Mapleson. Quantitative prediction of anesthetic concentrations. In E.M. Papper and R.J. Kitz, editors, *Uptake and Distribution of Anesthetic Agents*, pages 104–119. McGraw-Hill, 1963.

[67] J. McConnell. *The theory of nuclear magnetic relaxation in liquids.* Cambridge University Press, 1987.

[68] R. S. Menon and P. S. Allen. Application of continuous relaxation time distributions to the fitting of data from model systems and excised tissue. *Magn. Reson. Med.*, 20:214–227, 1991.

[69] R. S. Menon, M. S. Rusinko, and P. S. Allen. Proton relaxation studies of water compartmentalization in a model neurological system. *Magn. Reson. Med.*, 28:264–274, 1992.

[70] M-E Meyer, O. Yu, B. Eclancher, D. Grucker, and J. Chambron. NMR relaxation rates and blood oxygenation level. *Magn. Reson. Med.*, 34:234–241, 1995.

[71] K. W. Miller, N. V. Reo, A. J. M. Schoot Uiterkamp, D. P. Stengle, T. R. Stengle, and K. L. Williamson. Xenon NMR: Chemical shifts of a general anesthetic in common solvents, proteins and membranes. *Proc. Natl. Acad. Sci. USA*, 78:4946–4949, 1981.

[72] C. T. W. Moonen, J. Pekar, M. H. M de Vleeschouwer, P. van Gelderen, P. C. M. van Zijl, and D. DesPres. Restricted and anisotropic displacement of water in healthy cat brain and in stroke studied by NMR diffusion imaging. *Magn. Reson. Med.*, 19:327–332, 1991.

[73] M. A. Moscarello, L. S. Chia, D. Leighton, and D. Absalom. Size and surface charge properties of myelin vesicles from normal and diseased (multiple sclerosis) brain. *J. Neurochem.*, 45(2):415–21, 1985.

[74] M. E. Moseley, Y. Cohen, J. Kucharczyk, J. Mintorovitch, H. S. Asgari, M. F. Wendland, J. Tsuruda, and D. Norman. Diffusion-weighted MR imaging of anisotropic water diffusion in cat central nervous system. *Radiology*, 176:439–445, 1990.

[75] R. V. Mulkern, A. R. Bleier, I. K. Adzamli, R. G. S. Spencer, T. Sandor, and F. A. Jolesz. Two-site exchange revisited: A new method for extracting exchange parameters in biological systems. *Biophys. J.*, 55:221–232, 1989.

[76] T. Nakada and H. Matsuzawa. Three-dimensional anisotropy contrast magnetic resonance imaging of the rat nervous system: MR axonography. *Neuroscience Research*, 22:389–398, 1995.

[77] W. T. Norton and S. E. Poduslo. Myelination in rat brain: method of myelin isolation. *J. Neurochem.*, 21:749–757, 1973.

[78] R. C. Oldfield. The assessment and analysis of handedness: the Edinburgh inventory. *Neuropsychologia*, 9:97–113, 1971.

[79] L. Pauling and C. D. Coryell. The magnetic properties and structure of hemoglobin, oxyhemoglobin and carbonmonoxyhemoglobin. *Proc. Natl. Acad. Sci. U.S.A.*, 22:210–216, 1936.

[80] S. Peled, H. Gudbjartsson, C-F. Westin, R. Kikinis, and F. A. Jolesz. Magnetic resonance imaging shows orientation and asymmetry of white matter fiber tracts. *Brain Research*, 1997. in press.

[81] S. Peled, F. A. Jolesz, C-H. Tseng, L. Nascimben, M. S. Albert, and R. L. Walsworth. Determinants of tissue delivery for ^{129}Xe magnetic resonance in humans. *Magn. Reson. Med.*, 36:340–344, 1996.

[82] S. Peled, C-H. Tseng, L. Nascimben, R. L. Walsworth, and F. A. Jolesz. Hyperpolarized ^{129}Xe in blood *in vitro*. In *Proc. Experimental NMR Conference 37th Annual Meeting, Pacific Grove, CA.*, page 375, 1996.

[83] M. Pfeffer and O. Lutz. ^{129}Xe gas NMR spectroscopy and imaging with a whole-body imager. *J. Magn. Reson.*, 108:106–109, 1994.

[84] C. Pierpaoli, P. Jezzard, P. J. Basser, A. Barnett, and G. Di Chiro. Diffusion tensor MR imaging of the human brain. *Radiology*, 201:637, 1996.

[85] G. L. Pollack, J. F. Himm, and J. J. Enyeart. Solubility of xenon in liquid *n*-alkanols: Thermodynamic functions in simple polar liquids. *J. Chem. Phys.*, 81:3239, 1984.

[86] R. P. Rand, N. L. Fuller, and L. J. Lis. Myelin swelling and measurement of forces between myelin membranes. *Nature*, 279:258–260, 1979.

[87] T. G. Reese, R. M. Weisskoff, R. N. Smith, B. R. Rosen, R. E. Dinsmore, and V. J. Wedeen. Imaging myocardial fiber architecture in vivo with magnetic resonance. *Magn. Reson. Med.*, 34(6):786–91, 1995.

[88] M. Rosen, K.P. Coulter, T.E. Chupp, S.D. Swanson, and B.W. Agranoff. *Bull. Amer. Physical Soc.*, 41:1085, 1996.

[89] K. Sakai, A. M. Bilek, E. Oteiza, R. L. Walsworth, D. Balamore, F. A. Jolesz, and M. S. Albert. Temporal dynamics of hyperpolarized ^{129}Xe resonances in living rats. *J. Magn. Reson. B*, 111:300–304, 1996.

[90] J. S. Schoeniger, N. Aiken, E. Hsu, and S. J. Blackband. Relaxation-time and diffusion NMR microscopy of single neurons. *J. Magn. Reson. B*, 103:261–273, 1994.

[91] B. P. Shoenborn. Binding of xenon to horse haemoglobin. *Nature*, 208:760, 1965.

[92] G. J. Stanisz, A. Szafer, G. A. Wright, and R. M. Henkelman. An analytical model of restricted diffusion in bovine optic nerve. *Magn. Reson. Med.*, 37:103–111, 1997.

[93] E. O. Stejskal and J. E. Tanner. Spin diffusion measurements: spin echoes in the presence of a time-dependent field gradient. *J. Chem. Phys.*, 42:288–292, 1961.

[94] M. Sundaram, M. H. McGuire, and F. Schajowicz. Soft-tissue masses: histological basis for decreased signal (short T_2) on T_2-weighted MR images. *AJR Am. J. Roentgenol.*, 148(6):1247–50, 1987.

[95] S. D. Swanson, M. S. Rosen, K. P. Coulter, R. C. Welsh, and T. E. Chupp. *In vivo* NMR imaging of optically polarized ^{129}Xe. In *Proc. ISMRM 4th Annual Meeting, New York*, page 1360, 1996.

[96] A. Szafer, J. Zhong, and J. C. Gore. Theoretical model for water diffusion in tissues. *Magn. Reson. Med.*, 33:697–712, 1995.

[97] R. Tilton and I. Kuntz Jr. Nuclear magnetic resonance studies of xenon-129 with myoglobin and hemoglobin. *Biochemistry*, 21:6850–6857, 1982.

[98] C-H. Tseng, S. Peled, L. Nascimben, E. Oteiza, R. L. Walsworth, and F. A. Jolesz. T_1 of laser polarized ^{129}Xe in blood foam. *J. Magn. Reson.*, 1997. in press.

[99] R. Turner, D. Le Bihan, J. Maier, R. Vavrek, L. K. Hedges, and J. Pekar. Echo planar imaging of intravoxel incoherent motions. *Radiology*, 177:407–414, 1990.

[100] D. van Dusschoten, C. T. W. Moonen, P. A. de Jager, and H. van As. Unraveling diffusion constants in biological tissue by combining Carr-Purcell-Meiboom-Gill imaging and pulsed field gradient NMR. *Magn. Reson. Med.*, 36:907–913, 1996.

[101] V. Vasilescu, E. Katona, V. Simplăceanu, and D. Demco. Water compartments in the myelinated nerve. III. pulsed NMR results. *Experientia*, 34:1443–1444, 1977.

[102] V. Vasilescu, D. G. Mărgineanu, and E. Katona. Heavy water intake in tissues. II. H_2O-D_2O exchange in the myelinated nerve of the frog. *Experentia*, 33:192–194, 1977.

[103] E. J. W. Verwey and J. Th. G. Overbeek. *Theory of the stability of lyophobic colloids.* Elsevier, 1948.

[104] M.E. Wagshul, T.M. Button, H.F. Li, Z. Liang, C.S. Springer, K. Zhong, and A. Wishnia. *In vivo* MR imaging and spectroscopy using hyperpolarized ^{129}Xe. *Magn. Reson. Med.*, 36:183–191, 1996.

[105] J. B. West. *Respiratory Physiology - The Essentials.* Williams & Wilkins, 5 edition, 1995.

[106] C-F. Westin, S. Peled, H. Gudbjartsson, R. Kikinis, and F. A. Jolesz. Geometrical diffusion measures for MRI from tensor basis analysis. In *Proc. ISMRM 5th Annual Meeting, Vancouver, Canada*, page 1742, 1997.

[107] K. P. Whittall. Quantitative interpretation of NMR relaxation data. *J. Magn. Reson.*, 84:134–152, 1989.

[108] K. P. Whittall, A. L. MacKay, D. A. Graeb, R. A. Nugent, D. K. B. Li, and D. W. Paty. *In vivo* measurement of T_2 distributions and water contents in normal human brain. *Magn. Reson. Med.*, 37:34–43, 1997.

[109] R. S. Wijesinghe, F. L. H. Gielen, and J. P. Wikswo Jr. A model for compound action potentials and currents in a nerve bundle I: The forward calculation. *Ann. Biomed. Eng.*, 19:43–72, 1991.

[110] D. M. Wimberger, T. P. Roberts, A. J. Barkovich, L. M. Prayer, M. E. Moseley, and J. Kucharczyk. Identification of "premyelination" by diffusion-weighted MRI. *J. Comp. Assist. Tomogr.*, 19(1):28–33, 1995.

[111] S. F. Witelson and R. S. Nowakowski. Left out axons make men right: A hypothesis for the origin of handedness and functional asymmetry. *Neuropschologia*, 29(4):327–333, 1991.

[112] P. I. Yakovlev and P. Rakic. Patterns of decussation of bulbar pyramids and distribution of pyramidal tracts on two sides of the spinal cord. *Trans. Am. Neurol. Assoc.*, 91:366–367, 1966.

[113] J. R. Zimmerman and W. E. Brittin. Nuclear magnetic resonance studies in multiple phase systems: Lifetime of a water molecule in an adsorbing phase on silica gel. *J. Phys. Chem.*, 61:1328–1333, 1957.